Next generation dark-field microscopy: from high-speed single particle tracking to label-free imaging



Xuanhui Meng

Linacre College

University of Oxford

A thesis submitted for the degree of

Doctor of Philosophy in Theoretical and Physical Chemistry

18th October, 2019

Acknowledgements

Here I would like to take this great opportunity to express my most sincere gratitude to those wonderful people who have provided endless help and encouragements both academically and socially over my four years of DPhil life in Oxford. Without their supports, I would not be able to bridge the gap between my previous education background and postgraduate research quickly and make today's achievements.

First of all, I would like to thank Professor Philipp Kukura, my supervisor, for his patient guidance, enthusiastic encouragement and inspiring ideas of this research work. Indeed, it is my honour to be supervised by him. Especially for me, a person who has little background knowledge in physics and optics, his kindness and patience of training me how to build an optical microscope step-by-step when I just joined in the lab leave me an deep impression. I am sure there will always be professors as easy-going as him in any universities, however, he is the only person that I have ever met. Being a person comes from a country with a totally different cultural background, the free and relaxed environment both at and after work which he built up makes me feel as comfortable as being at home. In addition to life in the lab, his kind personality and interpersonal skills always have the value worthy of reference for me to benefit in the rest of my life. Most importantly, I will never forget the amazing meat feast that he has ever made for the whole group.

Next, I would especially like to thank Dr. Nikolas Hundt, an outstanding person who has a very solid biological background. He plays the role of a mentor

and a ‘sweet’ friend, whenever I encountered any problems in my projects on the biology front, having a fruitful discussion with him could always break up the stumbling blocks in the most effective way. As a proverb saying in Chinese, when I walk along with two others, they may serve me as my teachers. Without any doubt, I did learn a lot from him, who perfectly fits all positive stereotypes of a German people, i.e., preciseness, concentration and prudence. I have been firmly convinced from his achievements that all efforts will be paid off as he always strictly follows all standard protocols, requirements and rules.

Also, I want to offer my appreciation to Dr. Adar Sonn-Segev who took care of me well like a senior sister. It is great fun to work with her and a valuable chance to learn knowledge of data processing and simulation from her. Apart from my projects, I also thoroughly enjoyed working together with our collaborator, Dr. Yasuharu Takagi. Not only his fun researches broadened my horizons of science, but also his abundant life experience serves as a lighthouse which guides my way to future accomplishments.

The gang named Gandam by their names of Gavin Young, Dan Cole and Adam Fineberg deserved a special acknowledgement. I am particularly grateful for the assistance on microscope building given by all these talented people. Beyond the academics, their deep love in spicy Chinese food builds a strong connection between us. Hanging out with them made my memorable time in Oxford and also significantly improved my language skills. I will never forget those slangs I have been taught. I also want to thank Lee Priest, Manish Kushwah and Yiwen Li who joined in the group later but perfectly maintained the productivity and lovely atmosphere of our group. Although we are not working in the same lab, I would like to appreciate all my collaborators, Dr. Sanli Faez and Dr. Florian Selbach for their inspiring ideas, helpful discussions and samples with high quality.

Last but not least, I would like to express my greatest appreciation to my parents, whose everlasting understanding and warm caring to support me studying thousands of miles away from home. Their love offers me the most powerful tool to solve any problems both in academics and life. My special thanks are extended to Xixi Yu, for bringing me a colourful life alongside everyday lab works. Particularly, this thesis would have not been completed without her selfless support, cheerful chat and endless encouragement.

Statement of Originality

The research described in this thesis was carried out by the author between October 2015 and September 2019 and includes nothing which is the outcome of work done in collaboration, except where specifically indicated in the text. The use of the first person plural is strictly a matter of style in keeping with standard scientific convention.

List of Publications

The work carried out by the author between October 2015 and September 2019 led to the following publications:

1. K. Namink, **X. Meng**, M. Koper, P. Kukura, S. Faez, Electric-Double-Layer-Modulation-Microscopy, *Physical Review Applied*, 2020, **13**, 044065.

2. **X. Meng**, S. Faez, P. Kukura, Sensing force and charge at the nanoscale with a single molecule tether, in preparation.

3. **X. Meng**, C. Wong, F. Selbach, J. Doye, P. Tinnefeld, P. Kukura, Directly probing double-stranded DNA flexility at sub-persistence length scales, in preparation.

4. A. Sonn-Segev, **X. Meng**, A. Schumacher, P. Kukura, Total internal reflection scattering microscopy for fast accurate tracking of nanoparticles, in preparation.

Abstract

This thesis details the improvement and implementation of a total internal reflection dark-field scattering microscope, in terms of pushing the boundaries of its sensitivity and spatiotemporal resolution, to study the bending flexibility of DNA on biologically important length scales. Furthermore, by observing the scattering intensity response to the reconfiguration of the electric double layer on a substrate, dark-field microscopy has been brought into the field of label-free imaging, establishing a novel contrast mechanism. Specifically, Chapter 2 describes the basics of light scattering and tethered particle motion and elaborates various designs to apply total internal reflection-based dark-field microscopy. After characterisation and quantitative comparison regarding their signal-to-noise ratio and background noise suppression performance, high-speed tracking of 20 nm diameter gold nanoparticles with few nanometre localisation precision and few microsecond exposure time is demonstrated with the optimised set-up. Chapter 3 combines this imaging capability with tethered particle motion to directly address the mechanical properties of double-stranded DNA shorter than 160 base pairs without significant volume exclusion effect. Chapter 4 takes the advantage of the short DNA tether functionalised with a charged gold nanoparticle which behaves like a nanospring in the presence of an alternating electric field, to measure the electrophoretic force and charge with femtonewton sensitivity. In the last chapter, total internal reflection-based dark-field microscopy is applied to optically image the electric double layer around nanostructures on an ITO substrate based on the potentiodynamic

optical contrast mechanism and thus proves its potential, at least in principle, for label-free imaging at the single molecule level.

Contents

List of Figures **v**

List of Tables **viii**

List of Abbreviations **xi**

1 Introduction **1**

2 Materials and methods **21**

2.1 Single molecule tracking 21

2.2 Total internal reflection dark-field scattering microscopy . . . 24

2.2.1 Implementations of total internal reflection and background rejection 39

2.2.2 Characterisation of the final set-up 47

2.3 Tethered particle motion assay 51

2.3.1 Surface passivation and flow chamber assembly 52

2.3.2 Tether assembly 55

2.3.3 Density control 56

2.3.4 Spot detection and tracking 57

3 Flexibility of dsDNA at sub-persistence length scales **59**

3.1 Introduction 59

3.2 Experimental method 67

3.2.1 Materials 67

3.2.2 Double stranded DNA and TPM sample preparation . 68

3.2.3 RAD52 preparation 71

3.2.4 Stroboscopic dark-field microscope 71

3.2.5 Instrument setup parameters 72

3.2.6 Data acquisition and analysis 73

3.3 Experimental results 78
3.3.1 Observed Brownian motion: high degree of symmetry . 78
3.3.2 RDF: Particle-to-particle variability 79
3.3.3 Dependence of tethered particle distribution on DNA contour length 81
3.3.4 Monte Carlo simulations 82
3.3.5 Small conformational changes by DNA-protein interactions 89
3.4 Discussion 90
3.4.1 Volume exclusion effect 90
3.4.2 Heating effect of gold nanoparticles 92
3.5 Conclusion and outlook 93

4 Sensing force and charge at the nanoscale with a single molecule tether 97
4.1 Introduction 97
4.2 Experimental methods 99
4.2.1 TPM sample preparation and oscillating electric field implementation 99
4.2.2 Dark-field microscopy 100
4.2.3 Characterisation of individual effective spring constants 101
4.2.4 Measuring the displacement when applying external electric field 104
4.2.5 Extracting charge variations from the measured displacement 106
4.3 Results and discussion 108
4.3.1 Identification of molecular sensors and source of errors 108
4.3.2 Force measurement with external electric field 109
4.3.3 Displacement dependence on applied electric field potential 111
4.3.4 Changes in charge due to intermolecular binding events 112
4.3.5 Zeta-potential variations due to pH value 112
4.3.6 Ruling out the effect of electro-osmotic flow 114
4.4 Conclusion and outlook 115

5 Nanoscale imaging of the electric double layer 117
5.1 Introduction 117
5.2 Experimental methods 120
5.2.1 Dark-field scattering microscopy 120

5.2.2 ITO substrate preparation 120
5.2.3 Potentiodynamic optical contrast of the EDL 120
5.3 Results and discussion 123
5.3.1 Surface topographic variations 123
5.3.2 Potentiodynamic optical contrast response to applied cell potential 123
5.3.3 Accumulated charge at the substrate 125
5.3.4 Ruling out the quasi-capacitance charging effect 125
5.3.5 Material-specificity of the EDL 127
5.4 Conclusion and outlook 128

6 Conclusion and outlook **131**
6.1 Conclusion 131
6.2 Outlook 134

References **137**

List of Figures

1.1 Chemical structure of DNA. 3

1.2 DNA replication. 5

1.3 Atomic force microscope using beam deflection detection. . . . 13

2.1 Evanescent field and penetration depth. 28

2.2 Diagram of bright-field microscopy versus dark-field microscopy. 29

2.3 Focus control channel. 35

2.4 Prism geometry based TIRSM set-up. 36

2.5 Motion blur effects on imaging. 38

2.6 Effect of exposure time σ on the measured probability density distributions. 39

2.7 Objective-type TIRSM set-up using perforated mirror. 41

2.8 Objective-type TIRSM set-up using two micro-mirrors. 42

2.9 Quantitative comparison of Prism-type vs. Objective-type TIRSM set-up. 44

2.10 Emission properties of a vertically oriented dipole close to a dielectric planar antenna. 46

2.11 Comparison of Perforated mirror vs. micro-mirror TIRSM set-up. 47

2.12 Localisation precision and particle size distribution. 50

2.13 Vibration analysis. 51

2.14 Binding density exploration. 53

2.15 Surface passivation quality test. 54

3.1 Freely-joint chain model and worm-like chain model. 60
3.2 A monomer of RAD52. 67
3.3 Double-stranded DNA tether assembly. 70
3.4 Concept of pulsed laser illumination. 72
3.5 High signal-to-noise ratio dark-field image of 20 nm AuNPs. . 73
3.6 Various tethered particle behaviours. 77
3.7 Observed Brownian motion of single molecule tethered particles. 78
3.8 Radial distribution function. 80
3.9 Extracted persistence length of short dsDNA lengths. 82
3.10 Coarse-grained molecular dynamics simulations. 86
3.11 Results of statistical t-test for determining the measured persistence length. 88
3.12 Small conformational change by DNA-protein interactions. . . 90
3.13 Theoretical calculation of temperature increase on surface. . . 93

4.1 Dark-field microscope and concept of applying an alternating electric field. 100
4.2 Particle diffusive motion. 102
4.3 Measuring the effective spring constant by thermal fluctuations. 103
4.4 Characterisation of localisation error. 105
4.5 Response of a molecular sensor to the applied alternating electric field. 107
4.6 Particle displacements for different tethers. 110
4.7 Displacement dependence on applied electric field potential. . 111
4.8 Dependence of particle displacements on nanoparticle charge for a fixed potential. 113

4.9 Ruling out the effect of electro-osmotic flow. 114

5.1 Measuring the potentiodynamic contrast of the EDL on a rough surface. 122

5.2 The optical signal from the electric double layer under variable surface potential. 124

5.3 PDOC response on the ITO grain for three different anions in the electrolyte solution. 126

5.4 The elastic light scattering signal from chromium deposited on the ITO-coated slides through a SiN membrane 127

List of Tables

1.1 Comparison geometries among A-form, B-form and Z-form DNA. 8

3.1 Excursion number for various DNA lengths. 92

List of Abbreviations

l_p	Persistence length
AFM	Atomic force microscopy
AuNP	Gold nanoparticle
BFP	Back focal plane
bp	Base pairs
BSA	Bovine serum albumin
CMOS	Complementary metal–oxide–semiconductor
COM	Centre of mass
CW	Continuous wave
DNA	Deoxyribonucleic acid
dsDNA	Double stranded DNA
EDL	Electric double layer
EF	Electric field
ELS	Elastic light scattering
EO	Electric-osmotic
FFT	Fast Fourier transform
FJC	Freely-jointed chain
FOV	Field of view
FRET	Förster resonance energy transfer
FWHM	Full-with at half-maximum
hs-AFM	High-speed atomic force microscopy

iSCAT	Interferometric scattering microscopy
ITO	Indium tin oxide
mPEG	Monomethoxy poly-ethylene glycol silane
NA	Numerical aperture
ND	Neutral density
nt	Nucleotides
PCR	Polymerase chain reaction
PDOC	Potentiodynamic optical contrast
PEG	Poly-ethylene glycol
pl	Isoelectric point
PSF	Point spread function
RAM	Random-access memory
RMS	Root mean square
RNA	Ribonucleicacid acid
ROI	Region of interest
smFRET	Single-molecule fluorescence resonance energy transfer
SNR	Signal-to-noise ratio
SPT	Single particle tracking
ssDNA	Single stranded DNA
TIR	Total internal reflection
TIRFM	Total internal reflection fluorescence microscopy
TIRSM	Total internal reflection scattering microscopy
TPM	Tethered particle motion
Vpp	Voltage peak-to-peak
WB	Working buffer
WFL	Wide field lens
WLC	Worm-like chain

Chapter 1

Introduction

Deoxyribonucleic acid (DNA) is a biological molecule that has been found in all known forms of life including both eukaryotes and prokaryotes, as well as many viruses.[1–4] It carries all genetic information serving as instructions for organisms to develop, function, grow and reproduce. In eukaryotic cells, a long ($\sim$2 m) DNA is organised into compact structures called chromosomes and resides mostly inside the cell nucleus.[1,5,6] Nearly every cell in our body has the same DNA. In contrast, within bacteria and other simple or prokaryotic cell organisms, DNA is distributed only in the cytoplasm.[3] For viruses, DNA is packaged in a protein shell called a viral capsid.[4]

DNA is essential to every living organism since it contains the genetic information organisms need to both develop and reproduce, but it has a relatively simple structure as compared to other biological macromolecules. DNA is a long biological polymer assembled as a chain with repeating nucleotides that are joined together. Each nucleotide consists of a nitrogenous base linked to a sugar termed deoxyribose, and a phosphate group.[1,7] There are four types of nitrogen-containing nucleobases, which are classified into purines comprising adenine (A) and guanine (G), and pyrimidines consisting of cytosine (C) and thymine (T). C and T bases have only one ring, while A and G bases have two rings. (Figure 1.1b and c) The sugar of one nucleotide is covalently bound to

the phosphate of another nucleotide to form an alternating sugar-phosphate backbone (Figure 1.1a), which holds multiple linked nucleotides together in the shape of a single DNA chain that is also referred to as polynucleotide. Interestingly, instead of existing as a single chain, DNA usually exists as two coiled helical chains bound tightly to each other by hydrogen bonds.[7,8] American biologist James Watson and English physicist Francis Crick first elucidated its molecular structure of the double-stranded, anti-parallel, right-handed helix based on X-ray diffraction data[8] in the early 1950s. This ground-breaking discovery often misleads people to believe that Watson and Crick are the scientists who first discovered DNA. In reality, it is a complex question to answer who discovered DNA as many researchers and scientists have contributed to reveal the mysteries of DNA and bring us relatively comprehensive understanding of this molecule within around 150 years.

Dated back to 1869, Swiss physiological chemist Friedrich Miescher first identified a new substance what he called nuclein by isolating a molecule in the nuclei of human white blood cells.[9] Later in 1881, the Nobel Prize winner and German biochemist Albrecht Kossel identified nuclein as a nucleic acid and eventually named it as deoxyribonucleic acid. During the period 1885 to 1901, he was also able to isolate those nitrogen bases including A, T, G and C that are now considered to be the basic building blocks of DNA and uracil (U) in ribonucleic acid (RNA).[10]

Few years after Kossel's findings, Russian biochemist Phoebus Levene identified that nucleic acids were composed of a series of components linked together and named the basic units as nucleotide. Together with Walter Jacobs, Levene recognised d-ribose as an essential component of nucleic acids.[11,12] He further went on his research and was credited for first person who discovered ribose as the carbohydrate component of RNA and deoxyribose of DNA. In his

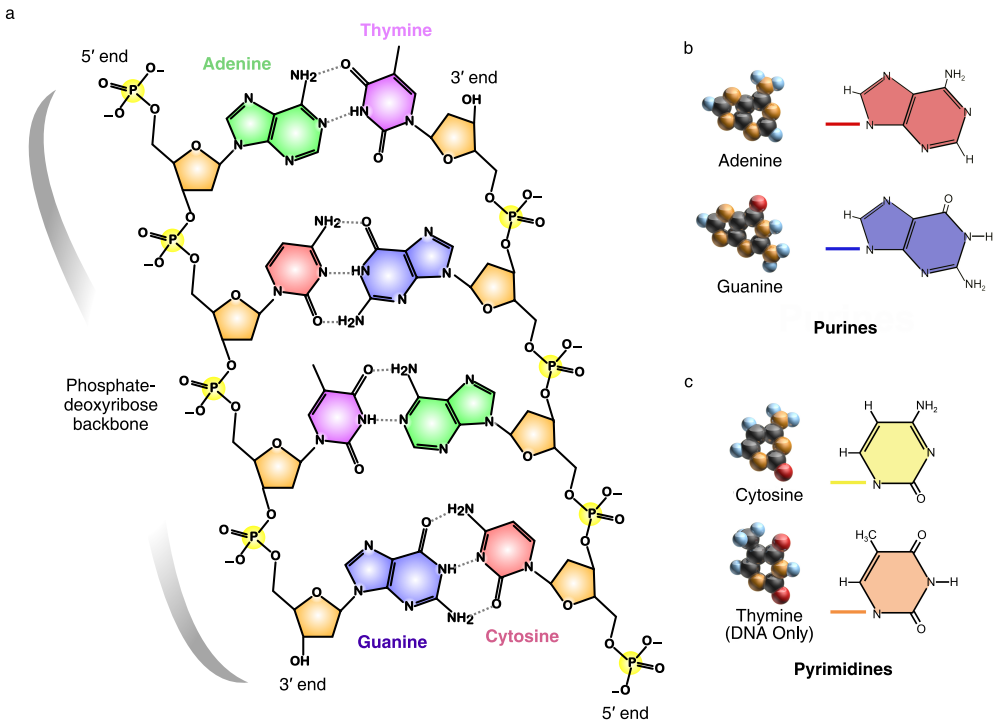


Figure 1.1: Chemical structure of DNA. (a) Chemical structure of DNA, with colored label identifying the four bases as well as the phosphate and deoxyribose components of the backbone. (b) The main purine-derived nucleobases. (c) The pyrimidine nitrogen bases found in DNA and RNA. Panel (a) modified from "DNA chemical structure" by Madprime (CC0/public domain). Panel (b) and (c) modified from "Blausen 0323 DNA Purines" and "Blausen 0324 DNA Pyrimidines" by Blausen.com staff (CC BY 3.0)

proposal, each nucleotide was in turn composed of a phosphate group, either a ribose (in the case of RNA) or a deoxyribose (in the case of DNA) sugar and just one of four nitrogen-containing bases. A series of nucleotides then link together in a string fashion through the phosphate groups which are termed backbone of the molecule and form the DNA molecule. Around 1910, he proposed the tetranucleotide structure of DNA[13] which suggests that nucleotides were always linked and repeated in a fixed order with equal amounts of adenine, guanine, cytosine, and thymine. Though his ideas about the structure of DNA were incorrect, his investigations laid the groundwork for the later work of uncovering the structure of DNA.

One other key piece of history related to the discovery of DNA was credited

to Austrian biochemist Erwin Chargaff.[14–18] His breakthrough was inspired by the famous 1944 paper by Oswald Avery et al.[19] who outlined the nature of DNA as the transforming principle, which essentially means that it's not proteins or carbohydrates but rather DNA was responsible for the transformation of cell properties. After reading Avery's paper, Chargaff analysed the DNA of different species and made two key observations with respect to the chemistry of nucleic acids. First, he discovered that the composition of DNA varies among species but not between individuals of the same species. Second, he concluded that the number of adenine (A) units is usually equal to the number of thymine (T) units, and the amount of guanine (G) units usually approximates the amount of cytosine (C) units. In other words, the total amount of purines (A + G) and the total amount of pyrimidines (C + T) are usually nearly equal. These findings are now known as Chargaff's rules which turned out to be vital to Watson and Crick's model of the DNA double helix.

In May 1952, a remarkably clear and striking X-ray diffraction image of DNA gave Watson and Crick crucial clues to the correct structure of DNA.[20] This important image taken by Roslind Franklin and her graduate student Raymond Gosling clearly showed the double helix structure of DNA and suggested that the backbones had to be on the outside and inspired Watson and Crick. It was in 1953, almost a century after DNA was first isolated, they published their elucidations of DNA's helical, two-stranded structure[8] which is now accepted as the first correct model of DNA.

Hydrogen bonds between two complementary nitrogenous bases of the two separate polynucleotide strands not only make a double-stranded DNA but also stabilise the DNA double helix.[21] According to base pairing rules, A bases always pair with T bases and similarly C bases always pair with G bases, which is consistent with and accounts for Chargaff's rule. These

A-T and G-C associations are known as complementary base pairs. The biological information stored in the DNA sequence, particularly the sequence of repeating nucleobases, plays a vital role in the development, function, growth and reproduction of all species. Both strands of the double-stranded DNA encode the same genetic information which is replicated as and when the two strands separate (Figure 1.2).[22] An intermediate chain of nucleotides known as RNA, which is essential for various biological function such as coding, decoding, regulation and expression of genes, is created using separated DNA strands as a template in a process called transcription.[23] These RNA strands carrying coding sequence of amino acids are further involved in protein synthesis during a process called translation. In 1965, Marshall Nirenberg with the help of scientists in NIH first sequenced the bases in each codon to decipher the genetic code and interpret how it operates in protein synthesis.[24–26] After a decade, British biochemist Frederick Sanger et al. developed a rapid DNA sequencing techniques called dideoxy chain-termination method[27,28] which speeds up the process. The dideoxy method was eventually used in sequencing reactions today and to sequence the entire human genome.

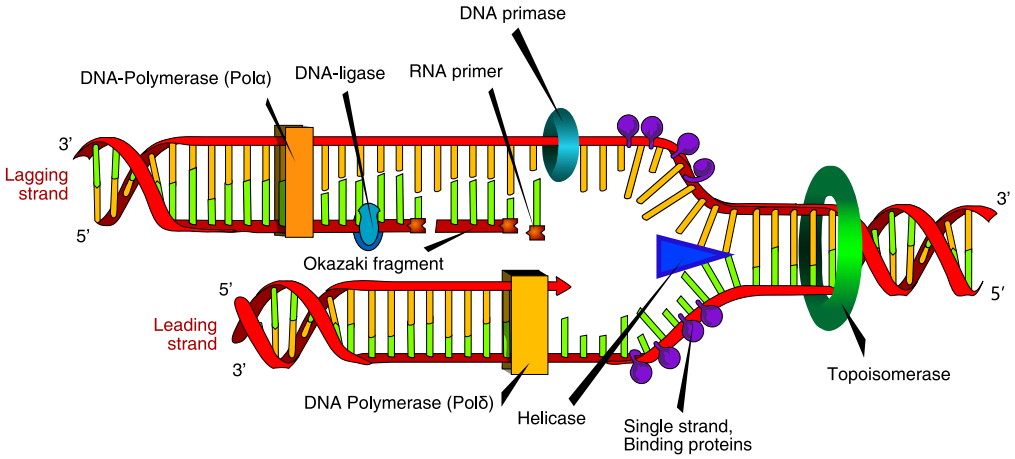


Figure 1.2: DNA replication. Two strands of DNA helix come apart so that enzymes involved in DNA replication have access to DNA molecule. Figure modified from "DNA replication" by LadyofHats Mariana Ruiz (public domain)

The specific base paring feature of DNA also allowed scientists to structurally engineer DNA to create two- and three-dimensional structures such like crystal lattices, nanotubes, polyhedral as desired at the nanoscale regime. In these applications, DNA is utilised as building material for nanotechnology rather than as the carriers of genetic information in organisms. The field of DNA nanotechnology was reportedly first founded by Nadrian Seeman[29] in the early 1980s to create a three-dimensional DNA lattice to simplify their crystallographic study. A rapid growth and expansion of this field occurred in the mid-2000s, for example, an assembly method known as DNA origami developed by Paul Rothemund[30] making it a useful material in biological engineering. In the past decade, a number of applications have been explored based on DNA origami, Nickels and Tinnefeld et al.[31] for example, developed a self-assembled DNA origami force clamp to measure the force of bending of DNA induced by the TATA-binding protein at low piconewton scale.

Despite there being many important and contributing discoveries before and after their work, Watson and Crick's model is fundamental to our current understanding of DNA. Beyond the genetic information content of a given DNA molecule, it has a number of structural properties that are important to its function and are crucial to our understanding of DNA in many biological contexts. Scientists continue to put great effort in understanding the human genome and the importance of DNA to life and health. There are new discoveries have been made regarding the precise geometries and dimensions of the double helix can vary and as a consequence the difference in functions. As an example, DNA supercoiling allows those extremely long DNA strands to coil into tight loops to fit and pack into a significantly smaller volumes relative to its relaxed state.[32–34] The formation of sharp bends in DNA is crucial to many biological processes such as gene regulation[35,36] and binding of transcription factors.[37,38]

Thus, as a physical chemist, it is highly interesting to study the precise nature of the flexibility of DNA since this will provide further insights into the energetics of many of these biological processes.

The structure of DNA is often divided into four different levels: primary, secondary, tertiary, and quaternary. As mentioned above, the linear sequence of nucleotides linked together make up the primary structure of DNA, and the secondary structure of DNA is the basepairing interactions between complementary bases which is responsible for determining the shape of DNA such as helices, and various kinds of loops. In general, the structural properties of a segment of DNA are determined by its nucleotide sequence. Thus, DNA molecules with the same nucleotide sequence will theoretically have the same structural properties.[1] Recently, some local structural variations due to intrinsic variability in the DNA structure have been found, that depend on the neighbouring nucleotides at certain positions.[39]

Tertiary structure is a higher order than the secondary structure in three-dimensional space which takes geometrical and steric constraints into account. The confirmations of DNA is dependent on many factors such as hydration conditions, DNA sequence, the amount and direction of supercoiling, chemical modifications of the bases, the type and concentration of cations in solution.[40] Among many possible conformations of DNA's double helix in space, A-DNA, B-DNA and Z-DNA[20,41–43] are the most common forms. In general, the structural forms of DNA differ in four attributes including handedness (a property that describes how their grooves are oriented in space), length of the helix turn, number of base pairs per turn and difference in size between the major and minor grooves. Comparison geometries of three different DNA forms are listed in Table 1.1. The one proposed by Watson and Crick is considered to be B-DNA which is the most common form of DNA in most living cells.[44,45] A-DNA form

is a right-handed double helix similar to the B-DNA, but with a broader spiral and more compressed along its axis. The major groove of A-DNA is deep and narrow, while the minor groove is wide and shallow. In contrast, Z-DNA was first discovered in 1979[42] and is a left-handed conformation compared to A-DNA and B-DNA. Unlike A-DNA and B-DNA forms, the major and minor grooves of Z-DNA show little difference in width. Although Z-DNA is a transient form of DNA, scientists have discovered that certain proteins bind very strongly to it which suggests that Z-DNA plays an important biological role in protection against viral disease.[46–48]

Geometry attributes:	**A-form**	**B-form**	**Z-form**
Handedness	right-handed	right-handed	left-handed
Length of the helix turn	2.86 nm	3.57 nm	4.56 nm
Mean number of bp/turn	11	10	12
Repeating unit	1 bp	1 bp	2 bp
Rotation/bp	32.7°	34.3°	60°/2
Rise/bp along axis	0.26 nm	0.34 nm	0.37 nm

Table 1.1: Comparison geometries among A-form, B-form and Z-form DNA.

With regard to the quaternary structure of DNA, it refers to the binding of DNA to small protein histones to form nucleosomes and their further packaging into higher-order chromatin fibres.[49] Within eukaryotic cells, chromatin consisting of DNA and protein organises long DNA molecules and packs them tightly into more compact complexes called chromosomes and squeezed into a microscopic space of nucleus. To get a sense of high degree of packing, the size of one nucleotide unit is approximately 3.4 Å (0.34 nm)[1] along the strand. Moreover, a DNA polymer can be very large and contain hundreds of million nucleotides with a length of approximately 2 metres for human cells, if straightened.[50] Consider that the human body contains about 50 trillion cells

which turns to 100 trillion meters of DNA per human which means 300 times return travel between Earth and the Sun.

The quaternary structure of DNA is important in functioning and strongly affects the expression of genes. Processes such as transcription and replication require chromatin fibres to open up transiently and two strands of DNA to come apart temporarily so that polymerases have access to the DNA template. In eukaryotes, the basic structural unit of chromatin is a nucleosome, which is composed of a segment of DNA wound around eight histone proteins.[51,52] Histone proteins are the primary components in chromatin, which are a family of small proteins termed H1, H2A, H2B, H3, and H4.[52,53] Because histones are positively charged, they bind very tightly with the negatively charged DNA (due to the phosphate groups in its phosphate-sugar backbone) as a general gene repressor.[54,55] Two each of the histones H2A, H2B, H3, and H4 come together to form a histone octamer, which binds and wraps approximately 1.7 turns of DNA with approximately 146 base pairs. One additional linker histone protein H1 wraps another 20 (up to 80) base pairs of DNA termed as linker DNA, resulting in two full turns around the octamer, and forming a long chain of nucleosomes. Its 'beads on a string' appearance was first observed by Don and Ada Olins in 1974 using an electron microscope.[56]

During the past few decades, studies of the structural properties of DNA molecules were primarily discussed in static and dynamic terms. Structural properties relating to the static DNA structure are termed the conformational properties considering how its static structure is influenced by base pair sequences as a consequence of translational or rotational variation between successive base pairs and variations in the width and depth of both the major and minor grooves which allow for necessary proteins like transcription factors to make contact with bases.[57] The dynamic structure, on the other hand, is known

as the mechanical properties implying the dynamic potential to its deformation. Although the microscopic details are of considerable importance in providing fundamental information regarding the long-range deformability of DNA, this thesis focuses on studying the mechanical properties, in particular the bending flexibility (bendability) of the double stranded DNA (dsDNA), considering the DNA as an elastic chain. As the flexibility of DNA matters significantly in DNA-protein interactions, quantitative knowledge of the flexibility of DNA is required for understanding many cellular processes such as gene replication, recombination, repair and transcription.[58–60]

According to recent studies, the most widely adopted, worm-like chain (WLC)[61,62] model describes the DNA double helix as a semi-flexible polymer, which behaves more or less like a rigid rod at small length scales (few hundred base pairs), whilst on larger length scales it appears flexible. One single parameter, the persistence length (l_p),[63,64] defines the length scale and quantifies the bending rigidity of DNA. Because of charges on the phosphates in the DNA backbone, the persistence length of DNA depends on the surrounding salt concentration.[65–67] For a double-stranded DNA that is several kilo-basepair (kbp) or longer, in a regime where its flexibility has been intensively studied by single molecule manipulation tools, the l_p is ∼50 nm (150 bp) at physiological salt concentration (∼139 mM KCl).[4,68,69] Such an approximation therefore leads to the notion that DNA must be rigid below the persistence length and the energetic cost to form small DNA loops or sharp bends over length scales shorter than l_p is large compared to $k_\mathrm{B} \cdot T$,[70] where k_B is the Boltzmann constant and T the temperature. In other words, the probability of spontaneous sharp bending by thermal fluctuations seems vanishingly small. However, some recent observations[71,72] yield contradictory results on the dsDNA flexibility, on length scales shorter than the persistence length.

Free molecules of DNA in solution are relatively well-behaved, although this affords an excellent experimental system,[73–78] early attempts to assess the flexibility of DNA were mainly performed in the context of polymer physics theories. Nevertheless, some locally nanoscopic conformational fluctuations and dynamics can hardly be captured/resolved at the ensemble level. It is only during the past two decades that measurements of the intrinsic flexibility of dsDNA has been achieved, using a variety of single molecule detection techniques.[69] These methods can be categorised into force-based techniques and optical microscopy approaches according to how the single molecule is detected.

Force-based techniques involve manipulating the single molecule and measuring the displacements due to an applied force. The most frequently used methods are atomic force microscopy (AFM), flow stress, optical tweezers and magnetic tweezers.[76,78–81] In contrast, optical-based approaches for studying mechanical properties of DNA, i.e. single-molecule fluorescence resonance energy transfer (smFRET)[72,82] and tethered particle motion (TPM),[83] rely on light to excite and detect single molecules or measure the motion of a probe attached to a DNA strand.

Atomic force microscopy

The advent of AFM[79] in 1986 introduced a powerful tool to force measurement, imaging and molecular manipulation with atomic resolution requiring no labels. Typically, an AFM system consists of a micro-fabricated silicon or silicon nitride cantilever with a sharp probe (tip) at the end and a laser-beam position sensitive detector. As illustrated in Figure 1.3, when the probe is brought into contact or near contact with a sample surface, forces between the probe and the sample lead to a deflection of the cantilever resulting in a shift of the laser-beam position reflected onto the photodiode. According to Hooke's law,[84]

forces and additional information like surface roughness can be simultaneously measured by detecting the motion of the cantilever while moving along the sample surface. Depending on the application, the AFM can be operated in contact mode for probing sample attributes where the cantilever remains statically in contact with the target sample, as well as non-contact or tapping mode where the cantilever is oscillated at a given frequency.[79]

AFM has been widely used for studying flexibility of DNA in many aspects. Wiggins et al.[80] used high-resolution AFM on individual DNA molecules on length scales between 5 to 100 nm and obtained a direct measurement of the bending energy function appropriate for scales down to 5 nm. Their measurements imply that the elastic energy of highly bent DNA conformations is lower than predicted by classical elasticity models such as the WLC model. Katan et al.[85] managed to visualise the dynamics of nucleosomal structures by using a high-speed AFM (hs-AFM) with a temporal resolution of tenths of seconds. Indeed, AFM has the advantage of directly imaging biomolecules in their natural environment with up to atomic resolution, which is a key limitation of optical microscopy. However, external mechanical stimuli imposed on molecules and relatively low time resolution due to scanning speed limitations narrows the applications of AFM in probing biological system.

Optical and magnetic tweezers

Optical traps and magnetic tweezers are force-based techniques for the manipulation and direct measurements of force and extension on biological macromolecules or the force generated by molecules. Stretching and manipulating a DNA molecule by applying a force around 50 to 65 pN with an optical trap, Smith et al.[76] and Wang et al.[78] have measured the extensibility of DNA with optical traps and obtained the intrinsic persistence length of dsDNA in agreement with the theoretical prediction by the WLC. Alternatively, studies using

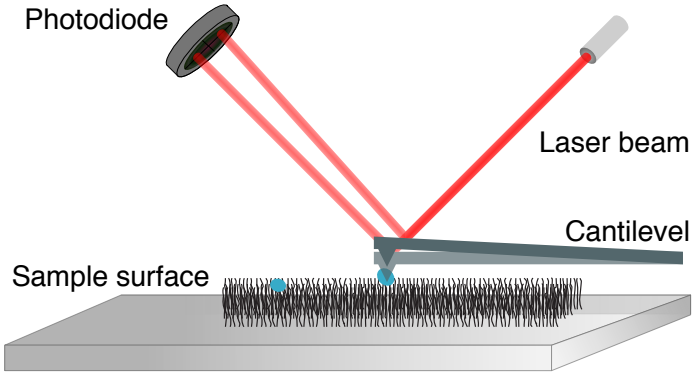


Figure 1.3: Atomic force microscope using beam deflection detection. As the cantilever with a sharp tip is deflected via its interaction with the molecule on surface, the position of the reflected laser-beam will be shifted on the surface of the photodiode detector

magnetic tweezers by Strick et al.[73,86] and Leonhout et al.[87] on investigation of the elasticity and dynamics of DNA supercoiling, which is vital to many genetic processes, have laid the groundwork for DNA-protein interactions.

In an optical tweezers setup, one uses a highly focused laser beam to physically trap a nanometre or micron-sized dielectric bead at the beam waist due to a very strong electric field gradient.[88,89] Being capable of manipulating the bead and precisely detecting its displacements with sub-nanometre precision allows for the measurement of forces applied to the particle, Likewise, the force generated by the molecule attached to the particle, can be calculated by following Hooke's law because the force applied to the bead is linear with respect to its displacement from the trap centre.

For a magnetic tweezers set-up, instead of dielectric beads, a magnetic bead is attached to a tethering surface by the molecule of interest, such as single- or double-stranded DNA. Pulling and torsional force[81] can be applied to study mechanical properties of single molecules by manipulating the magnetic microbead with the help of an external magnetic field.

Despite both forced-based tweezers apparatus being able to access sub-nanometre and microsecond spatiotemporal resolution, and report on rotational

force and torque, the laser beam used in optical tweezers may interact with other particles of the biological sample due to contrasts in the refractive index and therefore lead to additional photodamage and sample heating problems. In contrast, magnetic fields do not affect the sample and the magnetic interaction is highly specific to the magnetic microbeads. However, the range of forces accessible with magnetic tweezers is lower in comparison with optical tweezers and AFM. Nevertheless, intrinsic assay geometry limitations prevent the use of these single-molecule stretching methods on studying the mechanics of very short DNA molecules (less than kilobase length scales). The connection to a micron-sized bead introduces drift and noise from the macroscopic world thus prohibiting access to small conformational changes.[90] Magnetic tweezers use ∼1 to few microns sized beads, and even for optical trapping, people use beads which are ∼250 nm or larger. The probe size does matter to look at different mechanics. Moreover, for all the aforementioned techniques with few exceptions,[91–93] a frequently faced challenge in the context of force measurements is throughput, limiting the obtainable statistics.

Single-molecule fluorescence resonance energy transfer

Single molecule fluorescence resonance energy transfer (smFRET) is an advanced version of FRET wherein single donor and acceptor fluorophore pairs are excited and detected on a single molecule level.[94] In contrast to ensemble FRET, smFRET is capable of resolving the FRET signal of each individual molecule. In 1996, this technique was first developed by Ha and co-workers to reveal the dynamic structural changes of biomolecules[82] and to observe subpopulations in a heterogeneous mixture.[95–97] Recently, Vafabakhsh and Ha[72] developed a fluorescence-based, protein-free assay, by monitoring the cyclisation of single DNA molecules in real time, which reveals the extreme bendability of DNA at the length scales shorter than 100 base pairs. Murphy

and Ha[98] used smFRET measurements of fluorescently labeled oligo-dT to examine the conformational flexibility of single-stranded DNA (ssDNA) and obtain a comprehensive set of data over a wide range of NaCl concentrations (from 25 mM to 2 M) as well as chain lengths (10∼70 nucleotides).

In smFRET measurements, donor and acceptor FRET pairs are typically excited by a laser in order to generate sufficient fluorescence signal from single fluorophores, which are collected by a fluorescence microscope. Thereby, conformational changes and kinetic information of the molecules can be obtained by calculating the FRET efficiency and the relative fluorescence intensity fluctuation of single donor and acceptor FRET pairs. Despite many efforts to maximise the signal to noise ratio, difficulties in FRET pair labelling and intrinsic properties of fluorescent labels such as photoblinking and photobleaching remain distinct limitations for such fluorescence based technique.[94]

Tethered particle motion

Among the various single-molecule manipulating and imaging techniques, a force-free method known as tethered particle motion (TPM) analysis has provided a powerful alternative route to studying internal interactions of biopolymers such as DNA,[99,100] and related molecular processes such as protein-mediated DNA bending[101] and looping[101] in real time. In the TPM approach, a nanoparticle or microsphere is attached to the free end of a single polymer molecule, i.e. DNA strand, of which the other end is immobilised onto a glass surface. The thermal fluctuation induced Brownian motion of the tethered bead is constrained by the tether. Lateral observations by an optical microscope and the use of a single-particle tracking (SPT) method to monitor the (end-to-end) displacements of the reporter bead relative to the anchor point with nanometre precision reveal changes in the effective tether length, thus reporting conformation or elasticity variations.

TPM opens up a new way to quantify the mechanical properties of biopolymers with minimal externally applied force. First published by Schafer et al.[83] in 1991 to measure transcription elongation rate variations, TPM has been extensively studied experimentally[102,103] and theoretically.[104] Lindner et al.[105] have combined TPM with total-internal-reflection and dark-field microscopy and have measured the DNA spring constant using DNA with a contour length of $L = 925$ nm and a gold bead with diameter $d = 80$ nm with 10 nanometre accuracy.

Using TPM to explore the intrinsic bendability of DNA at very short length scales, however, remains challenging. On one hand, the large tethered particle size impedes the investigation of very short DNA molecules due to the volume exclusion effect.[106] Nelson et al. have developed a model and introduced a dimensionless number which is called excursion number N_{R} to determine the regime where the molecule motion is dominant.[104] Nevertheless, a smaller reporter bead is always favourable to minimise influence by the particle on the DNA tether. On the other hand, a tiny reporter bead brings difficulties in single particle imaging and tracking due to the limited sensitivity of optical microscopes and currently available sensors for detection. As shown in Equation 2.13, the Rayleigh scattering from nanoparticles decreases with the sixth power of their diameter, making the use of smaller particles (<40 nm diameter) an experimental challenge.

Despite its resolution limitations, optical scattering provides access to microsecond temporal resolution and sub-nm spatial precision simultaneously as well as a large field of view (FOV) and potentially high throughput. Ueno et al. have demonstrated the ability of dark-field scattering microscopy for imaging and tracking gold nanoparticles (AuNPs) ≥80 nm diameter with nanometre precision and sub-millisecond temporal resolution.[107] Therefore, the central mo-

tivation of this thesis was to explore the detection limit of dark-field microscopy in the context of improving the image contrast and spatiotemporal resolution. An unprecedented level of background suppression is demonstrated by combining evanescent illumination via total internal reflection (TIR) and dark-field microscopy. As an example to use this TIR-based dark-field microscopy method as an improved tool in single molecule studies, I first investigate the bending flexibility of dsDNA on sub-persistence length scales using 20 nm diameter gold nanoparticles as the smallest tethered beads to minimise perturbations on the molecule itself. Furthermore, I extend and experimentally demonstrate the application of dark-field detection method to label-free imaging, developing a novel contrast mechanism based on potentiodynamic phenomenon at interfaces.

This thesis is arranged as follows:

In *chapter 2*, I provide a detailed description of development of the dark-field detection combined with TIR illumination to enable detection and imaging of nanoparticles smaller than 40 nm with simultaneous nanometre localisation precision and microsecond temporal resolution at incident power densities comparable to single molecule fluorescence imaging. A brief introduction to the basics of scattering and evanescent field created via total internal reflection follows. Different implementations are presented and quantitative comparisons of their imaging performance, e.g. signal-to-noise ratio and background rejection, are carried out. Furthermore in this chapter, I describe a surface passivation assay developed for high throughput single-molecule TPM configurations. Finally, image processing methods for high-speed single particle tracking are covered.

Chapter 3 elaborates on TPM experiments of studying the mechanical properties of dsDNA at sub-persistence length scales implemented by a home-built ultra-sensitive total internal reflection scattering microscopy (TIRSM).

The measured elastic property of short dsDNA appears to be more flexible than predicted by WLC. Being capable of resolving and tracking small objects as 20 nm gold nanoparticles with sub-nm spatial and 6 μs temporal resolution, we are able to study much shorter dsDNA tethers ranging from 60 to 160 bp at regimes where the volume exclusion effect is negligible. A computational sorting program for the assessment of various tethered particle behaviours and corresponding selection criteria for determining well-behaved tethers is discussed.

In *chapter 4*, I apply the configuration of short dsDNA tethered and functionalised with charged gold nanoparticles as a molecular sensor. With an externally applied electric field, the stretched dsDNA acts as a nanospring. By characterising its effective spring constant and measuring the deformation via the tethered particle displacement, I measure the electrophoretic force at femtonewton (10^{-15} N) scales and detected the change in electric charge. Further characterisation of the molecular sensor is presented by studying its response to the magnitude of the applied electric field and the binding of supercharged biomolecules to the nanoparticle surface. Change of the zeta-potential due to the variation of pH value is verified and discussed.

In *Chapter 5*, I continue to explore the potential applications of TIRSM in label-free imaging. Optical imaging of the electric double layer around nanostructures on an indium tin oxide (ITO) substrate is experimentally demonstrated based on a contrast mechanism introduced as potentiodynamic optical contrast(PDOC). The material specific electric double layer reconfiguration is the main source for changes to the scattering intensity. This specificity is identified by comparing the different PDOC response to the ITO and chromium substrate. In addition, chloride (Cl^-), bromide (Br^-) and iodide (I^-) anions with different polarisability in solution are used to further validate the contrast

origin.

The final *chapter 6* presents a short summary of the contents of this thesis and provides an outlook for future work and the potential applications based on the methods demonstrated here.

Chapter 2

Materials and methods

This chapter describes the developments and experimental methods used throughout this thesis. All work presented in this chapter was performed by myself.

2.1 Single molecule tracking

Single molecule tracking involves detection and localisation of target molecules by linking particle coordinates between frames in a stack of sequential images. It is a key method to study diffusive dynamics of proteins and related biological processes such as receptor recognition and signal transduction within the cell. This method provides a distinct benefit of quantifying the nanoscopic behaviour of one molecule at a time compared with ensemble measurements.[108,109] However, the extremely small scattering cross sections of proteins have hindered the extension of conventional optical microscopy to label-free single-molecule imaging and tracking.

Most progress in this context has been achieved using fluorescence-based single-molecule detection. Fluorescence microscopy has been widely used in single molecule level tracking and imaging for more than 30 years due to its remarkable background suppression.[110–114] The use of fluorescent probes including organic molecular dyes, fluorescent proteins and semiconductor nanocrystals

attached to the molecule of interest overcomes the detection boundaries by separating the excitation light from emitted fluorescence signal, which has a longer wavelength; thus, significantly decreasing the levels of imaging background. In this case, limitations to signal-to-noise ratio are mainly determined by the maximum number of photons which a single fluorescent probe can emit in combination with other hardware factors such as dark counts and read-out noise of detectors as well as illumination source fluctuations.

Irrespective of hardware improvements, it is essential to optimise the level of background suppression to maximise the sensitivity. In a conventional wide-field optical epifluorescence microscope, inherent autofluorescence of molecules within the cell and emission from un-bound probes make a significant contribution to out of focus background which deteriorates the signal-to-noise ratio (SNR). To deal with such a problem, confocal approach is one of the solution that originally developed by Marvin Minsky in the mid-1950s.[115] Spatial filtering with detector aperture is the key strategy to exclude excessive out of focus light and background noise in confocal microscopy and various spatial filtering techniques[116,117] with respect to the geometry of detector apertures are applied accordingly in practical applications. An alternative way to optimise background rejection is to take advantage of the refractive index difference between glass and water in order to reach TIR at the interface.

Although not the first person[118] who proposed the idea of using TIR to study the contacts formed between cells and solid surfaces, Daniel Axelrod is believed to play a key role in the development and promotion of this technique in the early 1980s as TIRF microscopy.[119–122] Its advantages of offering high-contrast and high-resolution images at or near the plasma membrane,[123] making it the gold standard technique for investigating events in many varied areas of cell biology including endocytosis,[124–127] exocytosis,[128–130] cell adhesion,[131–134]

and cytoskeletal dynamics.[135–138] Total internal reflection gives rise to an evanescent field at the interface that decays exponentially with restricted propagation distance from the interface towards the aqueous side.[139] Therefore, high SNR images with significantly reduced background can be recorded as only fluorophores within the evanescent field are illuminated and excited. Beyond its superior background suppression, total internal reflection fluorescent microscopy provides high axial resolution which enables the observation of molecular dynamics.[140–142]

However, study of fast dynamics or processes that span multiple orders of magnitude in time is not achieveable with single-molecule fluorescence as the contrast mechanism due to the photochemical instability of fluorophores. Even under specifically chosen conditions to suppress photobleaching, the time over which a specimen can be observed by single-molecule fluorescence measurements is still limited to a few minutes. As with irreversible photobleaching, the presence of off-states when the fluorescence intensity intermittently and reversibly drops to zero, referred to as photo-blinking, interrupts the tracking of molecules. Moreover, limited photon flux emitted from single fluorescent probes is problematic for high precision and fast single molecule tracking.

Given these limitations, contrast mechanisms based on scattering provide an alternative route to single molecule tracking that do not suffer from those aforementioned drawbacks,[143–147] but at the expense of larger and thus more perturbable labels. Dark-field detection is the background-free scattering-based equivalent to fluorescence detection enhancing image contrast by producing a dark background.[148,149] In typical dark-field microscopy, the illumination light is partially blocked by a specially sized disc and rejected from the detection path. Only light scattered by the sample will be collected by the objective lens and the unscattered beam is excluded from the image thus forming an image

of a dark background with bright objects. In this respect, the SNR is limited by the background rejection efficiency and the contrast is determined by the scattering cross sections of the sample. The detected photon flux is ultimately only limited by the amount of light incident on the sample.

2.2 Total internal reflection dark-field scattering microscopy

Total internal reflection and the evanescent field

Whenever light travels between two transparent media with different refractive indices, it will be partially reflected and partially transmitted at the interface. When light initially travels through the more highly refractive medium (e.g. cover glass, $n_{\mathrm{g}} = 1.52$) to a less dense medium (e.g. water, $n_{\mathrm{w}} = 1.33$) at a sufficiently oblique angle, total internal reflection occurs. The light will be totally reflected at and above an incidence angle (measured from the normal to the interface) which is called the critical angle. Defined by Snell's law, the critical angle of incident light can be easily calculated as follows:

$$c = \sin^{-1}(\frac{n_1}{n_2}) \tag{2.1}$$

where n_1 and n_2 are the refractive indices of the medium and the coverslip respectively.

At the occurrence of TIR, according to the physical theory about the electromagnetic field which cannot be discontinuous at a boundary, a thin, non-propagating electromagnetic field known as the evanescent field, is produced at the interface by this TIR phenomenon.[139] In standard electromagnetic theory, a set of coupled partial differential equations aslo known as Maxwell's equations provide a mathematical model for the wave equation for both electric and

magnetic fields.[150–152] For the electric field and its associated magnetic field of the electromagnetic wave in a homogeneous dielectric medium,

$$\left(\frac{\partial^2}{\partial \mathbf{x}^2} - \frac{\varepsilon}{c^2}\frac{\partial^2}{\partial t^2}\right)\mathbf{E}(\mathbf{x},t) = 0 \tag{2.2}$$

$$B = \frac{2\pi cn}{\omega}k \times E \tag{2.3}$$

where in Eq. 2.2 ϵ is the dielectric constant, E(x,t) is the amplitude of the electric field vector at the position x and time t, c is the speed of light in vacuum. For Eq. 2.3, $n = \sqrt{\varepsilon}$ is the refractive index of the medium, k is the wavenumber of the wavevector $\boldsymbol{k}$ pointing in the direction of wave propagation and ω is the angular frequency.

When light travels from a medium of higher refractive index n_1 to a less dense material of lower refractive index n_2, it will be partially reflected and partially transmitted at the interface. Thus, we have incident and reflected waves on one side in the first medium, and transmitted waves on the other side of the interface in the second medium. All three waves are plane waves described by Eq. 2.2 with their own field amplitudes E_{0in}, E_{0r} and E_{0t}. The solutions to Eq. 2.2, however, are different on the two sides due to the discontinuity in the medium,[153]

$$\begin{aligned}
\mathbf{E}_{in}(\mathbf{x},t) &= \mathbf{E}_{0in}e^{2\pi i n_1 \mathbf{k}_{in}x - i\omega \mathbf{t}} \\
\mathbf{E}_{r}(\mathbf{x},t) &= \mathbf{E}_{0r}e^{2\pi i n_1 \mathbf{k}_{r}x - i\omega \mathbf{t}} \\
\mathbf{E}_{t}(\mathbf{x},t) &= \mathbf{E}_{0t}e^{2\pi i n_1 \mathbf{k}_{t}x - i\omega \mathbf{t}}
\end{aligned} \tag{2.4}$$

where $\boldsymbol{k}_{in}$, $\boldsymbol{k}_r$, $\boldsymbol{k}_t$ are wave vectors of the incident, reflected and transmitted waves, respectively.

Their directions are determined by the laws of reflection and refraction. The angle of refraction can be calculated by Snell's law:

$$cos\varphi = \sqrt{n_2^2 - n_1^2 sin^2\theta} \tag{2.5}$$

and it only exists for angles of incidence θ smaller than the critical angle θ_c given by

$$sin\theta_c = \frac{n_2}{n_1} \tag{2.6}$$

For incidence angles exceed the critical angle, total internal reflection occurs and only incident and reflected waves remain. Because Maxwell's equations impose a boundary condition of continuity at the interface, the transmitted wave is transformed into a non-propagating electromagnetic field known as evanescent wave. To verify this, consider the coordinate system where the interface between the media lying in the $x-y$ plane and the plane of incidence to be the $x-z$ plane, we can get the scalar product in the exponent of the propagation factor for the transmitted wave,[153]

$$in_2k(xsin\varphi + zcos\varphi) = ikxn_1 sin\theta - kz\sqrt{n_1^2 sin^2\theta - n_2^2} \tag{2.7}$$

Then the solution becomes

$$E_t(x,t) = E_{0t} e^{-i\omega t} e^{2\pi i n_1 k x sin\theta} e^{-2\pi k z \sqrt{n_1^2 sin^2\theta - n_2^2}} \tag{2.8}$$

The first exponential term is the standard oscillatory term that describes the time dependence of the wave. The second term indicates that evanescent wave propagates along the interface. However, it should be noted that nothing actually propagates, it is the electromagnetic energy moving back and forth through the interface forms a picture of a wave traveling on the surface. The last term on the right-hand side of Eq. 2.8 tells the amplitude of the evanescent wave decays exponentially with the distance from the interface towards the less

dense medium. Its intensity $I(z)$ decays exponentially as a function of distance away from the interface from the aqueous side,

$$I(z) = I_0 e^{-\frac{z}{d}} \tag{2.9}$$

The penetration depth of this evanescent wave is described by a function of the incidence angle (θ) and excitation light wavelength (λ) and the indices of refraction of the two media.

$$d = \frac{\lambda}{4\pi\sqrt{(n_1 \sin(\theta))^2 - n_2^2}} \tag{2.10}$$

Technically, the depth can be up to 200 nm from the glass-aqueous boundary but usually ranges from 40 to 100 nm.[107,154,155] In most live cell imaging, the excitation area is restricted to the distance near the glass-aqueous interface, which is the reason why TIR significantly reduces the background compared to epifluorescence microscopy. In my setup for the glass-water interface, the critical angle is 61.5° which in turn leads to an illumination depth of about 100 nm above the interface can be achieved.

Dark-field detection

In optical microscopy, dark-field illumination is a widely used imaging technique for rendering unstained biological materials whose refractive indices are very to their surroundings clearly visible. Figure 2.2 shows the diagram of an inverted dark-field microscopy compare with a bright-field microscope. In a conventional dark-field microscope, an opaque light stop is placed at the centre in the illumination path to form a hollow cone of light and a condenser lens is used to direct the illumination towards the specimen; thus forming an image in which the sample in the entire field of view appears bright against a dark background.

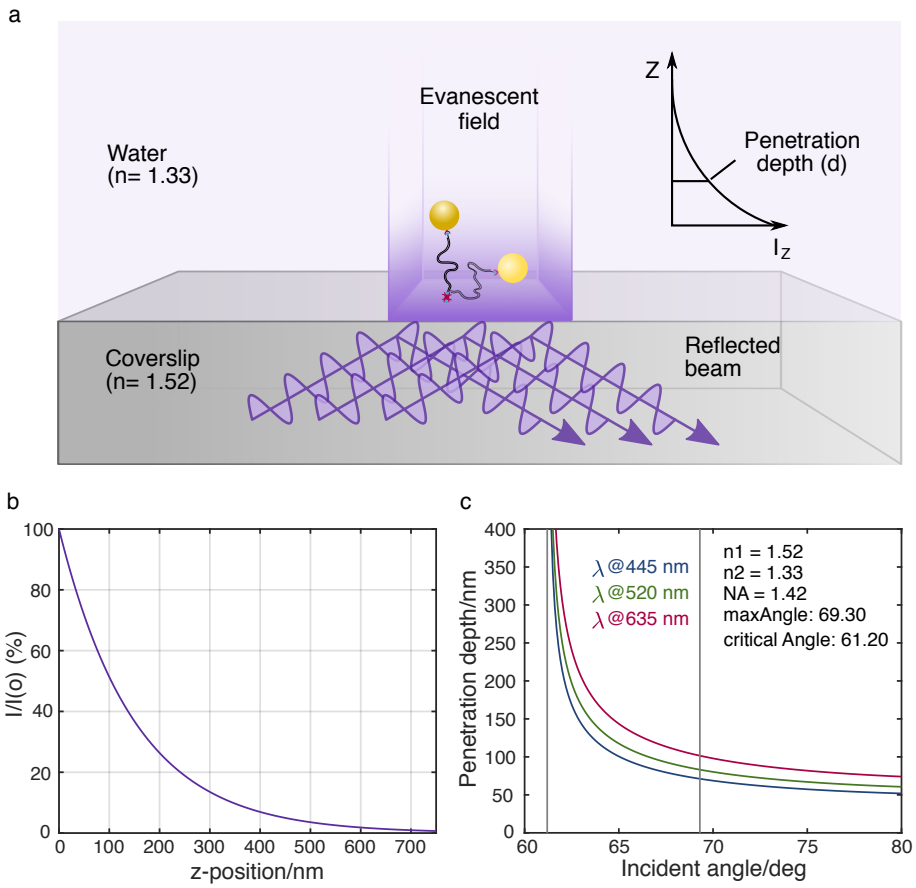


Figure 2.1: Evanescent field and penetration depth. (a) Evanescent field generated at the glass-water interface by total internal reflection, TIR only occurs when light initially travels through the more highly refractive medium to a less dense medium beyond a critical angle. (b) The intensity of the evanescent field decays exponentially as a function of the distance away from the interface as in (a). (c) Evanescent illumination depth dependence on the incident angle (θ), excitation light wavelength (λ) and the indices of refraction of the two media. Calculation based on glass (n_1=1.52) and water (n_2=1.33).

The detected intensity of the light scattered by the sample I_{det} is given by

$$I_{det} = I_{inc}[\zeta^2 + |s|^2 + 2\zeta|s|\cos\varphi] \tag{2.11}$$

where I_{inc} is the incident intensity, ζ^2 is the transmissivity of the glass-water interface, s is the scattering amplitude of the object, and φ is the phase difference between the reflected and scattered fields. For dark-field microscopy, the detected intensity is dominated by the purely scattering term, $|s|^2$, while

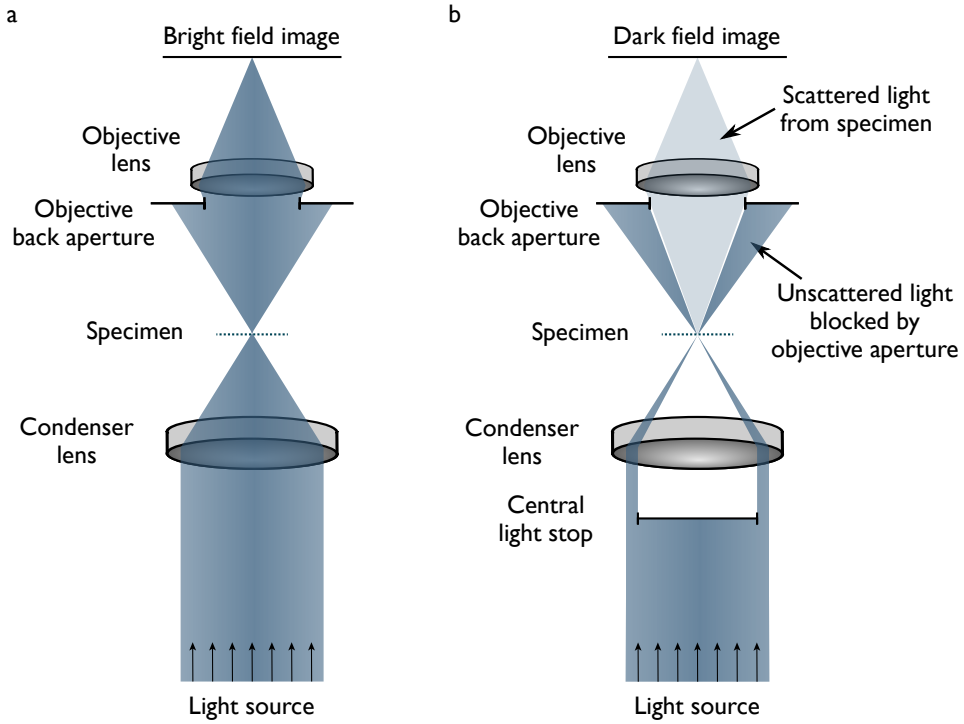


Figure 2.2: Diagram showing the difference between bright-field microscopy and dark-field microscopy. (a) Diagram of a conventional bright-field microscope. The recorded image is typically a dark sample on a bright background. (b) Diagram of an inverted dark-field microscope. An opaque light stop is inserted in the central illumination path to generate a hollow cone of light. The unscattered light is therefore excluded by the objective and only light scattered from specimen will be collected. Samples in dark-field microscopy image appear bright against a dark background.

the remaining terms are negligible for sufficiently weak scatters. The detected signal can therefore be expressed as $I_{\text{det}} = I_{\text{inc}} \cdot |s|^2$. Therefore, regardless of background from glass roughness, and stray light from optical imperfections, for an optimised dark-field experimental setting under shot noise conditions, the contrast scales with the total number of detected photons and the signal-to-noise ratio is determined by the fluctuations in the background induced by shot noise as

$$S \propto \sqrt{N} \tag{2.12}$$

For Mie scattering by a spherical particle $D \ll \lambda$ (D is the particle diameter),

the scattering amplitude can be written as:

$$s(\lambda) = \eta\alpha(\lambda) = \eta\varepsilon_{med}(\lambda)\pi\frac{D^3}{2}\frac{\varepsilon_{part}(\lambda) - \varepsilon_{med}(\lambda)}{\varepsilon_{part}(\lambda) + 2\varepsilon_{med}(\lambda)} \tag{2.13}$$

where $\varepsilon_{\mathrm{med/part}}$ denotes the complex dielectric constants of the medium and particle. For the pure scattering term, $|s|^2$, the resulting intensity of scattered light is proportional to D^6, which means a halving in the size of the scattering particles leads to a 64-fold intensity reduction.

Equation 2.12 implies that in principle the SNR can be improved by detecting more photons. As a result, a higher localisation precision, temporal resolution and sensitivity can be achieved by indefinitely increasing the amount of light incident on the sample. However, this is impossible in practice since biological specimens are susceptible to phototoxicity and heat accumulated by the photothermal effect. Ignoring the photodamage, purely scattering based imaging contrast has the capability of high-speed tracking with down to microsecond temporal resolution. This in turn leads to the topic of my research of merging advantages of total internal reflection fluorescence microscopy (TIRFM) and dark-field to explore the advantage of high-speed single particle tracking to label-free imaging.

Pure scattering

The entire TIRSM setup is built on a large and heavy breadboard to optimise the portability and then placed on a vibration isolated optical table spaced with air-filled tyres to minimise the vibrations from the environment being coupled into the microscope (Figure 2.13). Despite the simplicity of the optics for a dark-field microscope, all components except for electronics are precisely aligned and mounted to allow for sub-nm tracking precision. Finally, the setup is fully enclosed into compartments to eliminate any possible background

light and illumination beam instabilities induced by air flow. Even though there are different methods to implement TIRSM in terms of the geometry to achieve TIR and the technique to exclude the illumination and reflected beam, alignments of illumination and detection pathway are identical for those variants. To simplify the explanation of the alignment procedure, here I outline the process based on the version with two micromirrors-based coupling of incident and reflected illumination light with optimised mirror diameters and objective mirror separation.

The construction of the dark-field scattering channel can be divided into three stages in sequence: alignment of the illumination path, alignment of the detection arm and optimisation of background rejection. Three laser diodes are selected as illumination sources by taking their maximum power output, lower coherence length and high mechanical stability into account. Each of them has a distinct wavelength of 445, 520 and 635 nm for various applications (*Lasertack*, LDM-445-6000-C, LDM-520-1000-C, LDM-635-200-C). For example, the green laser is mostly applied for high-speed tracking of gold nanoparticles due to their plasmon resonance enhanced light scattering. Three illumination beams are combined in a plane parallel to the optical table at a certain height via dichroic mirrors before introducing the incident micro-mirror. Considering the relatively uniform beam profile coming out of these laser diodes and further requirements for a higher laser power output, instead of cleaning the beam by either coupling into a single-mode fibre or spatially filtering the beam through a pinhole, all excitations are expanded and collimated by a telescope system comprised of two lenses and attenuated by neutral density filters (ND). Finally, the expanded beam profile is cut to a diameter of approximately 5 mm full-with at half-maximum (FWHM) via an iris.

To enable precise tilt correction, the incident micro-mirror is glued on a

3D printed mirror holder, mounted on a high stability kinematic mirror mount and then placed into the illumination path. The height is carefully adjusted to ensure the illumination beam hits onto the area close to the tip of the micro-mirror. This allows for the maximal mirror separation in the following step so that minimal blockage of numerical aperture and loss of scattered light can be achieved. In the meantime, an iris is mounted at the same height after the incident micro-mirror as a reference for future alignment of the second micro-mirror.

The beam reflected by the incident micro-mirror is aligned so that it travels straight upwards and through the centre of the objective. To achieve a straight vertical beam-path, a lens tube with two irises mounted on both sides is screwed into the place where the objective sits. When the reflected beam travels through the centre of both irises, a target being marked in its place on the ceiling serves as a reference for later beam positioning. Next, the objective is inserted into the vertical beam path and moved around until the beam hits the ceiling target. A 200 mm focal length lens (*Thorlabs*, LA1708-A) is then positioned into the excitation path without introducing beam displacements relative to the ceiling target. It is moved back and forth until the beam size projected onto the ceiling is the smallest to ensure that the lens focuses the beam into the back focal plane (BFP) of the objective.

To begin the alignment of the detection path, a 45° mirror is first introduced underneath the objective to pick up the scattered light. For precisely adjusting its position and correcting the tilt, an additional alignment laser is applied from the camera side and collimated to travel straight in a plane parallel to the optical table towards the 45° mirror. The objective is removed and replaced by a flat mirror (*Thorlabs*, PF10-03-P01) inserted in its place, the 45° mirror is adjusted until the reflected beam from the mirror overlaps with the excitation

beam. Finally, moving around the 45° mirror on the table to ensure the position of reflected excitation beam on the ceiling has no displacement relative to the target in the absence of flat mirror.

To align the camera (*Pointgrey*, Grasshopper3 GS3-U3-32S4M), the objective is inserted back but with a ring-actuated iris diaphragm attached to the back aperture. A torch light is mounted on top close to the objective front lens and the diameter of the iris is tuned to achieve a reasonably small beam spot by cutting off the diverged light through the objective. After that, the camera is mounted to ensure the sensor is perpendicular to the imaging path and aligned so that the beam spot targets precisely the middle of the sensor chip. Next, an imaging lens selected on the basis of required magnification, for applications discussed in this thesis a 200 mm focal length lens (*Thorlabs*, AC254-200-A), is introduced at the appropriate focal distance away from the camera sensor without causing beam displacements on the camera chip. Special care is taken for proper positioning of the imaging lens. The distance between the lens and the camera sensor is deemed correct when the beam profile has the largest intensity and smallest area for an incident collimated beam. It is worth remarking that the imaging lens is placed as close as possible to the objective to improve the scattered light collection and reduce the loss of numerical aperture.

Finally, with the excitation and detection path aligned, the second micro-mirror mounted in the same way as the incident one is placed under the objective back aperture opposite to the incident micro-mirror. Tilt correction of the reflected beam coupling micro-mirror is performed by placing a coverslip on the objective and shifting the incident micro-mirror to achieve total internal reflection. When the TIR occurs, it is adjusted until the reflected beam travels through the reference iris mounted in previous procedure. Background rejection is optimised by checking the image of a coverslip with the camera and moving

around both two micro-mirrors. Background suppression is deemed optimised when the background noise is lowest while the SNR is the highest.

Fluorescence channel

The TIRSM setup compatible with simultaneous fluorescence imaging. Instant switching to TIRFM is achieved by simply applying a long pass or band pass filter as long as the excitation beam can be separated from the emission spectra. Multiple filters are inserted into an automatic filter wheel mounted in front of the imaging camera so that switching between scattering and fluorescence channel and different fluorescence excitations can be implemented without opening the enclosure. It is advantageous to keep the fluorescence channel in combination with the scattering channel to provide additional spatial information. For example, doubly labelling on head domains and simultaneously tracking of a 20 nm gold nanoparticle in scattering and a quantum dot in fluorescence is applied to investigate the transient states for both heads of myosin 5a molecules travelling along a actin filament.[145,156]

Focus channel

The focus plane is stabilised by taking advantage of the total internally reflected beam based on the principle that drifts in focus plane, in terms of the displacement between the sample and the objective, translate into shifts of the reflected beam imaged on a position detector. An infrared laser ($\lambda = 830$ nm, *World Star Tech*, VH5-30G-850, 30mW) is chosen for focus control channel excitation beam in consideration of its distinct wavelength far away from the plasmonic resonance frequencies of gold and silver particles to minimise the influence of auto-focus illumination beam on the sample. The focus control beam is first aligned and coupled into the illumination arm with the aid of two mirrors mounted on high precision kinematic mirror mounts to ensure that

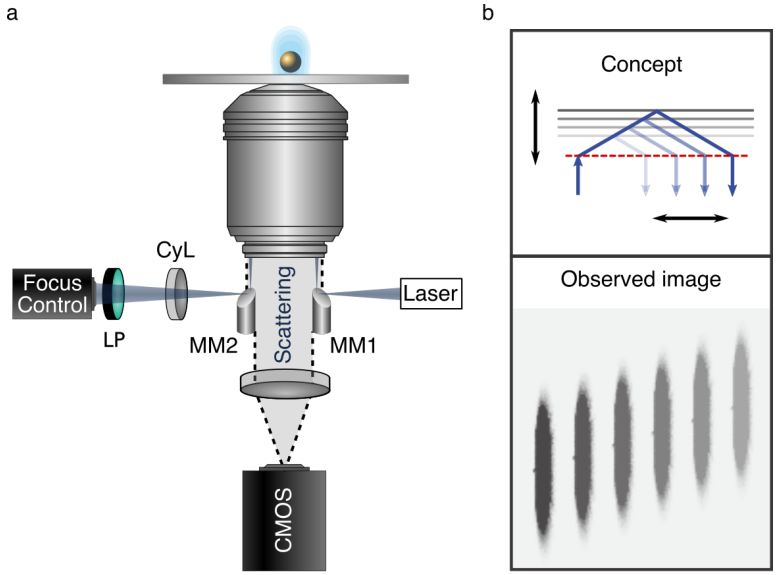


Figure 2.3: Focus control channel. (a) Schematic of focus stabilisation implemented in TIRSM set-up. MM1&2: Micro-mirror, CyL: Cylindrical lens, LP: Longpass filter. (b) Concept and expected signal observed in focus control channel. Vertical arrow: axial displacement; Horizontal arrow: corresponding axial displacements detected in the focus control channel.

the beam travels straight and in the plane parallel to the optical table. As long as TIR appears at the interface, the reflected beam is picked off by the second micro-mirror and introduced onto a focus control camera (*PointGrey*, Firefly USB 2). Next, a cylindrical lens (*Thorlabs*, LJ1363RM-A) is used instead of a normal lens to stretch the projected beam on the camera with an elongated profile for improved determination of its centre position. Moreover, in order to improve the sensitivity of the imaged beam to lateral displacements, it is essential to place the cylindrical lens off focal distance to the camera sensor. The focus feedback associated with the beam displacement on the camera is extracted by calculating the centre of mass of the linear beam profile after summing over all camera rows. To eliminate contributions from other illumination wavelengths, a long pass filter (*Thorlabs*, FGL780) is applied in front of the camera. Note that high stability of illumination beam is required since this approach is sensitive to beam profile and intensity fluctuations which

in turn may lead to unwanted beam displacements hence deceptive changes in focus.

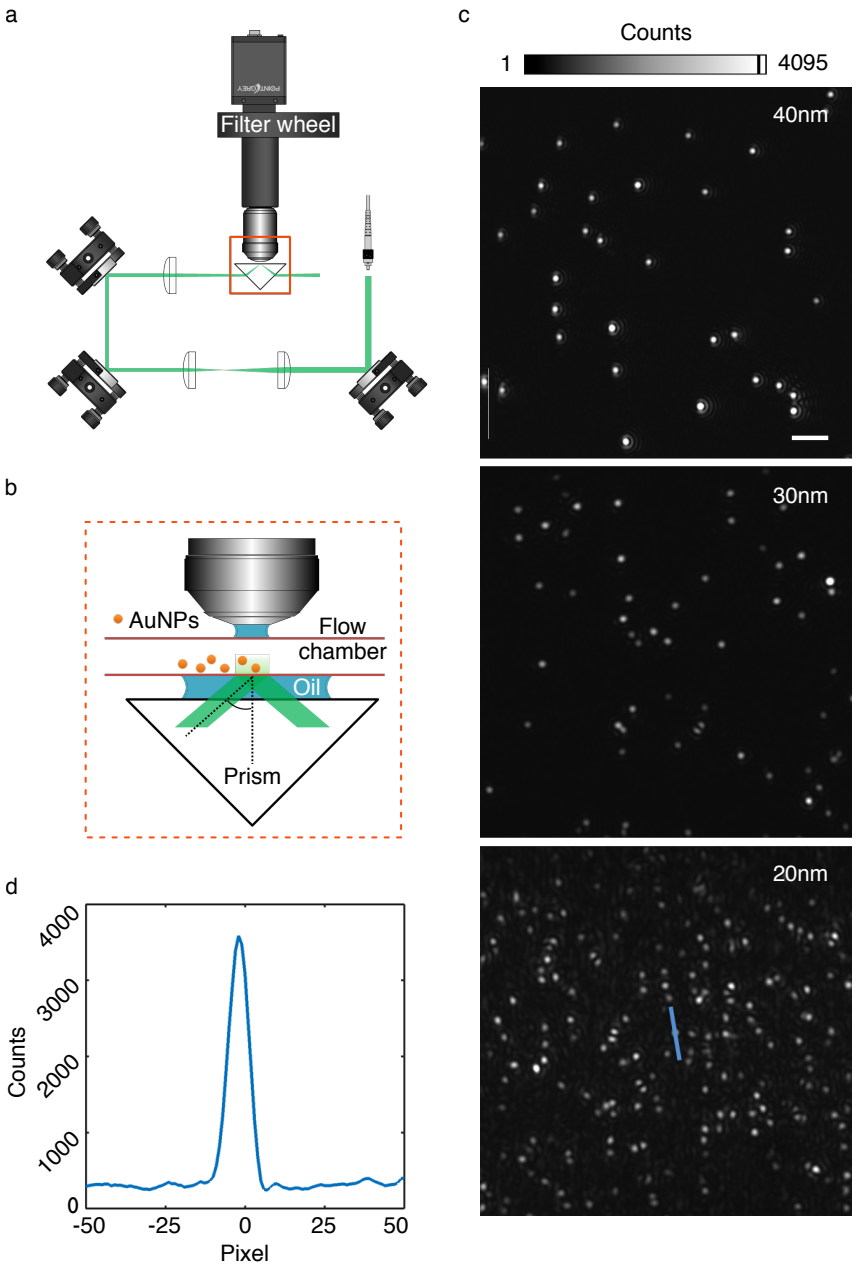


Figure 2.4: Prism geometry based TIRSM set-up. (a) Schematic of Prism-type TIRSM set-up. (b) Illustration of details with the red area in (a), showing total internal reflection and the evanescent field. Only the sample within the evanescent field will be excited. (c) Scattering light images of 40, 30, 20 nm gold nanoparticles acquired via Prism-type TIRSM set-up. Recorded with 1.5 kW/cm^2 incident intensity at 1 ms, 5.6 ms and 64 ms exposure time respectively. The exposure time was set to match D^6 dependence of the scattering cross section on particle size. Scale bar: 4μm. (d) Intensity linecut of a 20 nm AuNP in (c).

Effects of motion blur on imaging

Particle tracking suffers from many detection errors. In particular, errors in particle position localisation and trajectory linking lead to inaccurate characterisation of probe particle dynamics and result in significant systematic biases that affect the interpretations of measured physical observables.[157,158] Savin et al. quantified various sources of errors and separated them into two categories: "static" and "dynamic".[159,160] The "static error" is mainly due to the image signal noise, e.g. dark counts and read-out noise of detectors, and arises even in the position measurements of immobilized particles. While the "dynamic error" occurs when imaging fast diffusing particles, as a result of motion blur, due to finite camera exposure time.

The contribution of motion blur to the localisation error depends on the dynamics of the observed moving particles. It becomes problematic when measuring the position fluctuations of a nanoparticle undergoing Brownian motion, where even fast imaging methods can have long integration times with respect to the relevant time scale.[158] As a consequence, i) fast-moving particle spreads out its emission photons over many pixels and thus result in blurring of the PSF,[161] which makes detecting the genuine rapid motion of the nanoparticle difficult (Fig. 2.5a) and ii) at long exposure times σ with respect to the relaxation time τ of the particle, motion blur causes the shrinking of scatter plots and an underestimation of the variance of the measured particle position distribution (Fig. 2.5b), which in my case predicts that the dsDNA molecule appears stiffer.[162]

Taking the advantage of my ultrasensitive TIRSM setup to track single particle with simultaneous high signal to noise ratio and high spatiotemporal resolution, throughout this thesis (unless specified otherwise), camera exposure time is set to 6 μs which is its lower limit to avoid motion blur effect.

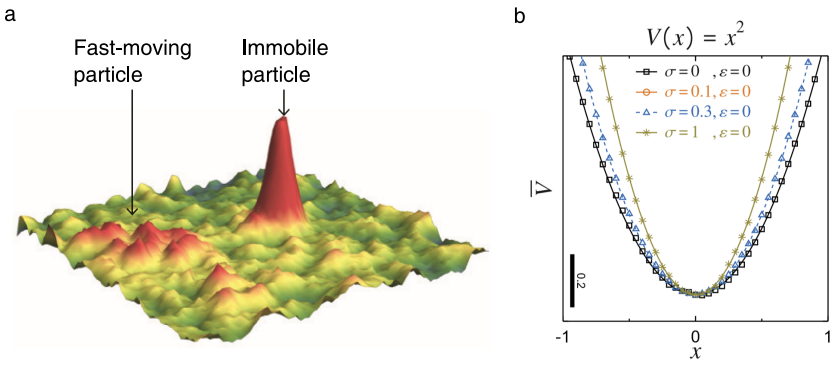


Figure 2.5: The effects of motion blur on imaging. (a) Motion blur effect results in blurring of the point spread function of a fast-moving particle as it spreads out its emission photons over many pixels during acquisition of a frame. In contrast, a slow-moving or immobile particle will appear as a well-shaped PSF and thus readily be detected. (b) In the absence of static errors ($\varepsilon = 0$), motion blur causes the shrinking of scatter plots (with the increase of shutter time τ) and an underestimation of the variance of the measured particle position distribution. Panel a adapted from reference 161 with permission. Panel b adapted from reference 162 with permission.

Nevertheless, I calculate the relaxation time of the particle to compare with 6 μs exposure time to show that snapshots of the particle are captured and corrections for detector time-averaging effects is not necessary in my measurements.[163] I acquired the motion of one particle using different exposure times $\sigma > \tau$. The variance S_r^2 obtained from the corresponding radial probability density function P(r) is 755.8 nm^2 and 198.8 nm^2 for exposure time 200 μs and 1 ms, respectively. Using the equation derived by Wong et al.,[158]

$$var(X_m) = var(X)S(\alpha) \tag{2.14}$$

$$S(\alpha) = \frac{2}{\alpha} - \frac{2}{\alpha_2}(1 - exp(-\alpha)) \tag{2.15}$$

where var(X)= $\kappa_B T/\kappa$ is the true variance. Here, the spring constant of confinement κ can be expressed in terms of the drag coefficient γ as[164]

$$\kappa = \frac{\gamma}{\tau} \tag{2.16}$$

with $\gamma = 6\pi\eta r$ for a sphere of radius r in a solution of viscosity η. A fit of S_r^2 vs. σ to Eq. 2.15 gives the relaxation time of the particle, $\tau = 72.1 \pm 9.2$ μs.

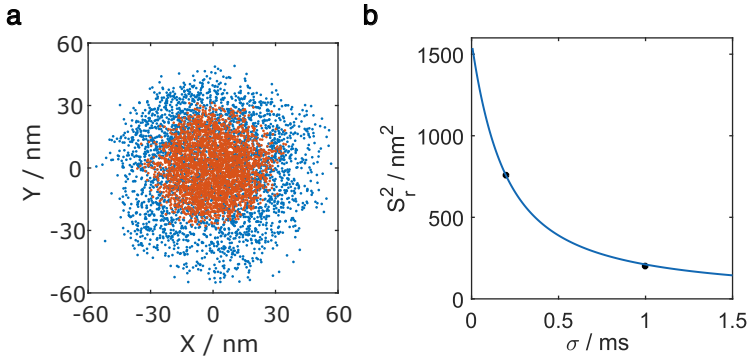


Figure 2.6: Effect of exposure time σ on the measured probability density distributions. The scatter plots were imaged from one same particle using exposure times, $\sigma = 200$ ms (blue) and 1 ms (orange). (a) 2D scatter plot of particle positions (3000 frames in each case). (b) A fit of variance vs. exposure time works out the relaxation time of the particle.

2.2.1 Implementations of total internal reflection and background rejection

For biologically compatible applications, TIR illumination is usually achieved by two different ways known as prism-based and through-objective illuminations. In prism-based TIR, the illumination beam and scattered light travel through different optics, while in the case of the through-objective type, one objective with high numerical aperture is shared to generate TIR at the interface and to collect light from the sample.

Prism type

With regard to the construction of a prism geometry based TIRSM setup, a right angle prism (*Edmund Optics*, #32-544) is used to introduce the excitation beam towards the glass-water interface at or beyond the critical angle. In Figure 2.4a,b, light travels horizontally from one side and enters the prism, being refracted upwards towards the normal. The angle of incidence is 45°, and

the angle of refraction is 27.7°. The light ray is now travelling at an angle of (45 - 27.7) = 17.3° above the horizontal towards the top surface of the prism, which results in an angle of incidence of (90 - 17.3) = 72.7°, greater than the critical angle of 61.5° for the glass-water interface. In Figure 2.4b, a portion of the energy of the incident light will be converted to form the evanescent field originating at the glass-water interface. Immersion oil between the coverslip and the top side of the prism prevents mismatch of refractive indices between aqueous samples and the prism.

Objective type

An objective-type TIRSM has been built as well for comparison purpose, which is based on the widely used through-the-objective TIRFM. In order to optimise light collection and scattering background suppression, the conventional configuration is slightly modified by inserting a perforated mirror customised with two holes close to the objective back aperture at 45° (Figure 2.7b), so that images of scattered light from objects is collected with exclusion of the reflected beam. Figure 2.7a depicts the construction schematically, the collimated laser beam is coupled out of a fibre and focused onto the periphery of the objective back focal plane passing through the holes on the mirror by a wide field lens (WFL). In this implementation, both excitation and reflected light and scattered light from the sample travel through the same objective shown in Figure 2.7b. Hence, a high numerical aperture objective (*Olympus*, PLAPON 60x 1.42NA Oil Immersion) has to be used so that light is incident on the sample at an angle greater than the critical angle.

Micro-mirror type

An alternative to exclude the total internally reflected beam from the detection path can be achieved with two individual micro-mirrors based on the through-

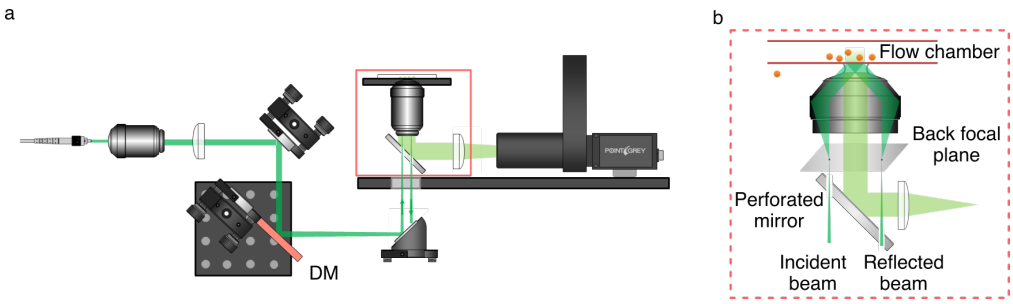


Figure 2.7: Objective-type TIRSM set-up using perforated mirror. (a) Schematic of Objective-type TIRSM set-up using perforated mirror. DM: Dichroic mirror. (b) Illustration of details with the red area in (a), the laser beam is focused onto the back focal plane of a high-NA objective to achieve TIR. The scattered light from samples excited by the evanescent field is collected by the same objective.

objective geometry. For the micro-mirrors based configuration, a compromise between objective high numerical aperture and large back aperture associated with its magnification has to be considered. A high numerical aperture is essential for introducing the incident beam beyond the critical angle at the interface and beneficial for higher collection efficiency of scattered light; whereas the large back aperture significantly facilitates the alignment process. As a result, an Olympus PLAPON 60× infinity-corrected oil-immersion objective is selected for this setup. Two 3 mm rod mirrors (*Edmund Optics*, #54-094) with 45° reflecting surface are selected on the basis of efficient reflection area and minimal loss of numerical aperture. To produce evanescent illumination, as shown in Figure 2.8, the incident laser beam is introduced to the outer edge of the objective back aperture by translating the position of the incident micro-mirror. The second micro-mirror is mounted on the opposite side in order to pick off the reflected illumination light from the scattering image. In contrast to the perforated mirror, scattered light from the sample is reflected onto the camera by a flat mirror aligned at 45°.

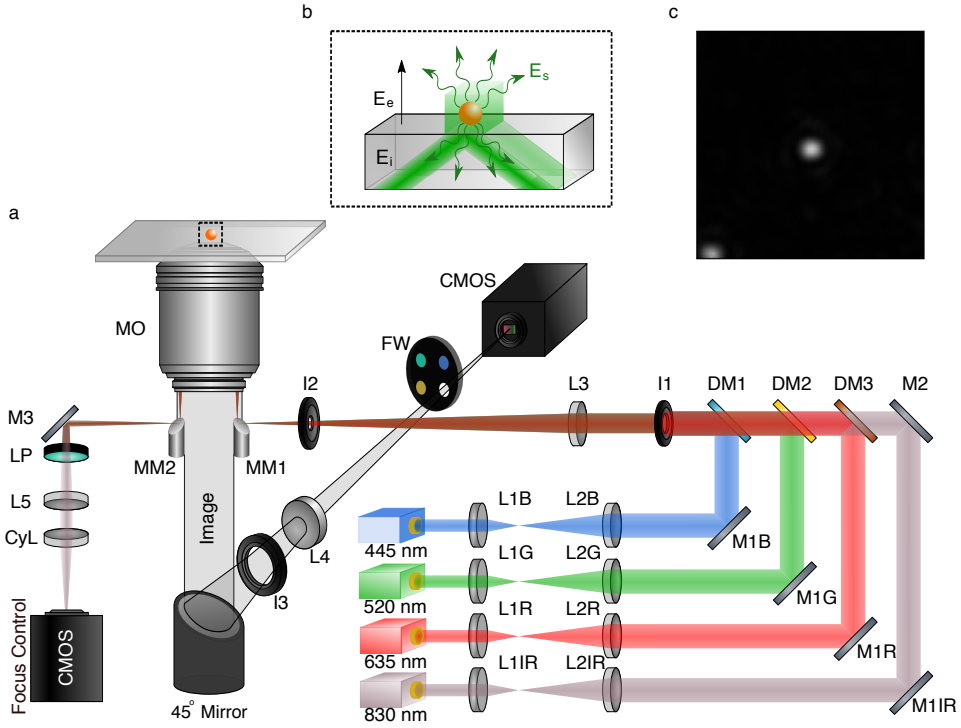


Figure 2.8: Objective-type TIRSM set-up using two micro-mirrors. (a) Schematic illustrating the Objective-type TIRSM set-up implemented with two micro-mirrors. L1-5: Lenses. M1-3: Flat mirrors. DM1-3:Dichroic mirrors. I1-3: Irises. MM1,2: Micro-mirrors. MO: Microscope objective. CyL: Cylindrical lens. LP: Longpass filter. FW: Automatic filter wheel. (b) Signal generation for total internal reflection-based dark-field microscopy: The 20 nm gold nanoparticle on the microscope coverslip is excited by the evanescent field, $E_\mathbf{e}$, generated by the total-internally reflected incident light, $E_\mathbf{i}$, and light scattered from the nanoparticle, $E_\mathbf{s}$, is collected by the microscope objective. (c) Scattering image of a 20 nm gold nanoparticle detected by TIRSM. The particle appears as a bright spot over a dark background. Intensity scale in arbitrary units.

Quantitative comparison of Prism-type vs. Objective-type

Each of these variants presents unique advantages and disadvantages. The prism-based geometry was shown to generate a clean evanescent wave, whereas in the case of through-objective geometry, the evanescent wave is contaminated with stray light. To assess their performance in terms of light collection efficiency and background light suppression, I produced a flow chamber from a thin coverslip (*Marienfeld*, High Precision Glass Coverslip 24 × 50 mm, #1.5H, Cat#0107222) and a top glass slide (*Marienfeld*, High Precision Glass

Coverslip 24 × 24 mm, #1.5H, Cat#0102062) bonded by double-sided scotch tape (3M) of 80 μm thickness to contain the sample. However, due to the limit of the working distance (0.17 mm) of the same objective used in both configurations, two cover glasses are assembled in a sandwich form in the absence of double sticky tape to hold the gold nanoparticle sample for prism-type setup testing. In such manner, we are able to focus on the 20 nm AuNPs immersed in water. Gold nanoparticles of a diameter varying from 20 to 40 nm (*BBI*, EM.STP20, EM.STP30, EM.STP40) are employed to characterise the setup. AuNPs are chosen as scatterers due to their strong plasmon resonance at 520 nm, which vastly increases their polarisability and therefore scattering cross section intensities, thereby allowing for more scattered light relative to their size. As shown in Figure 2.4c, scattering images of 40, 30 and 20 nm AuNPs in dark field are recorded by altering the camera exposure time but with illumination light intensity unchanged. Laser power intensity and other camera attributes are determined after focusing on 40 nm AuNPs with 1 ms exposure time to ensure that the intensity counts of particles appear just below the saturation capacity of each pixel. For the prism-type configuration, given that the illumination spot is an ellipsoid with a minor axis length of 10.5 μm, and major axis length of 105 μm, the power density can be calculated as $PD_p = 0.045\ W/3 \cdot 10^{-5}\ cm^2 = 1.5$ kW/cm^2. It is evident that the background becomes brighter relative to the particles with the increase of exposure time. The blue line cut in Figure 2.4d shows the cross section intensity of a 20 nm gold nanoparticle (blue line in Figure 2.4c) imaged by the prism geometry based TIRSM. The primary advantage of prism-type TIRSM is that there is no need to isolate scattered light from the illumination and returning laser beam since the unwanted reflected light is total internally reflected by the prism, thus will not be collected by the objective.

The same characterisation was carried out for through-objective TIRSM using AuNPs with the same sizes as above, however, the laser power is decreased to 0.65 mW, which is about 70 times lower than the power used for the prism-type setting in order to avoid saturating the camera. A uniform image captured with highly fluorescent dye of Rhodamine 6G is used to present the beam profile. Further smoothed by median filter, the illumination spot size is measured by fitting the beam profile to a 2D Gaussian function with a FWHM. Power density is calculated given that the illumination spot is a circle with a radius of 6.5 μm (95 pixels), as $PD_o = 0.65\ mW/(\pi \times 6.5 \cdot 10^{-4})^2\ cm^2 = 0.53$ kW/cm^2.

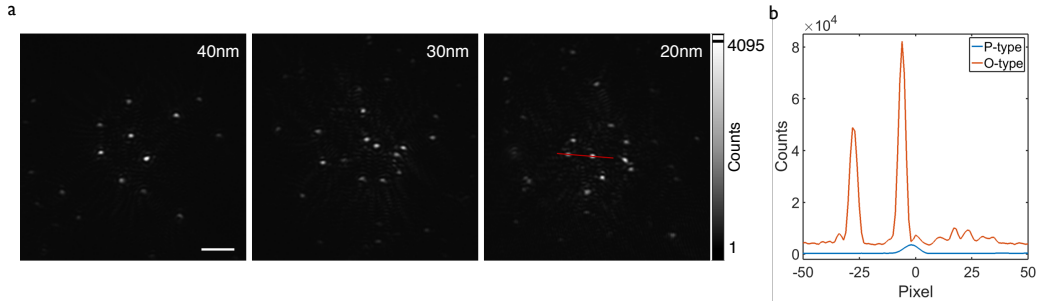


Figure 2.9: Quantitative comparison of Prism-type vs. Objective-type TIRSM set-up. (a) Corresponding scattering images of 40, 30, and 20 nm AuNPs acquired with perforated mirror-based Objective-type TIRSM set-up, recorded with 0.53 kW/cm^2 incident intensity at 0.12 ms, 0.64 ms and 7.3 ms camera exposure time, respectively. Scale bar: 2 μm. (b) Comparison of particle intensity linecuts imaged with different types of TIRSM set-up. Red: Linecut of Objective-type TIRSM in (a). Blue: Linecut of Prism-type in Figure 2.4c.

Figure 2.9a shows scattering images of 40, 30 and 20 nm AuNPs under Objective-type TIRSM. The exposure time is increased proportionately to ensure that the recorded images of different size of AuNPs theoretically have the same mean pixel intensity. In Figure 2.9b, a quantitative comparison of signal intensity of 20 nm AuNPs under Prism-type and Objective-type TIRSM is presented. Considering the difference in laser power intensity and exposure time, the single particle intensity linecut is normalised as:

$$Cut_{norm} = Cut_o \times \frac{PD_p}{PD_o} \times \frac{Exp_p}{Exp_o} \tag{2.17}$$

where $PD_{\mathrm{p/o}}$ is the power density and $Exp_{\mathrm{p/o}}$ is the camera exposure time of Prism-type and Objective-type respectively. It is clearly showing that the Objective-type configuration collects more than 20-fold higher intensity of scattered light than Prism-type with the same power density and exposure time.

The source of difference is the influence of the interface on the scattering properties of a nano-object.[165] Isotropic scattering is expected when the object or any other light source is immersed in a medium, however, when a dipole is placed in the rarer medium very close to the interface, the scattered light does not go everywhere isotopically and instead most of them goes into the higher index material. Consider electric dipoles located at distance z_0 from a dielectric interface and oriented perpendicular to it, when z_0 is smaller than the emission wavelength λ in the rarer medium (n_1), evanescent waves in the dipole's near field give rise to strong radiation and are transmitted into the denser medium (n_2) as plane waves with angles greater than the critical angle α_c,[165] where $\alpha_c = \arcsin(n_1/n_2)$. In which case a refractive index change like that for glass-water directs >90% of the scattered light towards the glass coverslip (Figure 2.10, $n_1 > n_2 > n_3 = 1$).[166] As a result, objective-type TIRSM is deemed to be more efficient at collecting scattered light. On the other hand, this characterisation shows that the perforated mirror assembly is capable of achieving similar or better level of background suppression compared to prism-type TIRSM, which is crucial for detecting smaller scatterers.

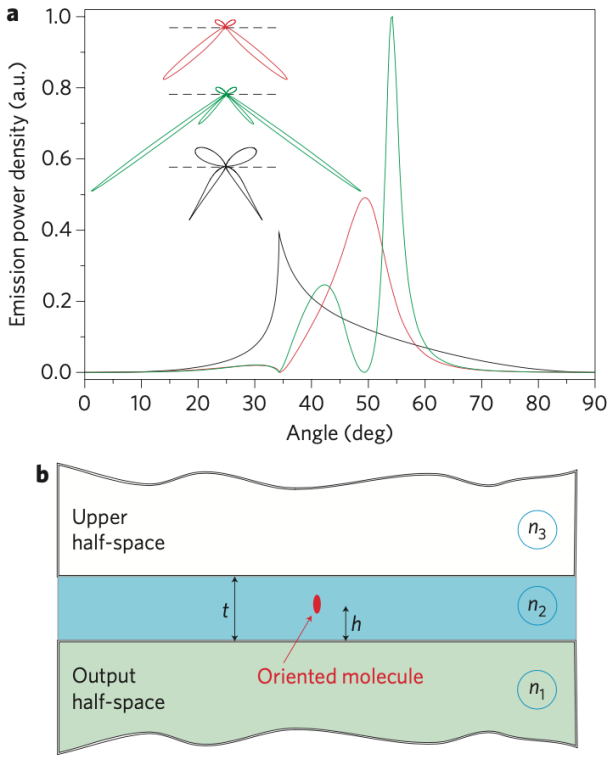


Figure 2.10: Emission properties of a vertically oriented dipole close to a dielectric planar antenna. (a) Emitted power density as a function of the collection angle. Black curve: dipole at a distance of 5 nm from the interface of two media with a refractive index ratio of 1.78 (air–sapphire). Red and green: dipoles in a structure as described in b with middle layer thickness, t= 350 nm and 600 nm, respectively; the emitter was placed at h = 200 nm in both cases. Insets: the same data in polar coordinates. The upper part of each figure is magnified by a factor of ten for better visibility. (b) Sketch of the layered dielectric antenna. Figure adapted from reference 166 with permission.

Perforated mirror vs. two micro-mirrors

In theory, the perforated mirror configuration with optimised hole diameter and distance produces higher localisation precision, since it simultaneously collects as much scattered light as possible from objects, with minimal loss of numerical aperture. However, it is efficient to implement in practice with one major limitation being that the optimised hole size and distance between two holes is determined and changed accordingly by many factors including the back-aperture size associated with objective in use, illumination beam incident

angle and the position where total internal reflection is generated. Once the perforated mirror is fabricated, it is impossible to adjust these predetermined parameters, resulting in limited flexibility during the alignment process. By contrast, two individual micro-mirrors are more flexible while providing similar light collection efficiency. The same signal-to-noise ratio comparison between these two settings is demonstrated in Figure 2.11. After normalisation of power density and exposure time, the setup using micromirror-based coupling of incident and reflected illumination light with optimised mirror diameters and objective mirror separation performs at a higher level of background rejection than the perforated mirror configuration due to the aforementioned drawbacks.

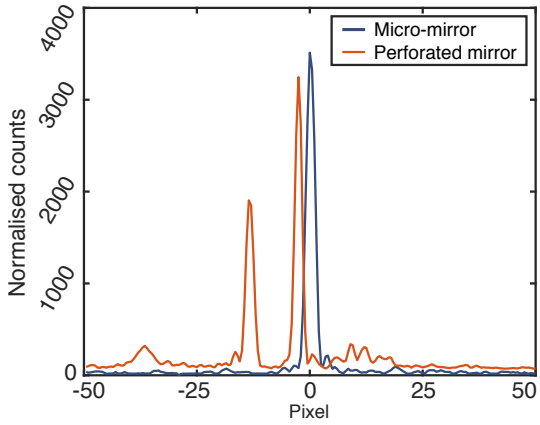


Figure 2.11: Comparison of normalised particle intensity linecuts between perforated mirror and micro-mirror TIRSM set-up.

2.2.2 Characterisation of the final set-up

Due to the diffraction limit, the resolution of an optical microscope is limited to about $\lambda/2$ and any objects smaller than this dimension appear as diffraction-limited spots on the detector, described by a point spread function (PSF). Despite the details within a spot are not being resolvable, the centre of the spot is well defined and thus can be determined with a precision far greater than the resolution of the microscope.

Localisation precision

The precision in localising a nano-object is critically dependent on the SNR which is determined by the number of detected photons and the background noise level. There are two main types of noise. Shot noise arises when photons randomly arrive at the camera chip, while background noise is caused by camera readout noise, dark current, and other factors. In the shot noise limited case, the localisation precision scales as the inverse square root of the number of detected photons ($N^{-1/2}$), whereas for background noise, the localisation precision scales as the inverse of the number of photons (N^{-1}). Therefore, it relatively more important to minimise background since the localisation precision is limited by background noise. Taking these two limits into account, the total localisation error of an experimental setup can be estimated as:

$$\langle(\Delta x)^2\rangle = \frac{s^2 + a^2/12}{N} + \frac{4\sqrt{\pi}s^3b^2}{aN^2} \tag{2.18}$$

where Δx is the localisation error, s is the standard deviation of the PSF, a is the size of the pixel, b is the background noise.

To assess if the setup is performing at or near the shot noise-limit, the experimental localisation error is characterised with sparse 20 nm gold nanoparticles immobilised on the glass surface. Every particle is localised and tracked in order to obtain their positions, which are then plotted as a function of time. To remove the contributions by overall sample drift and vibrations, the distance between each pair of particles is calculated and the localisation precision is determined from the standard deviation of the fluctuations in the distance between two particles divided by a factor of $\sqrt{2}$, since each measurement involves the localisation of two beads. By quantifying the localisation precision at different illumination intensities (or exposure times), the localisation decays as $\sqrt{N}$ and therefore the shot noise-limited behaviour of the setup is evaluated

and used to predict the localisation precision for future measurements (Figure 2.12a).[167]

Size distribution

It is essential to verify and ensure tracking of single particles rather than aggregates, and for this reason, calibration of size dependence is performed based on the principle that the scattering signal scales linearly with square of particle volume, as $S \propto D^6$. To characterise the size distribution, 20, 30 and 40 nm single gold nanoparticles are prepared on a coverslip. In order to obtain the scattering intensity correctly for different particle sizes, it is important to record the images without saturating the camera. In this case, 40 nm gold nanoparticles are first imaged with an initial illumination intensity and exposure time, camera exposure time is then increased 5.6 and 64 times accordingly for visualising 30 and 20 nm gold nanoparticles. Fitted intensities are taken 6^{th} root and plotted as a function of normalised particle size using the average 20 nm signal intensity as the reference. By measuring the scattering intensity of single nanoparticles with different size, the microscope was calibrated and can be used to measure the size of imaged gold nanoparticles, although its spatial resolution remains limited by diffraction.

Vibration analysis

Stability characterisation of the experimental set-up is further carried out in order to verify that external vibrations being coupled into the system do not interfere with measurements. To analyse the vibrations in terms of their frequency and amplitude, sparse 20 nm gold nanoparticles are immobilised on a coverslip surface and a selection of images are acquired at a frame rate of 1000 frames per second. Here it is important to stress that operating with continuous excitation and acquisition is necessary to correctly assess the vibrations over a

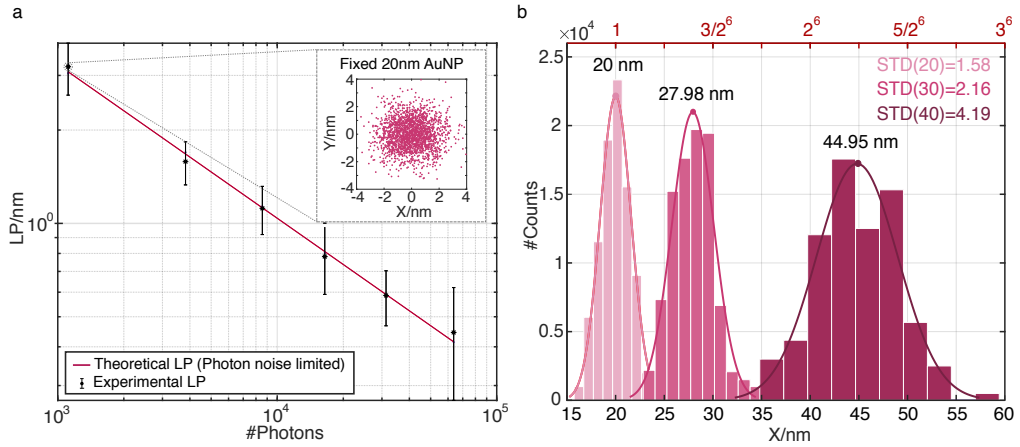


Figure 2.12: Localisation precision and particle size distribution (a) Calibrated experimental localisation precision and theoretical limits dependence on camera exposure time for 2.7 kW/cm^2 incident illumination density. (b) Amplitude of scattering light from spherical particle dependence on particle size.

wide range of frequencies. Tracking and localising all particles in the same FOV, returns a series of their positions through the entire movie (2000 frame in total). A Fast Fourier transform is applied on both x and y trajectories averaged over all particles, to obtain the root mean square (RMS) displacements as a function of frequency.

Vibration amplitudes are plotted in Figure 2.13a as a function of frequency, demonstrating that the localisation error caused by residual vibrations on x, y are on the sub-nm scale. The low frequency vibration is caused by the sample drift from the sample stage, whilst coupling noise from the environment results in the behaviour at higher frequencies. Furthermore, the same analysis is performed to investigate the benefit of applying an enclosure and air-filled tyres insulation method. The results shown in Figure 2.13b,c confirm that protecting the set-up from temperature gradients and air currents by a full enclosure decreases vibrations at mid-range frequencies (10 - 100 Hz), but also, using dual insulation significantly improves the localisation precision at moderate (10 - 100 Hz) and high frequencies (at 250 Hz).

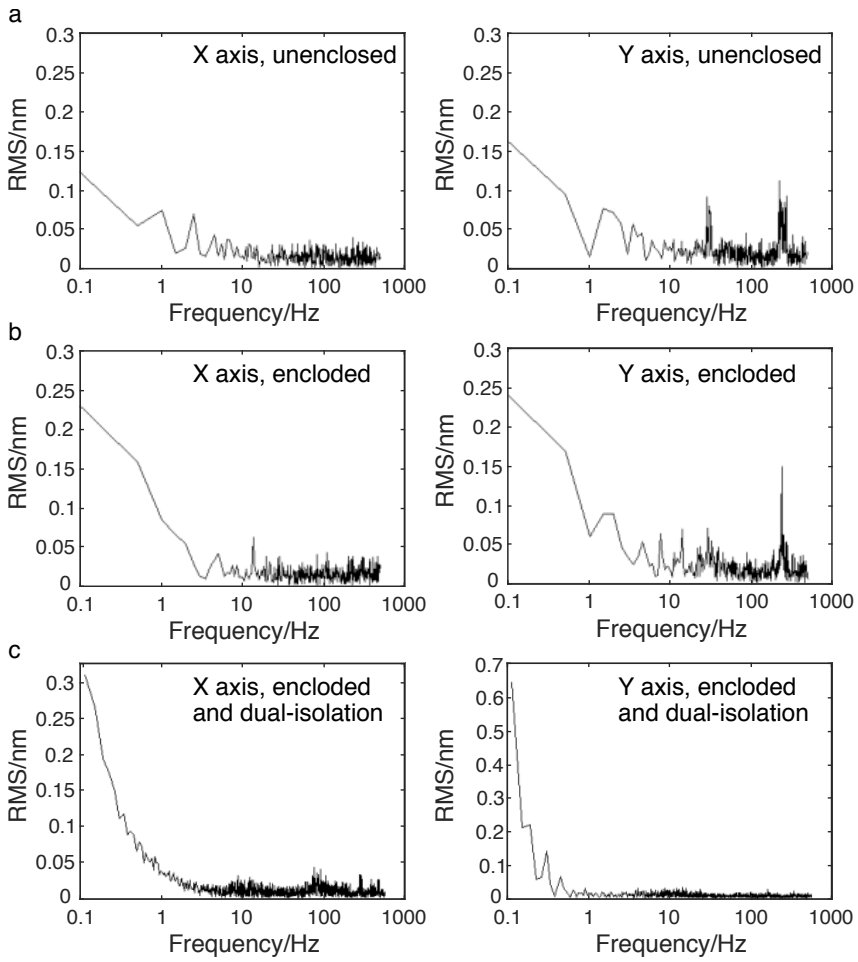


Figure 2.13: Vibration analysis of the experimental set-up (a) Root mean square displacement vs. frequency of microscope set-up open to temperature gradients and air currents. Distinct vibrations on the order of ∼0.1 nm are observed at high frequencies. (b) Root mean square displacement vs. frequency of the microscope set-up with full enclosure. Effective contributions to the decrease of vibrations at mid-range frequencies. (c) Root mean square displacement vs. frequency of the microscope set-up fully enclosed and additionally isolated by air-filled tyres.

2.3 Tethered particle motion assay

Tethered particle motion assay is a simple and power single molecule experiment method for studying mechanical properties and conformations of various biomolecules, e.g., DNA strands as well as interactions with other substances such as proteins. This method involves monitoring the diffusive motion of a reporter bead (tens to hundreds of nanometre) attached to one end of a molecule, while the other end is fixed to the coverslip surface which acts as a tether.

The Brownian motion of a reporter bead induced by thermal fluctuations is restricted by the tether. Incorporated with an optical microscope, the tethered particle is tracked over time with nanometre accuracy which represents the conformational exploration of the free end of the tether. By analysing the particle excursion, the end-to-end distance of the molecule can be extracted which provides useful information about the molecule. TPM is compatible with many microscopy methods such as TIRFM and dark-field microscopy to explore physical properties of molecules in their natural environment. First introduced by Schafer in 1991 to investigate transcription rate of RNA polymerase,[83] this technique gives an alternative to access on a single molecule without posing on external forces. Since then, many efforts have been put into improvements on many fronts such as bead size, tethering methods, imaging techniques and data analysis.[100,102,168,169]

2.3.1 Surface passivation and flow chamber assembly

Surface passivation is a physical/chemical surface treatment technique that is commonly used in many microscopy-based measurements. In TPM experiments, the coverslip surface has to be passivated to prevent non-specific binding of beads and molecular tethers. A selection of blocking agents, e.g. BSA, PEG silane, etc., are available to achieve optimal surface passivation quality depending on the molecule of choice. For all following experiments studied in this thesis, a mixture of mPEG silane (Molecular Weight 2000, *Laysan Bio Inc.*, MPEG-SIL-2000-1g) and biotin-PEG silane (Molecular Weight 3400, *Laysan Bio Inc.*, Biotin-PEG-SIL-3400-500mg) molecules was chosen to passivate the glass surface on the basis of their neutral surface charge, well-developed protocols and small scattering cross sections in terms of introduction of background noise relative to other agents. The mPEG silane acts as a blocking layer and

biotin-PEG molecules with longer length are used to immobilise DNA tethers. All flow chambers used in this thesis were prepared from a thin glass slide and a coverslip bonded by 80 μm thickness double-sided Scotch tapes (3M) to store the sample.

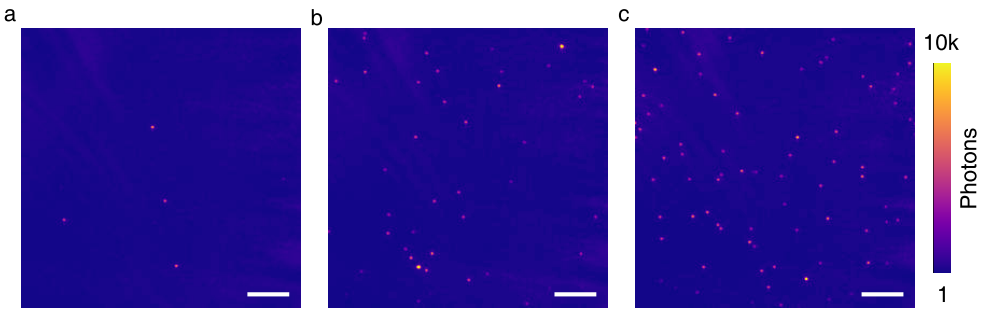


Figure 2.14: The exploration of optimal binding density. (a) Specific binding density with passivation agent of 10 mg/mL mPEG-silane and 1 μg/mL biotin-PEG-silane mixture. (b) Specific binding density with passivation agent of 10 mg/mL mPEG-silane and 10 μg/mL biotin-PEG-silane mixture. (c) Specific binding density with passivation agent of 10 mg/mL mPEG-silane and 50 μg/mL biotin-PEG-silane mixture. Scale bar: 4μm.

The surface passivation protocol is modified based on that from the Dogic lab by Stephen J. DeCamp.[170] The coverslips were sequentially bath-sonicated in 2 % Hellmanex in MilliQ water, isopropanol solution and MilliQ water each for 5 minutes, and subsequently blow dried with nitrogen. Ultrasonic bath cleaned coverslips were oxygen plasma-treated for 8 minutes to activate the surface. This was immediately followed by silane treatment since the surface activation deteriorates rapidly which leads to poor passivation quality. To make the passivation agent of 10 mg/mL mPEG-silane and 50 μg/mL biotin-PEG-silane mixture, I dissolved mPEG and biotin-PEG in 1 % acetic acid ethanol to prepare 20 mg/mL mPEG and 100 μg/mL biotin-PEG solution, respectively, and then mixed them up with 1:1 volumetric ratio. As shown in Figure 2.14, I choose the optimal binding density by exploring various ratio between mPEG and biotin-PEG based on the principle of getting high data throughput without saturating the surface. The plasma cleaned coverslips were stacked one over

other in a sandwich form with a spread of 80 to 100 μL mixture solution in between and stored in petri dishes. After incubation in an oven at 70°C for 45 minutes, the pegylated coverslips were rinsed and nitrogen blow dried again, which were assembled into flow chambers for future measurements.

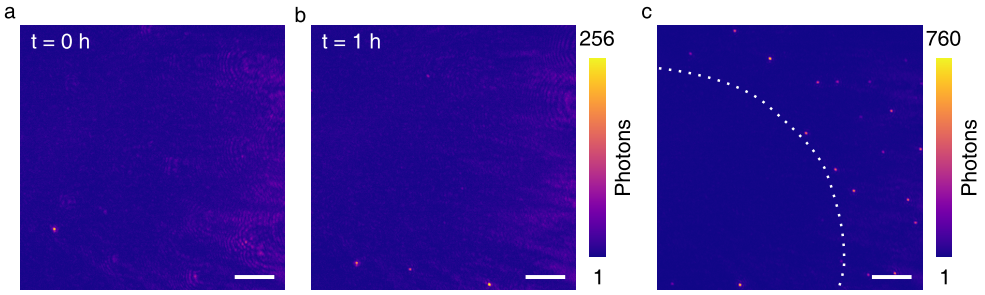


Figure 2.15: Testing the surface passivation quality using streptvidin. A PEG silane coverage of glass coverslip at 10 mg/ml appears to be sufficient for 5 nM nanoparticle concentration No bindings are observed as all specific binding sites were blocked by streptavidin molecules. (a) Image captured right after flowing in gold nanoparticles (at t = 0) and no bindings are observed. (b) No bindings are observed as well at t = 1h. Illumination light was off during the incubation. (c) Rupture of specifically bound tethers on the surface were detected under 20 minutes constant exposure at ∼3 kW/cm^2 illumination power density. White dotted line outlines the laser beam profile. Scale bar: 4μm.

The surface passivation quality was tested using streptavidin (*Sigma-Aldrich Ltd.*, S4762-1MG) and streptavidin-conjugated 20 nm AuNPs. Streptavidin molecules were first added into the flow cell to block all biotin-PEG binding sites on the surface. After washing away excess streptavidin, 20 nm gold nanoparticles functionalised with streptavidin were flowed into the chamber. A PEG silane coverage of glass coverslip at 10 mg/ml appears to be sufficient for 5 nM nanoparticle concentration, as no binding events were observed in 60 minutes (Fig. 2.15a, b). However, despite the high affinity between biotin and streptavidin, rupture of specifically bound tethers on the surface were detected under 20 minutes constant exposure at ∼3 kW/cm^2 illumination power density (Fig. 2.15c).

2.3.2 Tether assembly

The tether assembly is composed of two main phases: immobilisation of dsDNA on glass surface and attachment of gold nanoparticles to the dsDNA, both via a biotin-streptavidin linkage. Double-stranded DNA is synthesised by hybridising two complementary single-stranded oligonucleotides functionalised at their 5'-ends, both with binding of biotin. Previous studies[171,172] show that dsDNA with high GC content are found to be less flexible due to stronger base stacking interactions. In order to minimise any sequence effects, DNA strands used for all experiments in this thesis have a 50 % GC content. For the measurements, a mixture of 150 mM potassium chloride and 10 mM HEPES at pH 7.6 is used as the working buffer (WB), unless specified otherwise.

To immobilise DNA tethers on the glass surface, pre-assembled flow cells with an average volume of 15 μL were first wetted with working buffer (150 mM KCl, 10 mM HEPES, pH 7.6) and incubated with 10 μM streptavidin for 5 minutes to ensure that all biotin-PEG binding sites on the surface were entirely blocked. The streptavidin binds specifically to the biotin-PEG sites on the glass surface, hence avoiding streptavidin-AuNPs binding to the surface directly without dsDNA tethers. The excess streptavidin was then washed away, and an intermediate step was carried out by flowing in streptavidin-AuNPs to assess the streptavidin coverage. For 5 minutes of incubation with 10 μM streptavidin, zero particle bindings were observed. After washing the excess AuNPs, the 5'-end biotinylated-dsDNA (500 nM) in working buffer was injected into the flow cell and incubated for the same amount of time. The biotin on one end of the dsDNA will specifically bind to the streptavidin on the surface and the other end with biotin will be freely diffusing around in solution. Unbound dsDNA molecules were washed out from the cell after incubation. To attach reporter beads to the free end of dsDNA, 20 nm streptavidin-AuNPs (diluted to 4 pM,

BBI) were subsequently injected to the flow cell and incubated for another 5 minutes. The gold nanoparticles were added slightly in excess of bound DNA tethers so as to prevent multiple DNA tethers from binding to a single streptavidin-functionalised gold nanoparticle, thus ensuring that each single DNA tether is bound only to a single gold nanoparticle. After incubation, the flow cell was washed again to remove any unbound streptavidin-functionalised gold nanoparticles. The ready-to-use TPM sample was then kept hydrated for the measurement.

2.3.3 Density control

The density of biotin-PEG silane binding sites on the surface is the critical factor for the yield of qualified tethers. On one hand, when there are too many biotin-PEG molecules on the surface, the probability of a distance between two adjacent biotin-PEG molecules shorter than the DNA contour length increases, thus resulting in a situation that both ends of DNA are immobilised on the surface and attachment of AuNPs will not happen. In addition, DNA tethers very close to each other will lead to binding of multiple DNA tethers to a single gold nanoparticle, even if the gold nanoparticles are in excess of DNA molecules. On the other hand, when the number of biotin-PEG binding site is too low, less tethers will be successfully assembled. As a consequence, the data throughput level is significantly reduced. Thus, in order to balance between TPM sample quality and data acquisition rate, the concentration and ratio of mPEG/biotin-PEG silane mixture used for surface passivation are optimised until the tethered particles population is around 50 to 100 in a 25×25 μm^2 FOV.

2.3.4 Spot detection and tracking

The analysis of the acquired data involves spot detection and particle tracking of each frame in the recorded sequence by fitting a 2D Gaussian to the PSF of the image of a 20 nm gold nanoparticle. The PSF of a 20 nm gold particle is an Airy disc and can be described to a good approximation as a 2D Gaussian:[173,174]

$$PSF \approx A \exp - \left(\frac{(x - x_0)^2}{2{\sigma_x}^2} + \frac{(y - y_0)^2}{2{\sigma_y}^2} \right) \tag{2.19}$$

where the coefficient A is the amplitude of the PSF, x_0 and y_0 are the x and y positions of the PSF respectively. σ_x and σ_y are the x and y standard deviations of the PSF respectively. Therefore, by fitting this function to the images, the intensity counts and the x and y positions of the moving reporter bead for each frame of the recorded movie could be obtained from the fit parameters of A, x_0 and y_0.

Chapter 3

Flexibility of dsDNA at sub-persistence length scales

In this chapter, both the experimental work and the data analysis were carried out by myself. The molecular dynamics simulation using the oxDNA model[175] with different length substrates was performed by Chak Wong and Dr. Jonathan Doye.

3.1 Introduction

The mechanical nature of DNA remains an intriguing question. Despite its double helix structure being discovered more than 60 years ago,[8] neither theory nor experiment has made a unanimous conclusion on DNA flexibility. On large length scales (over thousands of base pairs), DNA is stable enough to be stored into chromosomes.[1,6,32–34,176] Whereas, on short length scales (∼100 base pairs), it has to be flexible enough so that proteins can access it to extract encoded information.[22,23] Understanding the mechanical properties of DNA not only provides insight into its biological function in regulation of many cellular processes, but can also facilitate the application of DNA in the nanosciences, such as DNA origami, used in bioengineering and nanotechnology.[30,31] Specifically, mechanical properties of short length DNA below 100 base pairs play a

fundamental role in many biological processes such as replication, transcription and gene regulation.[58–60]

From the theoretical perspective, because DNA is a biological polymer, ideal chain models including freely-jointed chain (FJC) and worm-like chain (WLC)[177] were developed to describe the flexibility of DNA molecules. In particular, the WLC model has been intensively used to describe the behaviour of semi-flexible polymers such as double-stranded DNA.

Freely-jointed chain model

The freely-jointed chain model is the simplest model to describe all ideal polymers. In FJC, a polymer such as a DNA strand is considered as a chain of N freely-jointed effective bonds (rigid monomers) with a constant bond length b, which is known as the Kuhn length. Each bond of Kuhn length b of the FJC is assumed to be completely rigid. Shown in Figure 3.1a, bond angles between bond vectors $\vec{r_i}$ and $\vec{r_j}$ defined as θ_{ij} are completely independent of each other. The mean-square end-to-end distance can be calculated as:[62]

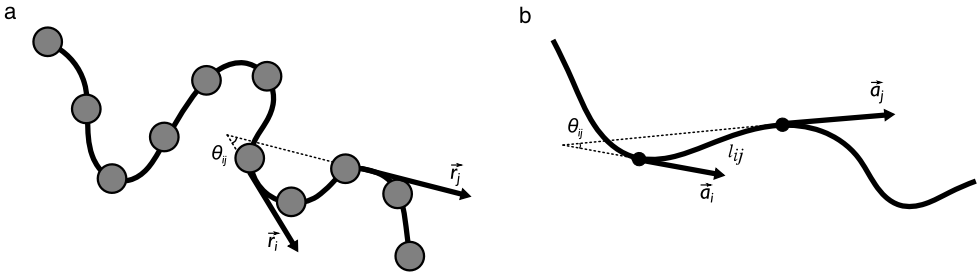


Figure 3.1: Freely-joint model and worm-like chain model. (a) FJC: One conformation of a flexible polymer of n+1 backbone atoms (with $0 \leq i \leq$ n). The bond vectors $\vec{r_i}$, $\vec{r_j}$ direct from atom $i-1$ to i and $j-1$ to j, respectively. θ_{ij} is the angle between bond vectors $\vec{r_i}$ and $\vec{r_j}$. There are no correlations between the directions of different bond vectors, so that $\langle \cos\theta_{ij} \rangle = 0$, for $i \neq j$. (b) WLC: Two tangents $\vec{a_i}$ and $\vec{a_j}$ at distant i and j from the origin along the chain with an end-to-end length l_{ij}. The cosine of the angle θ_{ij} between the two tangent vectors reflects the correlations. For lengths beyond the persistence length, the amount of correlation is 0, and for lengths much less than the persistence length the amount of correlation is 1. For lengths close to the persistence length, the correlation is between 0 and 1.

$$\langle R^2 \rangle = \sum_{i=1}^{n} \sum_{j=1}^{n} \langle \vec{r_i} \cdot \vec{r_j} \rangle = b^2 \sum_{i=1}^{n} \sum_{j=1}^{n} \langle \cos \theta_{ij} \rangle, \tag{3.1}$$

and its contour length L of the chain is:

$$L = N \cdot b. \tag{3.2}$$

Given that there is no interaction between monomers hence there are no correlations between the directions of different bond vectors, $\langle \cos \theta_{ij} \rangle = 0$, for $i \neq j$. Thus, the mean-square end-to-end distance of a FJC is simplified to:

$$\langle R^2 \rangle = Nb^2 = bR_{\max}, \tag{3.3}$$

where $R_{\max}$ is the largest possible end-to-end distance.

Worm-like chain model

The worm-like chain (WLC) model is an advanced model based on the FJC, which is suited for describing semi-flexible polymers, i.e., double-stranded DNA. A commonly used measure to quantify the flexibility of a polymer is characterised by a single microscopic parameter, the persistence length (l_{p}). It is the length at which a vector drawn tangent to the polymer is no longer correlated in space with another tangent vector at a distance. In other words, it reflects how well the orientation of one segment of a polymer is correlated to another segment and defines the regime where the molecule behaves like a flexible elastic rod. For the case of an infinitely long polymer, you would not expect to find any correlation beyond the persistence length while expecting correlations below the persistence length. Thus, for lengths of DNA that are longer than a few hundred base pairs, DNA can be described as a flexible polymer. In contrast, for a DNA molecule shorter than the persistence length, DNA tends to be stiff as implied by the of WLC model.

Two tangent vectors at distance i and j from the origin along the chain can be defined as $\vec{a_i}$ and $\vec{a_j}$ (Figure 3.1b). The correlations in alignment can be measured by the cosine of the angle θ_{ij} between the two tangent vectors with an end-to-end length l_{ij} and written as:[178]

$$\langle \cos\theta \rangle = \exp\left(-l/l_p\right), \tag{3.4}$$

with l_p representing the persistence length that defines the regime where the polymer behaves like a flexible elastic rod. From the mean expectation value of the cosine of the angle we learn that the correlations decay exponentially with separation. When the angle is 90 degrees on average, the cosine is zero, and when it is zero degrees, the cosine is 1. In other word, for lengths beyond the persistence length, the amount of correlation is zero, and for lengths much less than the persistence length the amount of correlation is one. For lengths close to the persistence length, the correlation is between 0 and 1.

WLC model assumes the flexibility of polymers is due to fluctuations of the contour of the chain from a straight line rather than bond rotations between discrete freely hinged segments. Similar to the FJC model, a polymer is described as being comprised of N rigid rod segments, with the bond length (l) which should be negligibly small compared to the contour length of the polymer chain ($L \gg l$). However, the bond angle θ in the WLC is also very small as the bond vector $\vec{r}_{i+1}$ is pointing roughly in the same direction of its neighbouring bond vector $\vec{r}_i$. The overall length L of the chain is:

$$L = N \cdot l \tag{3.5}$$

In contrast to the FJC, WLC segments on length scales shorter than the Kuhn length b are not strictly rigid and can fluctuate and bend. The length of this persistence segment is defined by the persistence length l_p:

$$l_p = l\frac{2}{\theta^2}. \tag{3.6}$$

Since there are correlations between tangent vectors, especially between two successive bonds, hence $\langle \cos\theta_{ij} \rangle \neq 0$ and the mean square end-to-end distance of a WLC can be expressed as:[62]

$$\langle R^2 \rangle = 2l_p R_{\max} - 2{l_p}^2(1 - \exp(-\frac{R_{\max}}{l_p})) \tag{3.7}$$

For a polymer with much longer contour length where $R_{\max} \gg l_p$,

$$\langle R^2 \rangle = 2l_p R_{\max} \tag{3.8}$$

the chain is taking random walks like an ideal chain and $\langle R^2 \rangle = Nb^2 = 2l_p R_{\max} = 2l_p Nb$, resulting in the equivalent expression

$$b = 2l_p, \tag{3.9}$$

the corresponding Kuhn length therefore is twice the persistence length.

$$\langle R^2 \rangle \cong {R_{\max}}^2 - \frac{{R_{\max}}^3}{3l_p} + \ldots \tag{3.10}$$

while, for a chain which is much shorter than its persistence length ($R_{\max} \ll l_p$), the polymer is then showing a rigid rod-like behaviour. Nevertheless, there has been substantial debates in literature regards the flexibility of DNA on sub-persistence length scales.

From the experimental perspective, measurements at different DNA length scales using various techniques yielded contradictory results. For example, the persistence length of dsDNA measured by single-molecule manipulation techniques such optical tweezers and magnetic tweezers is about 50 nm (150 bp), which is the widely accepted value in the field of DNA mechanics.[76,78]

However, Cloutier et al. recently have demonstrated the spontaneous sharp bending of short DNA (94 bp) using a DNA cyclisation assay.[71] Their results yielded a 10^2-10^4 times higher rate of cyclisability (j factor) than the prediction by the WLC model. Similar extreme bendability of DNA on short length scales (<120 bp) was observed by smFRET[72] and AFM[80] measurements which have challenged the idea that DNA shorter than persistence length acts like a rigid rod. Nevertheless, all these measurements have their own intrinsic limitations. Because of physical connections to a micron sized bead, optical tweezers and magnetic tweezers are insensitive to local bending which may remarkably increase DNA flexibility on short length scales.[179] The result of DNA cyclisation experiments has been challenged and attributed to very high ligase concentration.[180] For the smFRET experiment, information of DNA flexibility was only derived from overall population without access to the dynamics of individual molecules. Furthermore, the coupling effect of a rigid supporting surface reduces the accuracy of AFM measurements.

In this chapter, I addressed DNA flexibility at short length scales ($\leq$160 bp) obtained from direct measurements using the TPM method, which has been experimentally unachievable. Interactions between the tethered particle and the surface give rise to the volume exclusion effect,[104] which impeded direct investigations on short length DNA molecules below 100 nm. Although Brinker et al.[100] have made a great effort to experimentally investigate the shortest dsDNA molecules (123 nm) ever achievable using the single molecule technique which is similar to the one discussed in this chapter, their results are inaccurate due to the low tracking accuracy of tethered reporter beads and in turn less accurate measured l_p. In particular, the mean value of 34.8 nm of 45 candidates with a large error of σ = 18.6 nm is meaningless. Their localization precision is about 30 nm even at long exposure time of 10 ms which leads to 10%

underestimation of particle displacement due to the motion blur effect. In contrast, I set the camera exposure time to 6us and provide a 2 nm localization accuracy. According to my calculation in *Chapter 2*, the relaxation time of the particle is $\tau = 72.1 \pm 9.2$ μs suggesting that all the measurements are entirely free from motion blur effect. Also, they use 80 nm diameter gold nanoparticles as reporter beads result in a large excursion number (0.84 for 123 nm DNA) at a regime where the volume exclusion effect starts to at play adding additional errors on determination of native flexibility of DNA. But still, the approach how they determine the measured persistence length from simulations is helpful. By carrying out Monte Carlo simulations with a selection of persistence length from 10 nm to 90 nm and statistically comparing the experiment results to simulations, they determine the measured persistence length from which the distribution has the highest statistical agreement. Here, they change the persistence length used in simulations as a control factor. This idea provides me an alternative way to estimate the persistence length of dsDNA at sub-persistence length scales in the absence of a simple analytical formula to determine the distribution for the position distribution of tethered particles. Within all measurements in this chapter, TIRSM setup enables tracking of gold nanoparticles down to 20 nm diameter with simultaneous nanometre precision and temporal resolution on the order of microseconds, thereby allowing for investigation of much shorter DNA lengths at regimes where volume exclusion remains negligible.

Furthermore, I tested the possibility of my TPM assay for identifying DNA binding protein mediated conformational changes. By monitoring changes to the tethered particle motion, the protein-mediated deformation of DNA, which generally exceeded the conformational configurations induced by thermal fluctuations, could be distinguished. Protein RAD52 has been shown by many studies

to play a critical role in homologous recombination and double-strand break repair in eukaryotic cells. It is a gene product encoded by the RAD52 genes which have been identified in both mammalian cells of humans[181] and in yeast Saccharomyces cerevisiae.[182] Although the human RAD52 (hRAD52) protein shares similar structure and function with Saccharomyces cerevisiae RAD52 protein (ScRAD52), the role of RAD52 protein varies in homologous recombinational repair with regard to facilitating the loading of RAD51 on replication protein A (RPA)-coated single-stranded DNA (ssDNA) of humans[183,184] and yeast.[185–187] In Saccharomyces cerevisiae, ScRAD52 seems to be crucial for recombinational repair of double strand breaks (DSBs) via RAD51,[185,188–191] promoting the RAD51-dependent annealing of complementary ssDNA. In contrast, the corresponding role of hRAD52 in humans has been taken over by breast cancer susceptibility protein 2 (BRCA2),[192] however, hRAD52 plays an important role in the Rad51-independent recombination pathway.[193,194] RAD52 is a protein that reportedly both binds to ssDNA[183–185] and dsDNA.[186,191,195–198] The hRAD52 is a 418-amino acid protein that forms a heptameric ring with a large central channel as characterised by electron microscopy.[185,199] As presented in Figure 3.2, Kagawa et al. used a mutational analysis revealed that Arg-55 and Lys-152 are necessarily for ssDNA binding, whereas Tyr-65, Arg-153, and Arg-156 are essential for binding both ssDNA and dsDNA.[200] Singleton et al. proposed that ssDNA wraps around the outer surface of the RAD52 ring rather passes through the channel of the ring,[201] interacting with an exposed positively charged groove. While such DNA wrapping or protein-protein bridging is not observed in RAD52 bound to dsDNA,[202] their results predict that RAD52 binds to dsDNA through destabilising and intercalating into the double helix, resulting in a substantial decrease in persistence length and slight increase in contour length. And most importantly, the interaction of RAD52 with dsDNA

is not DNA sequence dependent.[202]

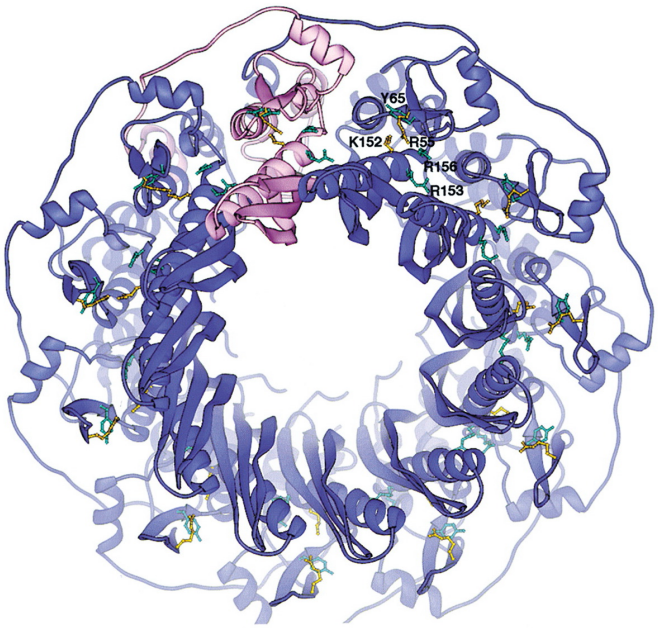


Figure 3.2: A monomer of RAD52. Residues that affected the ssDNA binding and the dsDNA binding most severely are colored in gold and sky blue, respectively, and are mapped on the $RAD52_{1-212}$ ring. Figure adapted from reference 200 with permission.

3.2 Experimental method

3.2.1 Materials

Both mPEG-silane (MPEG-SIL-2000-1g) and biotin-PEG-silane (Biotin-PEG-SIL-3400-500mg) were purchased from Laysan Bio, Inc. (Arab, AL, U.S.) and stored under nitrogen against humidity at -20°C. Prior to completion of plasma cleaning, PEG silane aliquots were dissolved in 1% acetic acid in ethanol. Single-stranded oligonucleotides of 60, 90 and 120 bases with biotin at the 5'-ends were purchased from Sigma-Aldrich Ltd. (Milwaukee, WI, U.S.). The 160 bases single-stranded DNA oligos were purchased from the ATDBio Ltd. (Southampton, U.K.). All single-stranded oligonucleotides are reconstituted with HEPES buffer to make dsDNA solutions containing

10 mM HEPES (pH 7.6) and 150 mM KCl. Streptavidin (S4762-1MG) was purchased from Sigma-Aldrich Ltd. (Milwaukee, WI, U.S.) and reconstituted with water to make a final concentration of 10 μM containing 10 mM HEPES (pH 7.6) and 150 mM KCl. It is important to use salt-free streptavidin to avoid streptavidin aggregation in the PBS buffer, which generates imaging background and deteriorates the SNR of the acquired images. Streptavidin conjugated gold nanoparticles were purchased from British Biocell International (Cardiff, U.K.) are diluted 500× to a final concentration of 5 nM.

3.2.2 Double stranded DNA and TPM sample preparation

Double-stranded DNA preparation

The double stranded DNA constructs of different lengths of 60, 90, 120 and 160 bp are prepared by annealing the two complementary single DNA strands, respectively. The dried single stranded oligonucleotides functionalised at their 5'-ends with biotin are reconstituted accordingly in 10 mM HEPES buffer and mixed. The mixtures are heated quickly up to 90°C followed by a cooling rate of 1°C/min down to 25°C in a polymerase chain reaction (PCR) machine, resulting in a 5 μM dsDNA solution. The sequence of the single-stranded oligonucleotides with 50% GC content are listed below:

60 bp

5′biotin- *GGC GTC GTC TGA GCA GTC TGA TCG TGT CTG AGT ACG CAT GAT CTG GAT GTG TGA TGT AGC* -3′

5′biotin- *GCT ACA TCA CAC ATC CAG ATC ATG CGT ACT CAG ACA CGA TCA GAC TGC TCA GAC GAC GCC* -3′

90 bp

5′biotin- *ACT GAT TCT ATA TGG ATA CCT AGA GTT GCC TAT ACC TCG ACC AGA CCA AGG GTG AGT GGT TGC AGT GTG ATC*

CTA GAG GGG CCA GAG GAG -3′

5′biotin- *CTC CTC TGG CCC CTC TAG GAT CAC ACT GCA ACC ACT CAC CCT TGG TCT GGT CGA GGT ATA GGC AAC TCT AGG TAT CCA TAT AGA ATC AGT* -3′

120 bp

5′biotin- *ACT GAT TCT ATA TGG ATA CCT AGA GTT GCC TAT ACC TCG ACC AGA CCA AGG GTG AGT GGT TGC AGT GTG ATC CTA GAG GGG CCA GAG GAG ATC GTA CAT TAT TGG GTG CCT TCC TGG GTA* -3′

5′biotin- *TAC CCA GGA AGG CAC CCA ATA ATG TAC GAT CTC CTC TGG CCC CTC TAG GAT CAC ACT GCA ACC ACT CAC CCT TGG TCT GGT CGA GGT ATA GGC AAC TCT AGG TAT CCA TAT AGA ATC AGT* -3′

160 bp

5′biotin- *CTG GAT GTG TGA TGT AGC GCA CTG ATT CTA TAT GGA TAC CTA GAG TTG CCT ATA CCT CGA CCA GAC CAA GGG TGA GTG GTT GCA GTG TGA TCC TAG AGG GGC CAG AGG AGA TCG TAC ATT ATT GGG TGC CTT CCT GGG TAA GTG AGA TAC CTG TGA GAA C* -3′

5′biotin- *GTT CTC ACA GGT ATC TCA CTT ACC CAG GAA GGC ACC CAA TAA TGT ACG ATC TCC TCT GGC CCC TCT AGG ATC ACA CTG CAA CCA CTC ACC CTT GGT CTG GTC GAG GTA TAG GCA ACT CTA GGT ATC CAT ATA GAA TCA GTG CGC TAC ATC ACA CAT CCA G* -3′

TPM samples preparation

Cleaned No. 1.5 borosilicate coverslips (Menzel-Glaser, Braunschweig, Germany) are used for preparation of TPM samples by following the same procedure as

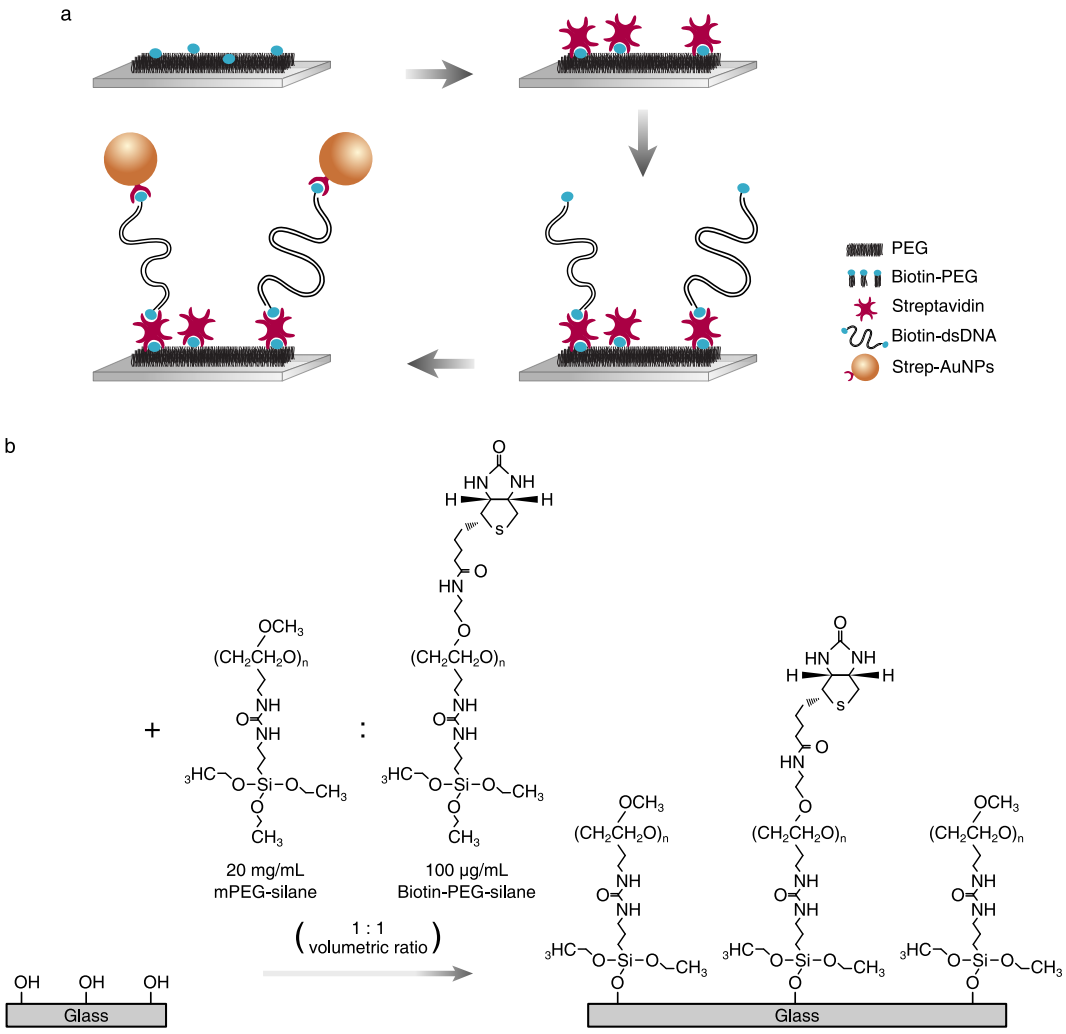


Figure 3.3: Double-stranded DNA tether assembly. (a)The cleaned microscope coverslip is passivated with a layer of mixed mPEG and biotin-PEG molecules to ensure that each DNA tether specifically binds to the surface. After that, excess streptavidin molecules are injected into the flow chamber to occupy all biotin-PEG binding sites on the surface. After washing the flow chamber with working buffer, biotinylated dsDNA tethers and streptavidin functionalised gold nanoparticles are subsequently added into the flow chamber to finish the assembly of TPM constructs. (b) Chemistry of the linkage from the surface to the DNA, including the mPEG-silane and Biotin-PEG-silane mixture.

described in *Chapter 2*. The dsDNA immobilisation on glass surface and the attachment of gold nanoparticles to molecules are achieved by taking advantage of high molecular affinity between biotin and streptavidin. The flexibility of the biotin-streptavidin linkage is negligible due to the strong protein interactions for which a 200 pN rupture force is needed to break the streptavidin-biotin

complexes.[203] Concentrations of mPEG/biotin-PEG mixture, dsDNA molecules and gold nanoparticles are varied until an optimal yield of single nanoparticle tethered dsDNA is observed. Figure 3.3b presents the chemistry of the linkage from the surface to the DNA using the method discussed in chapter 2.

3.2.3 RAD52 preparation

Aliquots of the DNA binding protein RAD52 are prepared and provided by the Schaffer group (Tübingen, DE) in 10 mM Tris (pH 7) and 50 mM NaCl buffer. Buffer exchange was carried out using desalting columns purchased from Bio-Rad Laboratories, Inc. (Berkeley, CA). The packing buffer in the column was first removed by 2 minutes of centrifugation at 1000× g and washed with 500 μL working buffer. Four washes result in >99.9% of buffer exchanged. The RAD52 sample (20 μL) was then applied to the column and centrifuged for 4 minutes at 1000× g. The buffer exchanged RAD52 is now in 10 mM HEPES (pH 7.6) and 150 mM KCl buffer. The protein concentration after centrifugation was determined by measuring the absorbance in working buffer. RAD52 samples were kept at 4°C and diluted to a final concentration of 5 μM before use.

3.2.4 Stroboscopic dark-field microscope

Imaging and tracking of dsDNA tethered particles is implemented with the custom-built micro-mirror based TIRSM setup. Considering the fast motion of bead, blurring happens if one takes snapshots which are too long/integrates over time. To avoid this, high temporal resolution is required. TIRSM is therefore operated in a stroboscopic fashion to determine the actual bead position rather than capturing a blurred image. In the meantime, for shot noise-limited detection, the SNR scales as $\sqrt{N}$, while keeping a short exposure time, a high level of SNR can be obtained with increasing incident power. Thus,

to enable high-speed tracking of 20 nm gold nanoparticles with nanometre localisation accuracy and meanwhile ensuring minimal thermal damage on samples, pulsed illumination is more preferable than a continuous wave laser beam. For these reasons, we opted for a pulsed laser with a 5% duty ratio enabled by a 1 kHz pulse waveform with its amplitude controlled by a function generator. Within the pulse duration, which is 50 μs, the power density of the illumination beam is about 91 kW/cm^2, while the integrated power density over the entire cycle is 4.5 kW/cm^2. In each movie, a sequence of 3800 images are captured with a frame rate at 200 Hz.

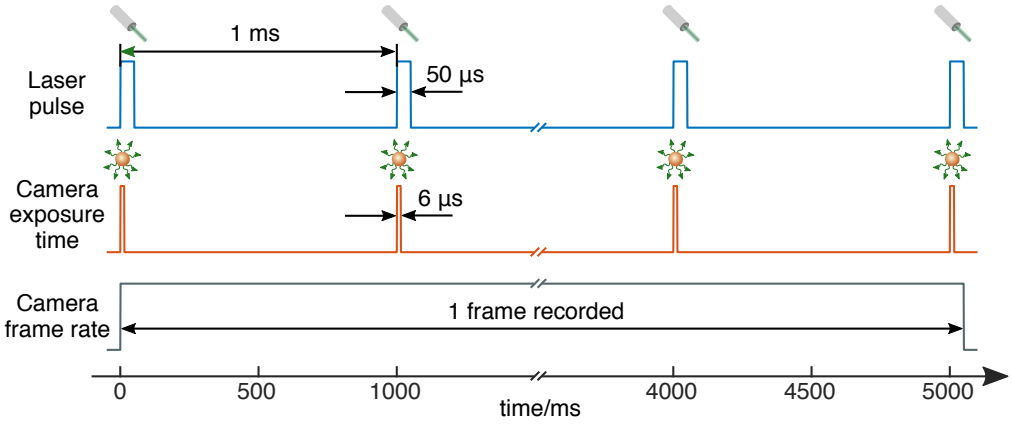


Figure 3.4: Concept of pulsed laser illumination. The illumination laser and camera are both synchronously triggered by a 1 kHz pulsed signal with 5% duty ratio. The camera exposure time is set to 6μs to ensure that the captured image of reporter bead is not blurred. In every 5 ms, one image is recorded according to the camera frame rate of 200 frames per second.

3.2.5 Instrument setup parameters

In all pure scattering channels of the TIRSM, a 520 nm wavelength laser is used as illumination light for tracking of gold nanoparticles and an independent focus control channel is achieved with an 830 nm infrared laser. The use of a high numerical aperture (1.42NA) Olympus PLAPON 60× infinity-corrected oil-immersion objective in combination with a 200 mm focal length imaging lens yields a 66.67× magnification, which results in an ultimate pixel size of

51.7 nm for the camera sensor with an effective pixel size of 3.45 μm. Detection camera is operated in triggering mode which is synchronously triggered by the same pulse for illumination. Camera exposure time is fixed to its lowest bound, which is 6 μs, while the integrated power density is altered between 4.5 kW/cm^2 and 0.5 kW/cm^2 for 20 and 40 nm particles.

3.2.6 Data acquisition and analysis

Raw data acquisition and spot detection are streamlined using custom-written software in LabVIEW. Limited by the deterministic time-scale of the computer which is typically on the order of milliseconds, time lag and frame skipping is evident when running at high speed and continuous data acquisition which can lead to loss of both information and synchronisation between the camera and the computer. In order to solve this problem, a sequence of images was first streamed into a 2 GB space pre-allocated in the random-access memory (RAM) before being transferred and saved to the hard drive. As a limitation, the number of captured images in each individual movie is up to 3800 frames with a 512 × 512 pixels FOV, as the file size is limited by the pre-allocated memory.

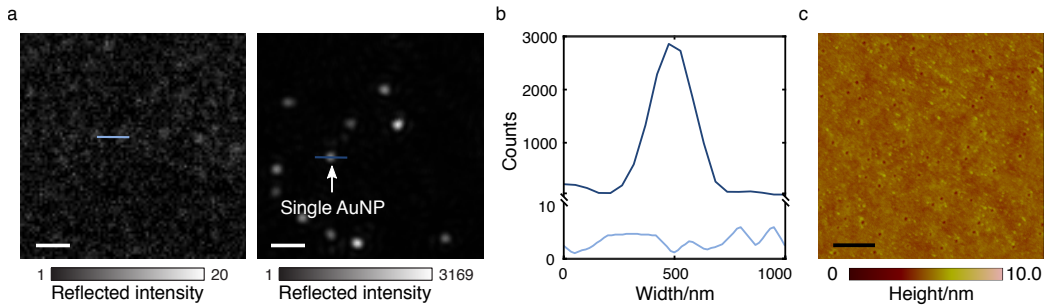


Figure 3.5: High signal-to-noise ratio dark-field image of 20 nm AuNPs. (a) Raw dark-field image of microscope coverslip surface roughness and raw dark-field image of single 20 nm gold nanoparticles on microscope coverslip surface with high SNR. Scale bar: 2 μm. (b) Intensity comparison of linecuts in (a). (c) Image of microscope coverslip surface roughness via AFM measurement. Scale bar: 200 nm.

Tethered particle candidate detection and localisation

Taking advantage of high SNR and strong scattering signal from 20 nm AuNPs against dark background, tethered particle candidates can be easily spotted by applying an intensity threshold above the background noise. Finding the pixel with maximum average intensity amplitude from the first 50 frames of the PSF, first returns the corresponding pixel coordinates in the FOV. Despite the fact that the optical response of a gold nanoparticle is a PSF with a FWHM on the order of ∼200 nm for visible light, by fitting the PSF to a 2D Gaussian function, various parameters of the particle including centre of mass of the PSF, standard deviation of the Gaussian and amplitude of the PSF can be obtained. To reduce the computational load, a small window of 16 × 16 pixel is applied and centred on the highest intensity pixel so that the time consumed for fitting can be significantly reduced.

Two-dimensional particle distribution

In the images of 20 nm AuNPs, the PSF can be modelled and approximated as a 2D Gaussian function.[173] From the fit parameters by Equation 2.19, the centre of mass position of a tethered particle in a sequence of images turns into a plot of particle displacements in $x - y$ plane. The mean-square displacement of a random walk from the origin is equal to the mean-square end-to-end vector of a freely jointed chain with the number of monomers N equal to the number of steps of the walk and the monomer length b equal to the step size $\langle \vec{R}^2 \rangle = Nb^2$. The mean-square displacement is composed of three mean-square displacements of the three independent one-dimensional walks:

$$\langle \vec{R}^2 \rangle = \langle R_x^2 \rangle + \langle R_y^2 \rangle + \langle R_z^2 \rangle = Nb^2 \tag{3.11}$$

Since each of the three Cartesian axes are equivalent, the mean-square displacement along each of them must be one-third of the total:

$$\langle R_x^2 \rangle = \langle R_y^2 \rangle = \langle R_z^2 \rangle = \frac{Nb^2}{3}. \tag{3.12}$$

In the textbook,[62] the one-dimensional probability distribution function for the components of a random walk along one axis (x axis for example) in terms of mean-square displacement can be written as:

$$P_{1d}(N, R_x) = \frac{1}{\sqrt{2\pi\langle R_x^2 \rangle}} \exp\left(-\frac{R_x^2}{2\langle R_x^2 \rangle}\right) \tag{3.13}$$

by substituting mean-square displacements $\langle R_x^2 \rangle = \frac{Nb^2}{3}$ into above equation, we get

$$P_{1d}(N, R_x) = \sqrt{\frac{3}{2\pi N b^2}} \exp\left(-\frac{3R_x^2}{2Nb^2}\right) \tag{3.14}$$

and two-dimensional:

$$P_{2d}(N, R_{x,y}) = \frac{3}{2\pi N b^2} \exp\left(-\frac{3(R_x^2 + R_y^2)}{2Nb^2}\right) \tag{3.15}$$

this probability distribution can be rewritten in the polar coordinate system:

$$P_{2d}(N, r)2\pi r dr = \frac{3}{2\pi N b^2} \exp\left(-\frac{3r^2}{2Nb^2}\right)2\pi r dr \tag{3.16}$$

where $r = \sqrt{R_x^2 + R_y^2}$ and Nb is equal to its contour length L, thus I obtain the equation:

$$P_{2d}(N, r)2\pi r dr = \frac{3}{2\pi b L} \exp\left(-\frac{3r^2}{2bL}\right)2\pi r dr \tag{3.17}$$

and in the polar coordinate system:

$$P_{2d}(N, R) = \frac{r}{\langle R^2 \rangle} \exp\left(-\frac{r^2}{2\langle R^2 \rangle}\right) \tag{3.18}$$

By comparing the fitted parameters from experimental data, the persistence length of the DNA molecule could be determined.

Selection criteria

Qualified particles defined as single DNA molecule tethered freely mobile particles are automatically identified based on their symmetric two-dimensional particle distribution of a maximum amplitude similar to the length of the DNA when fully stretched. The entire process is implemented with a computational sorting script written in MATLAB. Even though the optimised surface passivation quality and excessive streptavidin-AuNPs to DNA molecules incubation ratio were achieved to improve the yield of qualified TPM samples, potential presence of immobile particles and the attachment of multiple DNA tethers to a single gold nanoparticle is inevitable. As a result, particle distributions extracted from bead motion of poor candidate particles lead to an inaccurate estimate of DNA flexibility. However, the qualified particles and the DNA tethers as assumed are both free to explore any configuration therefore exhibiting a radially symmetric and fully expanded 2D projection, different from ones with restricted amplitude and asymmetrical profile derived from particles stuck on the surface and multiply tethered particles, respectively. Exclusion of immobilised particles whose distributions span significantly less than the dsDNA contour length and multi-tethered particle that exhibit elongated distributions is a powerful screening tool. However, only two selection criteria fail to exclude some particles which have an overall symmetric scatter plot of positions but are transiently stuck onto the surface during data acquisition. In addition, further symmetry assessment of the scatter plots is carried out by comparing the number of points and radial distribution function of eight equally divided sectors. Overall, the selection criteria for identifying a qualified tether are as follows:

1. The two-dimensional particle distribution has a radially symmetric shape whose ellipticity < 1.1

2. The two-dimensional particle distribution has a maximum amplitude close to the contour length of the DNA molecule ($0.8L < r < 1.2L$)

3. The standard deviation of number of points in each sector $\mathrm{STD}_{\mathrm{npts}} < 100$ and the standard deviation of the RDF in each sector $\mathrm{STD}_{\mathrm{rdf}} < 0.002$

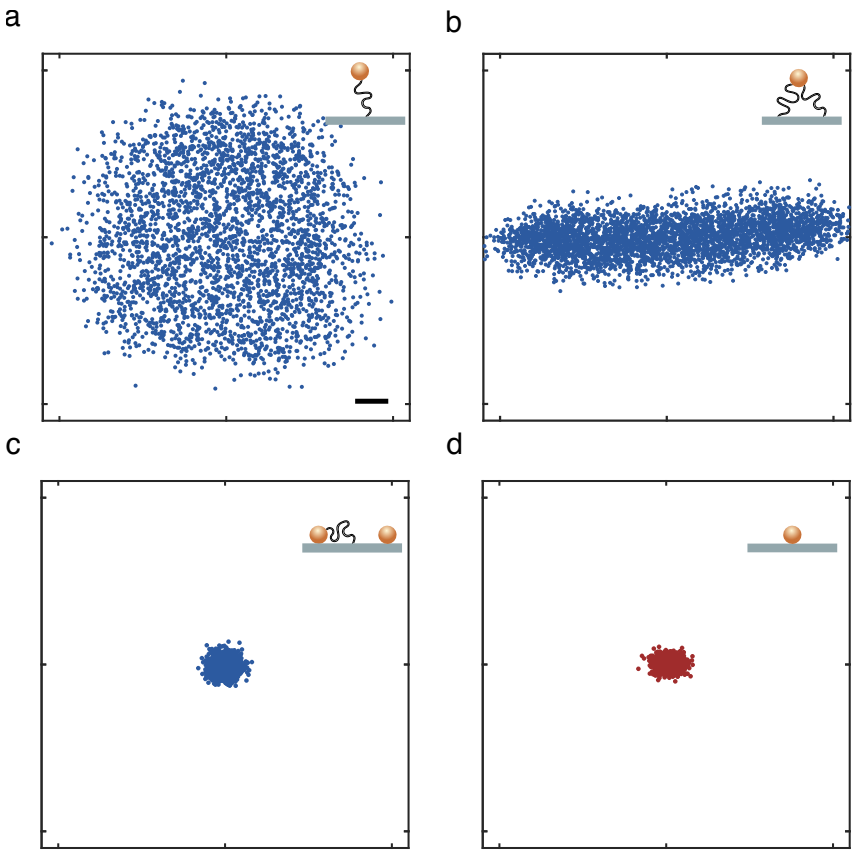


Figure 3.6: Various tethered particle behaviours. (a) Radially symmetric scatter plots of a freely mobile single-tethered particle. (b) Scatter plots of a partially mobile multi-tethered particle. The restricted motion of multiply tethered particle in solution results in an elongated distribution to a degree which depends on the distance between the anchor points of the DNA tethers on the surface. (c) Scatter plots of a stuck particle with limited particle displacement whether it has been tethered to a DNA molecule or not. All examples are obtained using 120 bp dsDNA with 20 nm reporter bead. (d) An indicating stable scatter plots of particle displacement obtained from a 20 nm gold nanoparticle directly immobilised on the surface without DNA tether. Scale bar: 10 nm.

3.3 Experimental results

3.3.1 Observed Brownian motion: high degree of symmetry

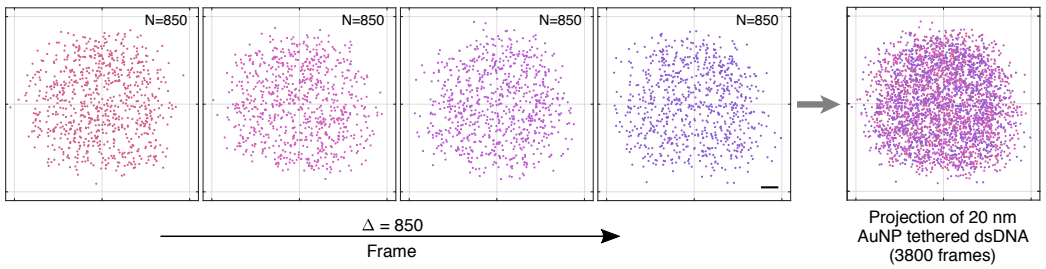


Figure 3.7: Observed Brownian motion of single molecule tethered particle. Scatter plots of localisations from individual 120 bp dsDNA molecules tethered with a 20 nm gold nanoparticle. The diffusion of a freely mobile particle restricted by a single dsDNA tether in solution is Brownian motion induced by thermal fluctuations. Its two-dimensional displacement has a high degree of symmetry. Scale bar: 10 nm.

Tracking and localising all particles in the same FOV, after exclusion of immobilised particles and partially mobile multi-tethered particles, returns positions of their centre of mass in each frame so that two-dimensional particle distribution plots with a high degree of symmetry from qualified particles can be obtained. Figure 3.7 shows an example of the radially symmetric scatter plot of a mobile single 20 nm gold nanoparticle tethered with a 120 bp dsDNA. The ellipticity is 1.06 defined as the ratio between x and y axis of the in-plane position distribution. Since both the DNA tether and the particle are free to undergo Brownian motion driven by thermal fluctuations, the particle displacement is independent of time and completely random. The diffusion of the particle restricted by the DNA molecule leads to a maximum displacement amplitude value of about 50 nm which corresponds well to the contour length of 120 bp dsDNA (40 nm) combined with the radius of tethered gold nanoparticles (10 nm) and the length of two biotin-streptavidin linkage (∼3 nm in total). Figure 3.6b presents the skewed distribution of multiple DNA tethers attached

to one gold nanoparticle; the degree of elongation depends on the distance between two anchor points of DNA tethers. In addition, Figure 3.6c depicts the two-dimensional particle distribution of a stuck particle. To verify that the source of limited particle displacement is mainly due to the localisation error and the flexibility of biotin-streptavidin linkers and PEG molecules, a control experiment was carried out by immobilising streptavidin conjugated 20 nm AuNPs directly on the mPEG/biotin-PEG layer in the absence of DNA. After performing the same analysis procedure, an indicating stable scatter plot of particle displacement is obtained (Figure 3.6d).

3.3.2 RDF: Particle-to-particle variability

TPM measurements provide the positional data of the reporter bead (and hence the polymer) over time, as described by the ideal chain models, and the flexibility of DNA can be extracted from the fit of the radial probability density function. To extract the persistence length of DNA from diffusive motion of the tethered particle, the radial distribution function is plotted from the histogram of its end-to-end distance in the two-dimensional particle distribution. Figure 3.8a shows individual plots and their averaged value of the observed RDF of 9 qualified movers acquired from two different measurements under identical conditions. As expected, after computational exclusion of malformed tethers, the RDFs (normalised to area) are Rayleigh distribution-like and the fit by the corresponding Equation 3.17 allows determination of the persistence length since the contour length of the tethered DNA molecule is known. The microscope setup and experimental assay are hereby confirmed to be reliable from the very small particle-to-particle variability, which also indicates that all qualified tethers are behaving similarly at thermal equilibrium. The histogram of radial distribution averaged over 1162 qualified tethers is presented in Figure

3.8b and the red line is the Rayleigh distribution fit of the radial distribution. Measuring persistence length from averaged RDF of multiples DNA molecules with small variability yields an accurate estimate of DNA flexibility with statistical significance.

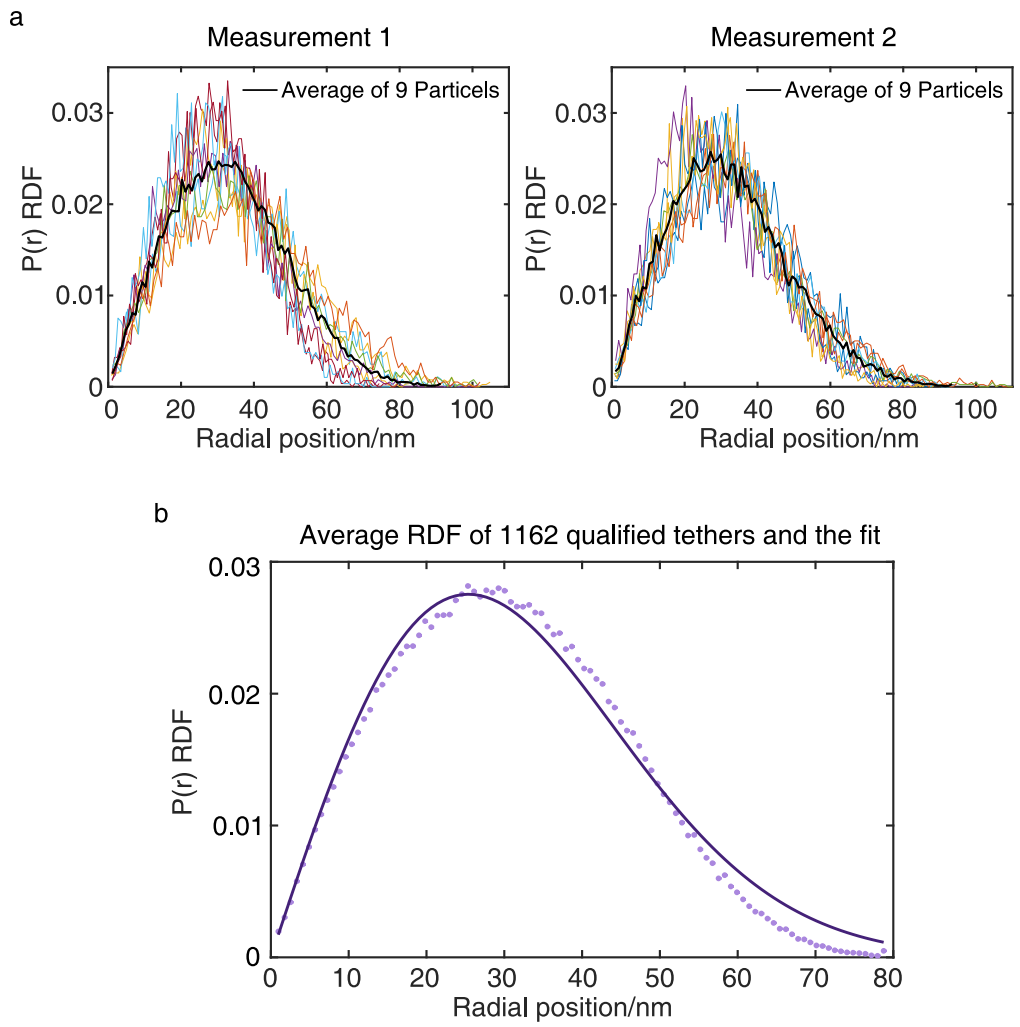


Figure 3.8: Radial distribution function (a) Observed particles' radial distribution functions acquired from two experiments with the same conditions and plotted with 9 tethered particles from each experiment. Black line is the averaged RDF over 9 particles. The small particle-to-particle variability indicates that all qualified tethers are behaving similarly at thermal equilibrium. Experiment data obtained using 120 bp dsDNA. (b) The histogram of radial distribution function averaged over 1162 qualified tethers.

Same TPM experiments are repeated with 60, 90 and 160 bp dsDNA molecules to determine the corresponding persistence length from their observed

RDFs. Parallel imaging and acquiring multiple tethers with nanometre spatial and 6μs temporal resolution in a short period of time not only provides a considerable amount of statistics from a large number of representative tethers, but also minimises the errors from mechanical drift; therefore, post-processing such as drift correction and detector time-averaging effects is not necessary in this approach.

3.3.3 Dependence of tethered particle distribution on DNA contour length

In TPM experiments, the tethered gold particle is enduring Brownian motion under confinement of the DNA molecule, the maximum amplitude of particle excursion is therefore limited by the effective length of the tether, in which case is the contour length of DNA molecules in the absence of DNA bending and looping. Although, the diffusion of tethered particle is restricted to a half-space due to the confinement imposed by the coverslip for a real TPM, particle displacements in the unconfined directions $\langle x^2 \rangle$ and $\langle y^2 \rangle$ represent the same values as for a free DNA molecule in three-dimensions that can be used to quantify the change of DNA contour length. The normalised probability density function of the end-to-end distance, $r = \sqrt{x^2 + y^2}$, of 60, 90, 120 and 160 bp dsDNA molecules tethered with 20 nm AuNPs are plotted respectively in Figure 3.9. The plot presents that the radial distribution function spreads out as the contour length of dsDNA increased. By comparing the effective tether length dependent radial distribution functions, TPM assay can be employed as a powerful tool for probing deformation of biomolecules induced by multiple factors such as protein binding and salt concentration variation.

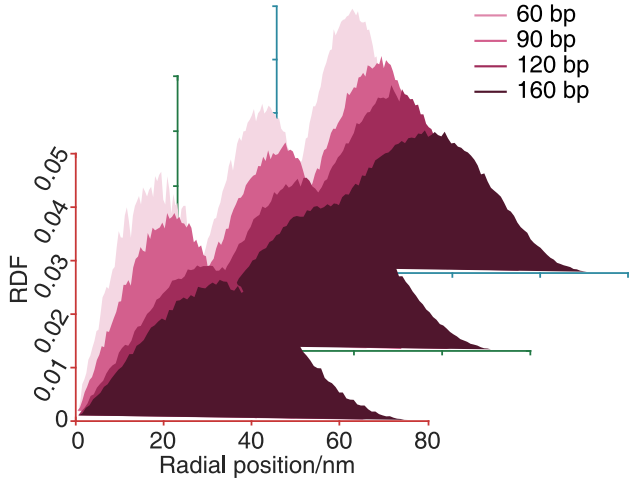


Figure 3.9: Extracted persistence length of short dsDNA length. (a) Observed particle radial distribution functions of 60, 90, 120 and 160 bp DNA strands plotted from three measurements with all the same conditions. Highly reproducible experimental results obtained from a large number of qualified particles lead to accurate estimation of dsDNA persistence length at sub-persistence length scales.

3.3.4 Monte Carlo simulations

The WLC is a well-developed and broadly accepted model to describe the conformations for dsDNA chains of any lengths by introducing the persistence length. In Brinkers's paper,[100] they carried out Monte Carlo simulations of the experiment, which give insight into the flexibility of the DNA. Statistical comparison with the obtained distribution function of reporter bead in the corresponding experiments was performed to determine the persistence length of the dsDNA. Although the WLC model gives precise end-to-end distance distribution of free DNA molecules, it reflects little information on the influence of tethering a nanoparticle to one end of dsDNA molecule with the other end attached to a substrate. Therefore, we carried out Monte Carlo simulations using two models: a. we use the oxDNA model with much more detailed structural information and bond orientations to evaluate that our TPM construct could represent the status of DNA molecule nicely and the volume exclusion effect is negligible in our experiments; b. we carried out simulations using

WLC model to determine the measured persistence length by looking for the simulation with which the observed particle RDF has the highest statistical agreement.

The oxDNA model

The oxDNA model is a coarse-grained model of DNA designed to capture the thermodynamic, structural, and mechanical properties of single- and double-stranded DNA.[175,204,205] It represents nucleotides as rigid bodies featuring three interaction sites and ignores the internal atomic motions of bases, resulting in a better model of sampling of more global large-scale conformational changes. We performed simulations using molecular dynamics to represent the conformations of DNA attached to a nanoparticle. In the simulation, DNA was represented via the oxDNA model,[175] while the nanoparticle and biotin-streptavidin linkage were represented by repulsive particles (Figure 3.10a). Specifically, the bonds connecting the DNA duplex to the surface and to the gold nanoparticle are modelled as a particle with a diameter of 5 nm.[206] The gold nanoparticle is treated as a particle with a diameter of 20 nm. Moreover, an average-sequence representation for DNA was used to avoid any sequence-specific effect on the behaviour of the system.

An example of a simulation setup for the system with a duplex of 120 base pairs and a 20 nm gold nanoparticle is shown in Figure 3.10a. The duplex initially points along the z-axis while the PEG surface is fixed in the $x-y$ plane. The detailed form of the interaction potential (V) and simulation parameters used are described below:

$$V = V_{non-bonded} + V_{bonded} + V_{oxDNA} + V_{wall} \tag{3.19}$$

where $V_{\text{non-bonded}}$ is the non-bonded potential, V_{bonded} is the bonded potential,

V_{oxDNA} is the potential for the oxDNA model, and V_{wall} is the wall potential for modelling the PEG surface. The non-bonded potential is given as,

$$V_{non-bonded} = V_{non-bonded,DNA-linker} + V_{non-bonded,DNA-AuNP} + V_{non-bonded,AuNP-linker} \tag{3.20}$$

For particle type A interacting with particle type B, we have

$$\begin{aligned} V_{non-bonded,A-B} &= 4\epsilon((\frac{\sigma_{AB}}{r_{AB}})^{12} - (\frac{\sigma_{AB}}{r_{AB}})^{6}) + \epsilon \\ &= 4\epsilon((\frac{(R_A + R_B)/2^{1/6}}{r_{AB}})^{12} - (\frac{(R_A + R_B)/2^{1/6}}{r_{AB}})^{6}) + \epsilon \end{aligned}$$

where $R_{\text{DNA}} = 0.335$ nm is the size of a coarse-grained nucleotide backbone bead in oxDNA, $R_{\text{linker}} = 2.5$ nm is the size of the linker, $R_{\text{AuNP}} = 10$ nm is the size of the nanoparticle, r_{AB} is the distance between the two interacting particles, and the pairwise energy ϵ is set to be 2 in simulation units. The interactions were truncated at the minimum of the potential, i.e. $r_{\text{cut}} = 2^{1/6} \cdot \sigma_{AB}$.

$$V_{bonded} = V_{bonded,nucleotide-linker} + V_{bonded,linker-AuNP} + V_{bonded,linker-dummy} \tag{3.21}$$

For particle type A bonded with particle type B, we have

$$\begin{aligned} V_{bonded,A-B} &= \frac{1}{2}\kappa(r_{AB} - r_0)^2 \\ &= \frac{1}{2}\kappa(r_{AB} - (R_A + R_B))^2 \end{aligned}$$

where R_{DNA}, R_{linker} and R_{AuNP} are the same as described above, $R_{\text{dummy}} = 0$ is the size of a fixed dummy particle on the surface that restrains the linker on

the surface, r_{AB} is the distance between the two bonded particles, and κ is set to be 2 in simulation units. There are two nucleotide-linker bonds, one is the linker-AuNP bond and the other is the linker-dummy bond.

For V_{oxDNA}, we took the same model as in Ouldridge's paper.[175]

$$\begin{aligned} V_{wall} &= 4\epsilon((\frac{\sigma}{r})^{12} - (\frac{\sigma}{r})^{6}) + \epsilon \\ &= 4\epsilon((\frac{(R)/2^{1/6}}{r})^{12} - (\frac{(R)/2^{1/6}}{r})^{6}) + \epsilon \end{aligned}$$

where R_{DNA}, R_{linker} and R_{AuNP} are the same as described above, r is the distance of the particle from the wall (the $x-y$ plane), and ϵ is set to be 2 in simulation units. The interactions were truncated at the minimum of the potential, i.e. $r_{\mathrm{cut}} = 2^{1/6}\sigma$.

The simulations were carried out in the canonical ensemble using Langevin dynamics at a temperature of 298 K. The time step is 0.005 in simulation units. 24 simulations are performed for each system, each of which consist of 108 steps. The system configuration was outputted every 104 steps. The RDF for each system was then calculated from the trajectory of all 24 simulations.

We compared RDFs obtained from simulations with our experimental results from TPM experiments and plotted in Figure 3.10b. The RDFs from simulations and experiments are found to be in satisfactory agreement since they have a similar distribution shape. Nevertheless, the RDFs from simulation generally show a shifted peak position and a sharp cut-off of the tail. This discrepancy can be attributed to two possible reasons. The first one could be the simplified treatment of the linkages, which cannot capture their flexibility, and the second reason could be the heterogeneity of different tethered nanoparticles and linkages, which is present in experiments but absent in simulations. Adding

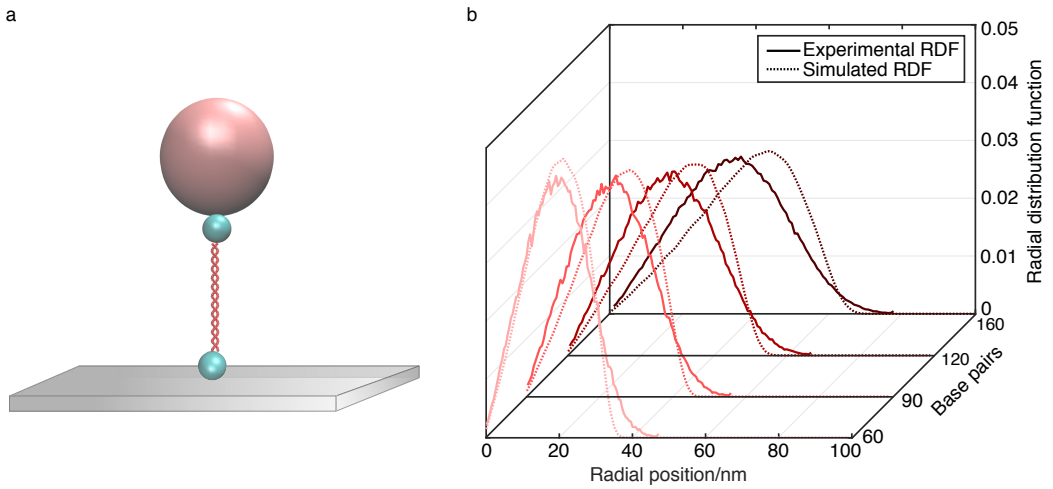


Figure 3.10: coarse-grained molecular dynamics simulations. (a) Concept of the DNA-tethered nanoparticle model in simulations. (b) Particle radial distribution functions (RDFs) obtained from the simulation present a similar shape with our experimental results by TPM measurement.

noise to the simulation data, e.g. the localisation error, could lead to a softer tail of the simulated RDFs.

As described in Ouldridge's paper,[175] one could estimate the l_p through the Eq. 11. Thus, we did the persistence length calculations by following the same method and got 125 bp, 128 bp, 126 bp and 130 bp, for 60 bp, 90 bp, 120 bp and 160 bp dsDNA, respectively, in reasonable agreement with which has been characterised in the paper as about 125 bp (42.5 nm) of a 202 bp DNA duplex. In another oxDNA paper,[205] the persistence length of a short 60 bp DNA duplex was measured at various salt concentrations, and it varies between 135 bp (46 nm) at 0.1 M (Na^+) and 120 bp (41 nm) at 2.0 M (Na^+). However, this is an inaccurate characterisation for our TPM experiments since the persistence length is not a variable in the oxDNA and you almost always get the same number regardless of how your system is constructed.

The WLC model and measured persistence length

We took the same construct as in the oxDNA model, the interactions of the DNA and nanoparticle with the substrate are modelled as hard-wall interactions.

For each DNA configuration, the orientation of the nanoparticle is randomly sampled from a uniform distribution. We also introduce a bending angle potential to the linkers, which restrains the gold-linker-DNA bond angle to be close to 180°, to prevent nanoparticle intersecting with the DNA duplex. We calculate WLC RDFs of the nanoparticle with a series of persistence length starting from 30 bp to 206 bp, equivalent to 10 nm to 70 nm in length, with a step size of 3 bp and sampled 10^5 times for each conformation all lengths including 60 bp, 90 bp, 120 bp and 160 bp. Here, we simulate with 3 bp step size simply because it is roughly the same as the localisation error in my experiment.

We calculated the WLC RDF from literature.[207] The WLC RDF in this paper is an interpolation of many different literature approximations for short, medium and long chains demonstrated to be in good agreement over the full stiffness and extension range. (Figure 12b in ref. 207) It gives a correct RDF for any chain lengths of free molecules, but not for molecules with constrained ends. In order to compare with experiments, the RDF of the nanoparticle is estimated from the WLC model using the following method. First, a random vector is sampled, with its length sampled according to the WLC RDF from equation 21 in reference 207 and its orientation being a random unit vector in 3D. This vector represents the end-to-end vector of the DNA duplex. To estimate the position of the nanoparticle, we add another random vector to the previous vector. This random vector represents the DNA-nanoparticle connection. Its length is 15 nm (radius of bead plus linkage size), and its orientation is a random unit vector in 3D. The sum of these two vectors is the position of the nanoparticle. To calculate the RDF on 2D, we simply calculate bead displacement r from the x- and y-position of the nanoparticle, and construct a histogram of r. Theoretically, the vector of the nanoparticle

should point to the same direction as the vector of the end of DNA because we assume there is no bending from the biotin-streptavidin linkage and the nanoparticle cannot practically bend over towards the duplex. However, we don't know where the vector of the end of DNA is pointing towards in this WLC model because we only have the RDF from literature.

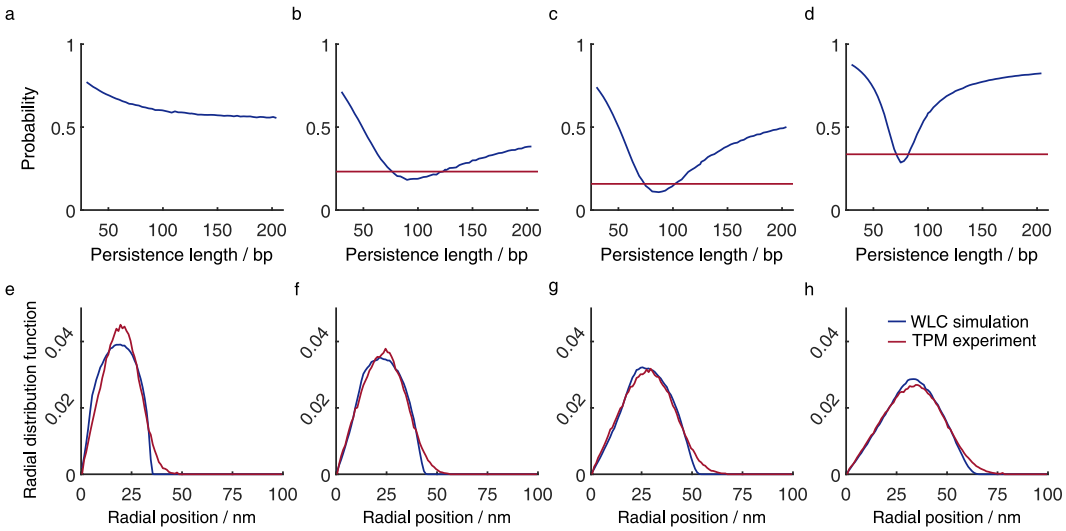


Figure 3.11: Results of statistical t-test for determining the measured persistence length. (a) to (d) Obtained p-value by comparing experimentally obtained particle radial distribution function to simulations using different persistence lengths for 60 bp, 90 bp, 120 bp and 160 bp dsDNA, respectively. Red line in b-d annotates the statistical significance of 0.05. (e) to (h) Particle RDFs obtained from TPM experiments are in the best statistical agreement with WLC simulations at 90 bp, 87 bp and 75 bp, for 90 bp, 120 bp and 160 bp duplex, respectively.

Statistical t-test was applied to find out the simulated persistence length with which the experimental result has the highest statistical agreement. The t-test evaluates the difference between the two RDF curves and returns a p-value indicating the level of disagreement between the experiment and simulation. In figure 3.11, the persistence length of the dsDNA is determined by looking for the minimum probability for the statistical tests with the simulations with different persistence lengths. The measured l_p here is between 78 and 120 bp (90 bp), 75 and 102 bp (87 bp), 72 and 81 bp (75 bp), for 90 bp, 120 bp and 160 bp dsDNA at 0.05 significance, respectively (numbers in brackets show

the persistence length at minimum probability). As shown in Fig. 3.11 f-h, the high degree of agreement between RDFs from simulation and experiment reveals that our TPM assay can track the gold nanoparticle to a reasonably high accuracy compared to simulations. It is sensitive enough to represent the motion of DNA duplex at short length scales. However, our method failed to determine the measured persistence length for extreme short 60 bp duplex, the issue is probably due to the significant size of the tethered 20 nm gold nanoparticle which is comparable to the contour length of the DNA molecule under investigation, leading to a scaling of the mean square radius compared to free molecules. The error introduced by the random motion of tethered particle smears out the details of the RDF of the end of the DNA duplex, resulting in loss of information.

3.3.5 Small conformational changes by DNA-protein interactions

The combination of the TPM technique and the ultra-sensitive TIRSM setup introduces a new method to investigate small conformational changes by protein-mediated DNA bending and looping. Many kinds of proteins are impossible to visualise via an optical microscope due to their small scattering cross sections. However, measuring the decrease of effective tether length that caused by the binding of proteins, by quantifying the change of particle distributions with nanometre localisation precision, directly implies the information of dynamics and conformational change of DNA-protein interaction *in vitro*.

To demonstrate the capability of TPM experiments for probing conformational changes, after preparation of TPM samples and identification of freely mobile single tethered particles, 5 μM DNA binding protein RAD52 in 10 mM HEPES (pH 7.6) and 150 mM KCl were injected into the flow chamber and incubated for 5 minutes. The chamber is then washed with WB before acquiring

the two-dimensional particle distribution within the same FOV. RAD52 will bind to 4 nucleotides of DNA, hence resulting in conformational change of the DNA molecule. Direct comparison of the particle distribution and its radial distribution function are presented in Figure 3.12. A significant drop of particle excursion amplitude and a 15 nm shift of the peak at the largest probability density in the RDF are observed, which indicates that after 5 minutes incubation, multiple RAD52 molecules bind to and interact with the DNA molecule, demonstrating the capability of TPM assay for probing protein-induced DNA bending and looping, i.e. DNA topological changes.

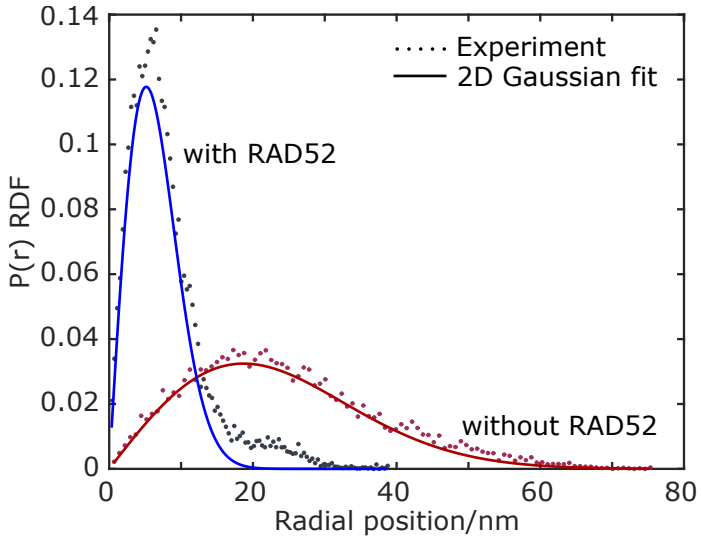


Figure 3.12: Small conformational change by DNA-protein interactions. Conformational change of DNA and observed decrease of particle excursion amplitude due to bindings of RAD52. 2D Gaussian fit of experimental RDFs reveal a significant drop of particle excursion amplitude and a 15 nm shift of the peak at the largest probability density.

3.4 Discussion

3.4.1 Volume exclusion effect

In TPM experiments, the mechanical properties of the DNA molecule under investigation can be extracted from the motion of the reporter bead whose

diffusion represents the configuration of the DNA molecule. However, owing to the proximity of the tethered bead to the coverslip surface, the DNA molecule fails to explore all possible conformations due to the proximity to the glass surface. This leads to inaccurate measurements of the physical properties of the DNA. Using smaller reporter beads allows for probing shorter DNA molecules since the influence caused by bead-surface interactions results in less entropic stretching force on the molecule.[104] This so called volume exclusion effect has been analysed theoretically by Segall et al.[104] and a dimensionless number was introduced to define regimes where the volume exclusion effect is at play. The excursion number N_{R} controls the scaling relation between the particle size and the length of the DNA molecule which is a function of the particle radius R_{p}, the contour length L and persistence length l_{p} of the DNA molecule:

$$N_R = \frac{R_p}{\sqrt{L \cdot l_p/3}} \tag{3.22}$$

When the N_{R} >1, the observed motion is dominated by the bead and the DNA molecule is effectively stretched due to the influence of excluded volume, hence appearing to be stiffer. While when the excursion number is smaller than 1 ($N_{\mathrm{R}} < 1$), the exclusion volume effect becomes negligible and the observed motion is mainly due to structural fluctuations of the molecule.

To assess that various length of DNA were investigated without any perturbation by the volume exclusion effect, excursion number value for TPM measurements of 60, 90, 120 and 160 bp DNA attached with 20 nm diameter gold nanoparticles, using the persistence length of 50 nm cited from literature, the excursion number was calculated as shown below:

As shown in Table 3.1, even for the shortest 60 bp DNA molecule, the excursion number is 0.54 if using a l_{p} of 50 nm, compared to using the extracted l_{p} from our measurement it is 0.84. Both calculated N_{R} are smaller than 1

DNA base pairs	DNA contour length L/nm	N_{R} (use l_{p}= 50 nm)
60 bp	20.4 nm	0.54
90 bp	30.6 nm	0.44
120 bp	40.8 nm	0.38
160 bp	54.4 nm	0.33

Table 3.1: Excursion number for various DNA lengths, which were investigated with reporter beads of 20 nm gold nanoparticle in diameter. N_R was calculated using generally accepted persistence length of dsDNA of l_{p}= 50 nm.

which indicates that all measurements were carried out in a regime where the physical properties of the DNA molecule remain unaltered. To conclude, the volume exclusion effect should be negligible for all measurements since the reporter beads used here are as small as 20 nm gold nanoparticles in diameter.

3.4.2 Heating effect of gold nanoparticles

The heating of gold nanoparticles due to light adsorptions poses another potential problem for studying the flexibility of DNA molecules in TPM experiments. In order to achieve a high SNR level, illumination light with the wavelength (520 nm) which is close to the surface plasmon resonant frequency of gold nanoparticles (∼520 - 570 nm)[208] is selected to provide plasmon enhanced scattering signal from the reporter beads.[209–211] On the other hand, under the plasmon resonance condition, the gold nanoparticle strongly absorbs light energy due to the large absorption cross-section, resulting in an increase in local temperature.[209] The localised heating effect gives rise to a series of problems. For instance, the increased surface temperature of the gold nanoparticle could lead to streptavidin detachments or break the biotin-streptavidin linkage, which further turns into the loss of reporter bead, i.e. heat induced protein degradation. Although the light energy is absorbed by the gold nanoparticles, heat dissipated

from the particle to the surroundings and the DNA molecule can induce melting of double-stranded DNA if the melting temperature is reached.[212] Furthermore, several experiments have shown that the local temperature rise causes the DNA molecule to appear more flexible due to breaking a few hydrogen bonds between complementary bases.[171,213]

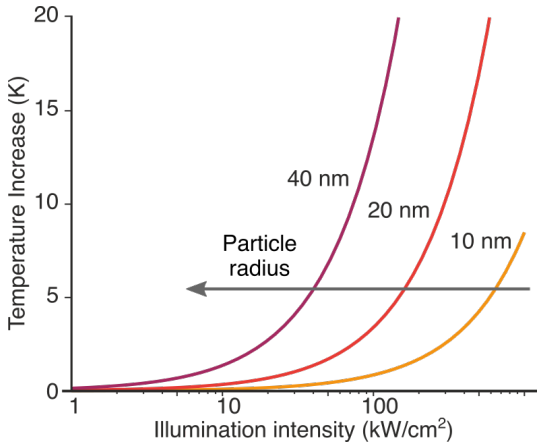


Figure 3.13: Theoretical calculation of temperature increase on surface. Theoretically calculated maximum temperature increase on the surface of a single gold nanoparticle induced by absorption of incident light at 520 nm.[209]

However, based on theoretical models the local temperature rise can be calculated and serve as a guide to determine whether the heating effect is significant. As plotted in Figure 3.13, given the 4.5 kW/cm^2 integrated power density of the pulsed illumination, results in a local temperature rise at the surface of the gold nanoparticle of about 0.2 K. Therefore, the heating effect of the gold nanoparticle on the DNA molecule is negligible for all TPM experiments carried out in this thesis.

3.5 Conclusion and outlook

In conclusion, I have shown that optimisation of a total internal reflection-based dark field microscopy can achieve exceptionally high signal-to-background images of 20 nm diameter gold nanoparticles, allowing for few nanometre locali-

sation precision even with <10 μs exposure time with synchronous stroboscopic illumination. Using such small scattering labels, tethered particle motion enables the study of much shorter DNA strands than possible to date, without significant surface interference. I have shown that my experiments assay can track the gold nanoparticle to a reasonably high accuracy compared to simulations. It is sensitive enough to represent the motion of DNA duplex at short length scales. By taking advantage of these imaging capabilities, the flexibility of double-stranded DNA at sub-persistence lengths scales has been measured. Measurement of the tethered particle radial distribution, from the particle excursion projected in two-dimension, by comparing experimentally obtained particle RDF to WLC model simulations using different persistence length for DNA from 60 to 160 base pairs, respectively. The measured persistence lengths varied from 75 bp to 90 bp, which is slightly short than the broadly accepted 145 bp (50 nm). In addition, I demonstrated the capability of this assay to detect nanoscopic conformational changes by observing protein-mediated bending of DNA and showed that protein-induced DNA deformations can be distinguished from nonspecific binding events.

The future in DNA topological or conformational change studies will require more effort on both the theoretical and experimental approaches to determine the more detailed mechanical parameters for different length scales, especially in the 'nanoscopic regime'. On the one hand, WLC model has been intensively studied by TPM experiments with long DNA length which predicts DNA molecules to be strictly rigid under persistence length scales. In spite of modified WLC models[179,214] and the nonharmonic elastic model being developed[80] to account for the extreme bendability of short length DNA, due to formation of local kinks[215] and minicircles,[216,217] the field still requires a better mathematical interpretation of these different length scales of DNA. Nevertheless, a new model

which could well explain our TPM experiment data with DNA shorter than the persistence length is still required, and currently does not exist in literature. On the other hand, developments can be conducted on the design of more intricate experiment assays. In order to elucidate whether the high flexibility is caused by local kinks on DNA, a control experiment of particle tethered DNA molecules with nick or mismatch between complementary nucleotides can be performed in the future as an extension of this study. With high localisation accuracy of TIRSM, one could distinguish the difference of RDF between tethers with nick on it and normal tethers. In addition, applying microfluidics jointly with the work presented in this thesis can provide means to precisely control the salt concentration in buffer inside of an experimental chamber, while monitoring the same DNA tethers for different buffer conditions, thus enabling the investigation of the dependence of DNA flexibility on ionic strength with higher accuracy. Finally, with further calibrations, important structural information of DNA-protein interactions in an aqueous environment which has not been achievable by other force-free single molecule techniques can be estimated from the measurement of the degree of protein-mediated kinking/conformational change of the DNA.

Chapter 4

Sensing force and charge at the nanoscale with a single molecule tether

4.1 Introduction

The quantification of forces at the single molecule level has become a widely used method to understand biomolecular dynamics and function. Optical tweezers[23,76,218,219] and scanning probe methods such as AFM[80,220] have been the dominant approaches due to their exquisite levels of sensitivity and speed.[85,90,221] Nevertheless, both approaches have their own intrinsic limitation. Specifically, for the optical trapping method, the physical connection of a macron-sized bead to the molecule of interest introduces vibrations from the aqueous environment that prevents the investigation of minor conformational changes.[90] Whereas for the scanning probe method, external mechanical stimuli imposed on molecules is the largest concern which undoubtedly alters the flexibility and elasticity of molecules.[222] In parallel, force-free methods such as tethered particle motion,[83] in which the mechanical properties and conformational changes of a molecule are imprinted on the motion of a reporter bead attached to the molecule bound to a surface, have provided powerful alternative means to studying bio-polymers such as DNA,[99,100] and related molecular processes such as protein-mediated

DNA interactions and their mechanical consequences.[101,223–226] Nevertheless, for all the aforementioned techniques, a frequently faced challenge in the context of force measurements is throughput, limiting the obtainable statistics.

The majority of TPM studies have relied on the use of reporter beads with diameters >100 nm to maximise simultaneous localisation precision and temporal resolution required to monitor the bead motion with sufficient accuracy.[100,227] The convenience of a large optical signal comes at the expense of the inability to study the dynamics of short tethers due to volume exclusion effects near interfaces.[104] Recently, Lindner et al. have combined TPM with total internal reflection illumination and dark-field microscopy to extract the spring constant of DNA with a contour length of $L = 925$ nm tethered to a 80 nm diameter gold nanoparticle, achieving 10 nm localisation precision and 1 ms time resolution.[105]

Using smaller particles is important to minimise the influence of particle motion on the bio-polymer dynamics,[104] and to measure conformational changes and transitions from small molecules.[228] The scattering cross section decreases with the sixth power of the particle diameter, therefore making the imaging and tracking of smaller particles a significant experimental challenge. This is a particular problem in the context of rapid diffusion, which results in positional blurring. Furthermore, the larger the particle, the more difficult is detection and quantification of any changes affecting the particle motion, such as charge or viscosity.

I have previously shown in chapter 3 that optimised total internal reflection-based dark field microscopy (Figure 4.1) can achieve exceptionally high signal-to-background ratio images of 20 nm diameter gold nanoparticles on microscope cover glass, allowing for few nanometre localisation precision even with <10 μs exposure times. Such a short exposure time reduces the positional blurring.

Taking advantage of these imaging capabilities, here we present a molecular force sensor and charge detector based on parallelised imaging and tracking of tethered double stranded DNA functionalised with charged nanoparticles interacting with an externally applied electric field. Tracking the position of the tethered particle with simultaneous nanometre precision and microsceond temporal resolution allows detection and quantification of electrophoretic forces down to the femtonewton (10^{-15} N) scale. Furthermore, we demonstrate that this approach is capable of detecting changes to the particle charge state, as induced by the addition of charged biomolecules or changes to pH. This approach provides an alternative method to studying structural and charge dynamics at the single molecule level.

4.2 Experimental methods

4.2.1 TPM sample preparation and oscillating electric field implementation

Flow chambers and TPM samples were prepared following the procedure as described in chapter 2. For all measurements in this chapter, only 160 bp dsDNA (ATDBio Ltd, Southampton, U.K.) was used.

To apply an electric field parallel to the coverslip surface, two platinum electrodes were placed on both sides of the flow chamber. Both electrodes were wired to a power amplifier with amplitude and frequency controlled by an external function generator. In order to ensure reliable electrical connections between two electrodes and the electrolyte, epoxy was used to firmly attach the electrodes onto the surface and create barriers outside both the inlet and outlet of the flow chamber. Enough buffer solution was added inside the barriers to ensure that electrodes were completely immersed, and thereby in good contact with electrolyte inside the flow chamber. The resistance between the two

platinum electrodes ($2 < R < 5$ MΩ) was measured and monitored to confirm a good electrical contact.

4.2.2 Dark-field microscopy

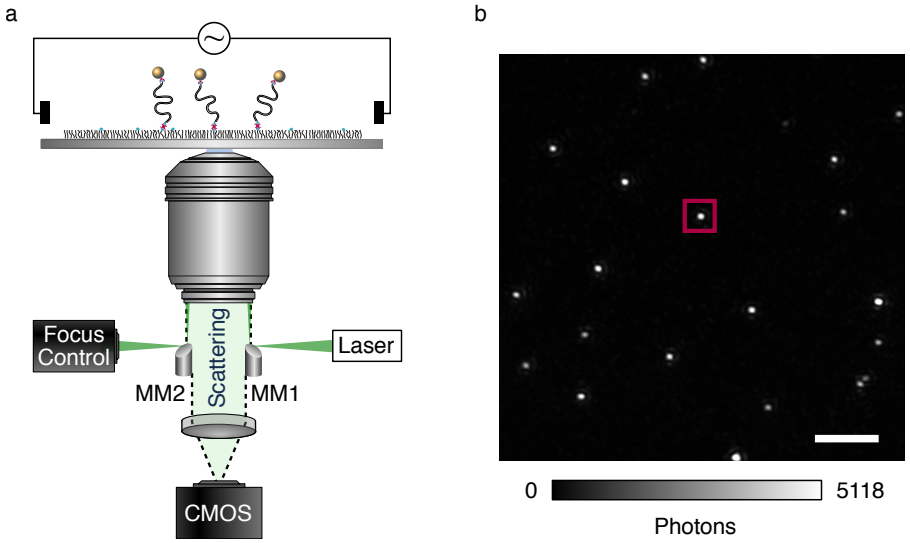


Figure 4.1: Dark-field microscope and concept of applying an alternating electric field. (a) Simplified schematic of the microscope setup and diagram of the DNA-tethered particle construct in the presence of an external electric field. External electric field was applied via two platinum electrodes. (b) Dark-field image of single molecular sensors. Scale bar: 3 μm.

The dark-field microscope (Figure 4.1) used here was the same as described earlier and the instrument settings for tracking tethered particles were the same as described in chapter 3. To maximise the scattering signal, a 520 nm wavelength laser was selected as the illumination beam on the basis of using gold nanoparticles as reporter beads. The scattered light from individual gold nanoparticles was collected by a high NA objective and focused by a lens onto a complementary metal–oxide–semiconductor (CMOS) camera (Point Grey Grasshopper GS3-U3-32S4M-C). Using a 200 mm focal length imaging lens in combination with the camera and the objective yields a pixel size of 51.7 nm/pixel with a FOV of 25×25 μm^2. Images were first acquired with pulsed illumination at 6 μs exposure time. These high-speed data were

analysed for selecting qualified sensors and extracting effective spring constants before starting the force/charge measurement. After this, variations exist in terms of the excitation beam and the operation mode compared to settings in chapter 3. First, in addition to the primary illumination beam, a reference beam (445 nm) was aligned to flag the reverse of potential of the applied electric field. The blue laser was turned on at each point when the potential was reversed hence resulting in a temporary increase of background signal which could be distinguished in the data analysis. Secondly, after acquiring the high-speed data, the pulsed illumination beam (520 nm) was switched to continuous wave mode and the exposure time was increased to 2 ms for the force/charge measurement.

4.2.3 Characterisation of individual effective spring constants

Diffusive motion of the single-tethered particle, induced by thermal fluctuations, matches a normal distribution. This enables us to model the DNA tether as a classical harmonic oscillator (Figure 4.2). As there is variability among the elastic properties of dsDNA molecules and their binding configuration on the nanoscale, each tether is considered individually. Monitoring each tether individually also enables the detection of small conformational changes and binding(unbinding) events where such stochastic behaviour is typically averaged out in ensemble measurements.

At thermal equilibrium, the probability of finding the particle in a state with energy $E = K + V(\vec{r})$ is $P(\vec{r}) = \frac{1}{Z} e^{-E/k_{\mathrm{B}}T}$, with Z the partition function, k_{B} the Boltzmann constant and T the temperature. In the over-damped regime, the kinetic energy K averages to zero, making the particle mass irrelevant since

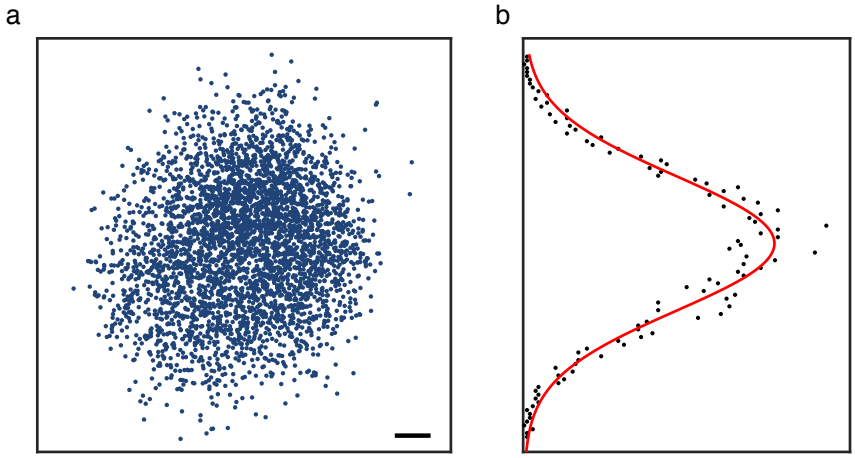


Figure 4.2: Particle diffusive motion. (a) Thermal fluctuations induced diffusive motion of single-tethered particle. Scale bar: 10 nm. (b) Probability density function $P(x)$ of x displacement in (a). The motion matches a normal distribution that allows us to consider the DNA tether as a classical harmonic oscillator.

all inertial motion is damped by friction, and leading to the potential

$$V(\vec{r}) = -k_{\mathrm{B}}T \log Z - k_{\mathrm{B}}T \log P(\vec{r}) \tag{4.1}$$

We can conclude the (local) minimum of the potential coincides with the position where the particle is found most often. At this point $\frac{dV}{d\vec{r}} = 0$. Without losing generality, the origin is normalised to the minimum potential of the particle distribution. If we (Taylor) expand the potential around its minimum,

$$V(\vec{r}) = V_0 + \frac{1}{2}\kappa_{\mathrm{H}}(x^2 + y^2) + \frac{1}{2}\kappa_z z^2 + O(r^3), \tag{4.2}$$

where κ_{H} denotes the effective in-plane spring constant and κ_z the spring constant in the z-direction. Displacement in the z-direction involves stretching the DNA and therefore in general $\kappa_z \neq \kappa_{\mathrm{H}}$. In general, κ_{H} could be obtained by taking the second derivative of the experimentally measured $\log P(x)$ around its maximum. However, based on these measurements, the observed particle distribution matches a Gaussian function $P(x) \propto e^{-x^2/2\sigma^2}$, thus for an acceptable approximation, the effective spring constant

$$\kappa_{\mathrm{H}} = k_{\mathrm{B}}T/\sigma^2 \tag{4.3}$$

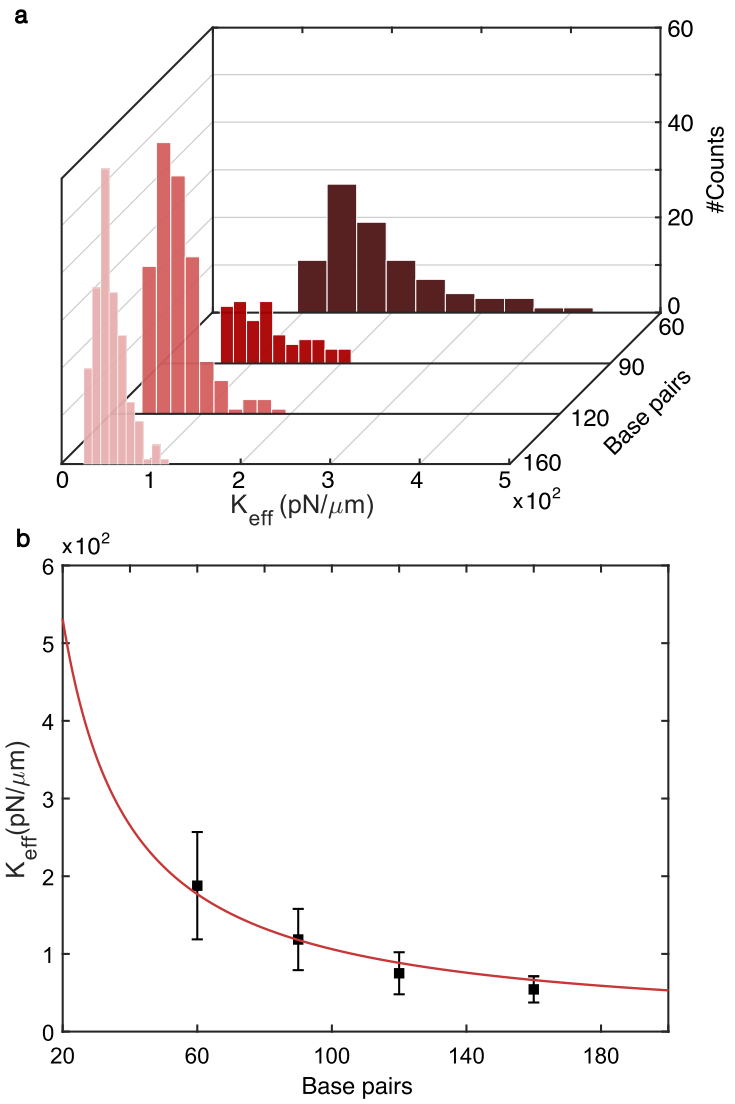


Figure 4.3: Measuring effective spring constant by thermal fluctuation. (a) Distributions of effective spring constants extracted from P(x) of 60, 90, 120 and 160 bp dsDNA (N = 88, 73, 197 ,210). (b) Effective spring constants versus the length of DNA tethers, one base pair equals to 0.34 nm. We obtained the product of Young's modulus E and the cross-sectional area A from the fit (red line), E = 114.9 ± 18.5 pN· nm^{-2} for R = 10 Å.[76,229]

where σ is the standard deviation of particle distribution from a Gaussian fit. We can thus quantify κ_{H} for each tether individually. For example, based on the experimental data acquired in chapter 3, we obtained average values of the effective spring constant for dsDNA tethers consisting of 60, 90, 120 and 160 base pairs, at pH 7.6, and plotted them in Figure 4.3, respectively. Since

the tensile stress is given by $\sigma_{\text{stress}} = F/A$ and the tensile strain is given by $\varepsilon_{\text{strain}} = x/L$, the Young's modulus can be expressed as:

$$E = \frac{\sigma_{\text{stress}}}{\varepsilon_{\text{strain}}} = \frac{F/A}{x/L} = \frac{F \cdot L}{x \cdot A} \tag{4.4}$$

where A denotes the cross-sectional area of the material and L the length of the spring. According to the Hooke's Law, the effective spring constant is given by

$$\kappa = \frac{E \cdot A}{L}. \tag{4.5}$$

Thus, the effective spring constant of dsDNA molecules which have the same cross-section area (A) and the same GC content (same Young's modulus E) is inversely proportional to the contour length. The effective spring constants obtained from my previous experimental results fit well to the theory (Figure 4.3b). These results demonstrate that the assay cannot only characterise and resolve differences in mechanical properties of different dsDNA tethers, but also suggest that they may be used to quantify forces on the sub-piconewton scale.

4.2.4 Measuring the displacement when applying external electric field

To test the ability of measuring forces on femtonewton (10^{-15} N) scales, after measuring the effective spring constant of each dsDNA tether in the FOV at high speed, an external electric field was applied across the flow chamber. Assuming that the DNA-bead construct is charged, one would expect the centre of mass of the tether to change depending on the polarity of the applied field (Figure 4.5a). The polarity of the applied field was alternated at a frequency of f = 0.5 Hz and the reference beam (445 nm) was simultaneously triggered

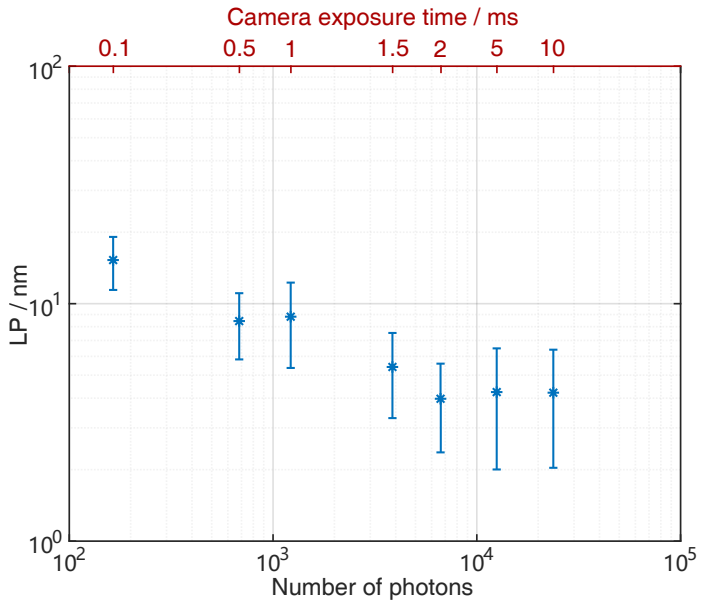


Figure 4.4: Characterisation of localisation error. Given a fixed incident light intensity, localisation error is re-characterised to determine the optimal camera exposure time to ensure the highest tracking precision by averaging out the nanoparticle diffusive motion.

with the EF by a synchronised pulsed signal (f = 1 Hz, 10% duty ratio) to identify the reversing of the EF polarity from captured frames (Figure 4.5b). In contrast to the previous measurements where we needed to essentially freeze the position of the reporter bead to accurately sample its motion, because only the averaged displacement was of interest in these experiments, the illumination laser was therefore switched from pulsed illumination to continuous wave mode when carrying on the force measurement, and the camera exposure time was increased to 2 ms (Figure 4.4) to average out the nanoparticle diffusive motion. Centre of mass (COM) positions of a tethered particle were grouped into POS cycles and NEG cycles (Figure 4.5) according to the direction of applied potential when it appeared. The particle displacement in the present of the alternating EF was calculated based on the distance between the averaged COM position in POS cycles and NEG cycles. We used statistical t-test to further exclude tethered molecules with no statistically significant difference

between distributions where the p-value is great than 0.05 when the EF is at work.

4.2.5 Extracting charge variations from the measured displacement

In the last analysis step, to obtain the charge on the tethered particle from the measured displacement, we followed a similar approach to what has been developed for (micrometer-sized) particles in optical tweezers.[230] From the textbook treatment of a freely diffusing charged particle under the influence of an electric field in a polyelectrolyte solution, we find that the zeta potential ζ is related to the drift velocity v_d of the particle by the Helmholtz-Smoluchowski equation

$$\zeta = \frac{\eta v_d}{\epsilon\epsilon_0 E}, \tag{4.6}$$

where η and $\epsilon\epsilon_0$ are the viscosity and the absolute permittivity of the medium. This relation is valid in the absence of electro-osmosis and at low frequencies when relaxation effects of the electric double layer are negligible. Since in the steady state, the electrophoretic force F_e is balanced by the viscous drag, the Stokes relation can be used to write $F_e = -3\pi d\eta v_d$, where d is the particle diameter, which leads to the relation between the zeta potential and the electrophoretic force.

$$\zeta = \frac{F_e}{3\pi\epsilon\epsilon_0 dE}, \tag{4.7}$$

For a tethered particle, the drag force is zero (on average) but F_e is balanced instead with the retention force of the tether given by $F_r = -\kappa_{\mathrm{H}}\Delta x_{\mathrm{COM}}$. Therefore, for a tethered particle with charges on it under the effect of an electric field

$$\zeta = \frac{\kappa_{\mathrm{H}}\Delta x_{\mathrm{COM}}}{3\pi\epsilon\epsilon_0 dE}. \tag{4.8}$$

To obtain the charge from the zeta potential, assuming all the charge is distributed on the nanoparticle surface, we could use the Gouy-Chapman equation for the surface charge density σ. Considering $q = \pi d^2 \sigma$,

$$q = \pi d^2 \sqrt{8\epsilon\epsilon_0 k_B T n_0} \sinh \frac{e\zeta}{2k_B T}, \tag{4.9}$$

where n_0 is the number density of univalent ions present in the solution and e is the elementary charge.

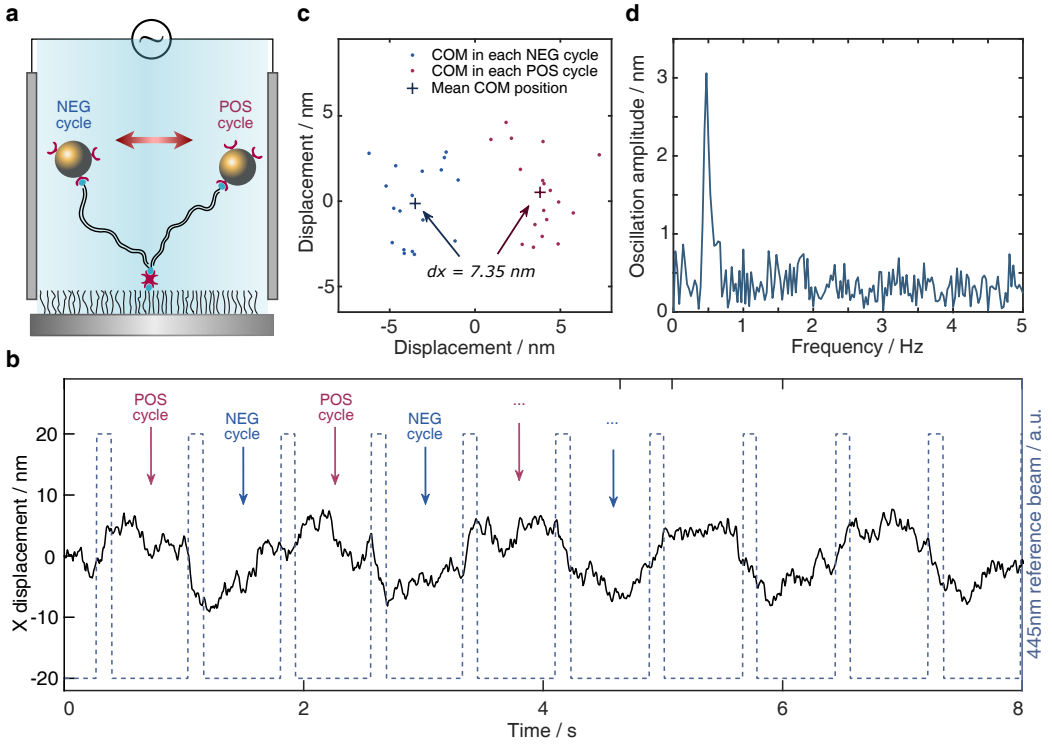


Figure 4.5: Response of a molecular sensor to the applied alternating electric field. (a) Schematic of a single tethered particle in the presence of an electric field. Centre of mass positions of the particle were grouped into POS cycle and NEG cycle based on the direction of the applied electric field. (b) Particle oscillating along X axis (in black) in the presence of an applied potential 80 V peak-to-peak at 0.5 Hz (camera frame rate is 150 FPS). (c) Particle displacement is calculated from the distance between COM obtained from the average positions of all POS cycles and all NEG cycles, respectively, in one measurement. For the particle shown here, the particle displacement is 7.35 nm with 18 cycles in total. (d) Fourier transform of the particle trace shown in (b).

A more accurate description of the electrophoretic displacement requires finite-element simulation of the complete tether-nanoparticle system, which is

beyond the scope of the current work.

4.3 Results and discussion

4.3.1 Identification of molecular sensors and source of errors

As with the study of DNA flexibility described in chapter 3, multi-tethered and immobilised particles can introduce artefacts and uncertainty in the characterisation of the effective spring constant, and thereby leads to failure of accurate force and charge measurements. Inherent to the self-assembly process of these molecular force sensors, stuck beads are potentially present, sometimes caused by incomplete surface passivation. Despite the use of gold nanoparticles in excess of DNA molecules during incubation, which helps to minimise the presence of the multiple attachment of DNA tethers to a single gold nanoparticle, multi-tethered beads cannot be totally eliminated. An additional assessment of the distribution amplitude of tethered particle motion in the absence of electric field after the force measurement, together with three criteria described in chapter 3, were carried out to exclude any possible permanent collapse due to the application of an external electric field. After procedurally excluding all faulty tethered tracers, only a single tethered fully mobile particle which is still free to undergo Brownian motion by thermal fluctuations in solution after applying the external electric field will be used as a qualified molecular sensor. In this part of the study, of all the measurements being carried out, about 70% of all imaged tethers qualified as molecular sensors. In summary, the selection criteria for a qualified sensor are as follows:

1. A single-tethered fully mobile particle

2. After switching off the applied EF, both the tethered particle and molecule

remain active and recover to the freely diffusive motion by thermal fluctuations.

Error in this part of the work was mainly from lateral sample drift. An evident sample drift induced by the temperature change was observed, in particular with the externally applied electric field via electrodes, introducing extra localisation errors together caused by shot noise. However, this sample drift can be easily corrected by applying a low-pass filter on particle trajectories and subtracting contributions of the low frequency drift from genuine particle displacements. Another systematic uncertainty is the possible damage of dsDNA tethers due to multiple mechanical oscillations of bead positions. Special care was taken during experiments to avoid any possible artefacts in the following ways: data was acquired as soon as possible once the electric field is applied and any flow chamber with samples were not used more than 30 minutes after tether assembly was complete.

4.3.2 Force measurement with external electric field

Upon the presence of an alternating electric field, effectively charged nanoparticles were forced to shift away from their equilibrium positions. As a result, the stretched dsDNA acts as a nanospring under forces on the sub-piconewton scale. Its deformation was monitored by tracking the scattering signal from the tethered nanoparticle with simultaneous nanometre spatial and microsecond temporal resolution, enabling the simultaneous force measurement of multiple tethers for high throughput study. As described, application of an 80 V peak-to-peak (Vpp) square waveform potential at 0.5 Hz results in a displacement of the tether. The corresponding bead position along the axis of the applied potential reveals clear oscillatory behaviour in the X trace after applying an low-pass filter on the X trace over time (Figure 4.5b). Performing a Fast

Fourier transform on the raw data exhibits a dominant feature at 0.47 Hz, the fundamental harmonic of the damped harmonic response (Figure 4.5d), with the difference attributable to the communications delay between the imaging camera and the interfacing hardware. The imaging noise can be further reduced by averaging to obtain a mean position for each direction of the applied potential, demonstrating clear separation, in this case, approximately 7.35 nm driven by the electrophoretic force (Figure 4.5c). Following the expansion of potential energy as in Eq. 4.2, the exerted force on this DNA tether is calculated as 235±14 fN given a measured effective spring constant of $\kappa_{\mathrm{H}} = 32 \pm 2$ pN/μm.

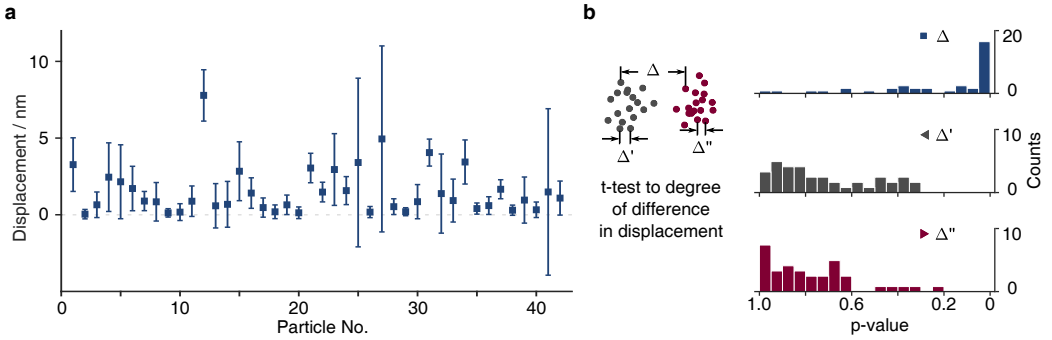


Figure 4.6: Particle displacements for different tethers. (a) Particle displacements from a single field of view ranging from 0.15 nm to 8.23 nm (N = 42). (b) Statistical t-test was carried out to exclude tethered molecules with no statistically significant difference between distributions where the p-value is great than 0.05 in the presence of potential (△). Corresponding statistical t-test results (△' and △") reveal that particle displacements are very similar within the same potential polarity.

The same analysis was then repeated on all free particles (42 for the measurement shown in Figure 4.6) visible in a field of view. After exclusion of multi-tethered and stuck particles, a wide variety of displacements ranging from <1 to 5 nm were observed, likely due to differences in the tether charge and surface attachment (Figure 4.6a).

However, previous assessments on selecting qualified molecular sensors failed to exclude outliers without significant difference between average positions in the presence of electric field. Given the large error bars for the displacement

compared to its magnitude (Figure 4.6a), a statistical analysis is therefore performed to test whether the average positions for opposite potentials were indeed different within the error of the measurement. 20 out of 42 tethers exhibited $p < 0.05$ (Figure 4.6b, △). In addition, comparisons of particle positions in consecutive negative (△') and positive potentials (△") were carried out, which exhibited dramatically different behaviours (Figure 4.6b) for opposite potentials but similar behaviours within the uniform potential. These results suggest that I am indeed able to resolve even very small displacements in the centre of mass caused by the electrophoretic force.

Finally, a screening test of the tethered particle motion after switching off the electric field was performed to inspect the viability of every sensor. Only those tethers which recover from the oscillating movement will finally qualify as molecular sensors. In this work, of all the measurements carried out, ∼10% of the tethers had satisfied all eligibility criteria for the final force measurements.

4.3.3 Displacement dependence on applied electric field potential

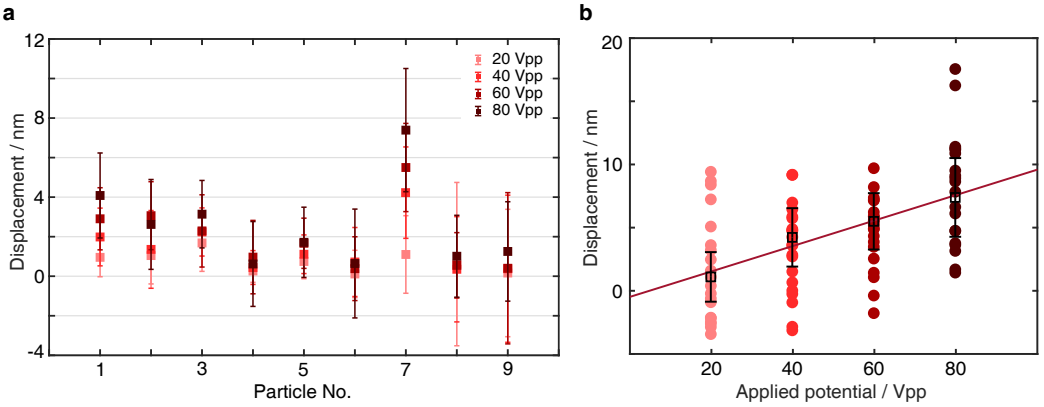


Figure 4.7: Displacement dependence on applied electric field potential. (a) Particle displacements at different applied E-field potentials. (b) Measured displacement (particle 7 in (a)) versus applied electric field potential.

In order to further verify the displacement dependence on applied EF

potential, the amplitude of applied potential was changed from 20 Vpp with a 20 V increment up to 80 Vpp to study the force-dependent variation of the displacement. The FOV remained unchanged throughout the measurement. At each applied potential, images were acquired under the same conditions and the same analysis was performed as outlined above for 9 different particles (Figure 4.7a). In all cases, Figure 4.7b shows an increase in the centre of mass displacement with applied voltage, exhibiting overall roughly a linear dependence as expected for an electrostatic interaction.

4.3.4 Changes in charge due to intermolecular binding events

The nanoparticle equivalent to changing the applied potential involves changing the charge on the nanoparticle for a fixed potential. To explore this mechanism, two different experiments were performed. In the first, excess biotinylated dsDNA molecules were added to the chamber after an initial displacement measurement. These biotin-dsDNA will specifically bind to unoccupied streptavidin binding sites on the nanoparticle surface, and thereby change the particle surface charge. As expected, a clear increase was observed in the displacement upon addition of charged molecules to the reporter bead surface (Figure 4.8a, b). The displacement increase ranges from 1.24 nm to 3.88 nm, corresponding to a 8.1 mV and 25.3 mV change in zeta-potential and 369e and 1227e charges caused by the number of biotin-dsDNA molecules that bind to each nanoparticle.

4.3.5 Zeta-potential variations due to pH value

In a second demonstration, we changed the zeta-potential by varying the pH value of the working buffer. Because the gold nanoparticles that being used are functionalised and covered by excess streptavidin molecules, the surface

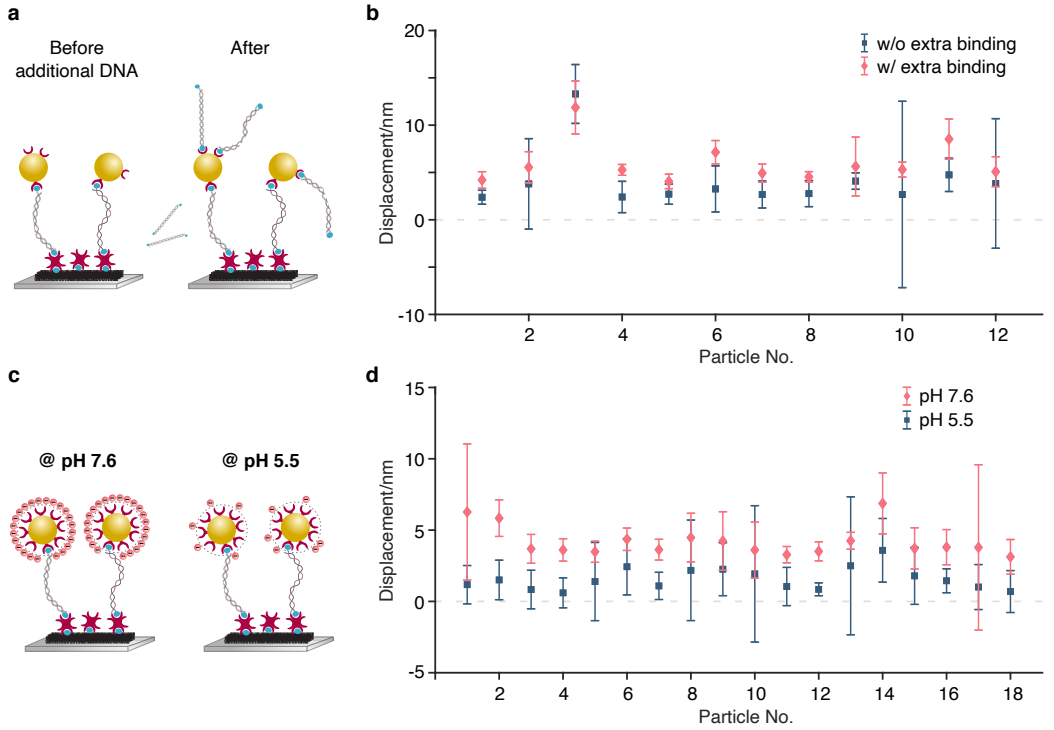


Figure 4.8: Dependence of particle displacements on nanoparticle charge for a fixed potential. (a) Binding of additional biotinylated dsDNA molecules to a streptavidin functionalised particle. (b) Increase in particle displacements upon binding additional biotinylated dsDNA to the reporter bead surface. (c) Schematic indicating a change of tethered particle surface charge caused by buffer pH value alteration. (d) Corresponding change of particle displacements..

charge on the particle is dominated by protein rather than the charge on gold nanoparticle itself. Streptavidin has an isoelectric point (pl) between 5 and 6.[231] Therefore, particle displacements were measured respectively at pH 7.6 and pH 5.5 with the flow chamber being washed using corresponding buffer in between. At pH 5.5, each tethered particle only carries a few charges and is nearly electrically neutral. The particle displacements are considerably larger at pH 7.6, increasing from 1.51 nm to 5.84 nm, corresponding to a 32.8 mV change of the zeta potential (Particle No. 2 in Figure 4.8d).

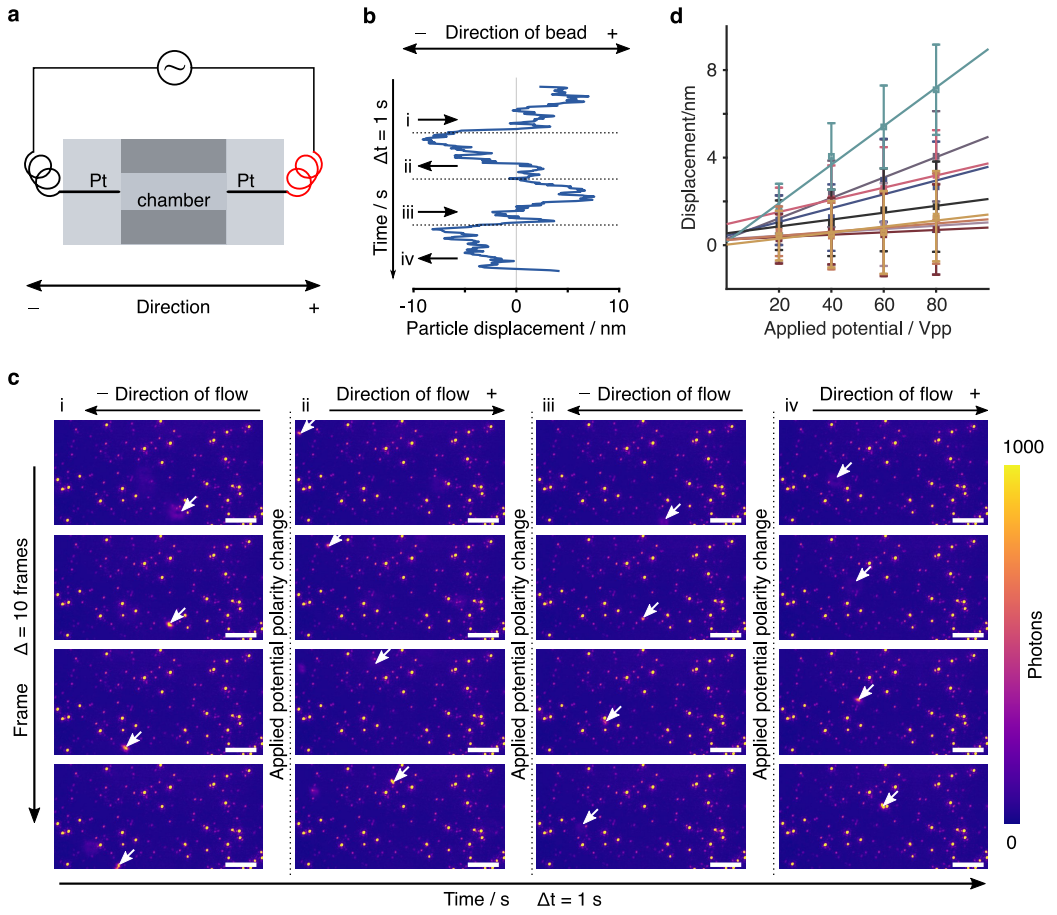


Figure 4.9: A negatively charged particle moves in the direction opposite to the direction of electro-osmotic flow in the presence of EF, ruling out the effect of EO flow. (a) An illustration shows the wiring of electrodes and our definition of the direction of motion. (b) Directions of motion of the tethered particle (same particle in Fig. 4.5) in the first 4 cycles. Dotted line indicates the change of polarity of applied potential. (c) Directions of flow within corresponding cycles in (b). We predicted the direction from known polarity of applied EF and confirmed that by observing the motion of unbound objects. (d) Different particle displacement due to nanoparticle surface charge variations (slope). This suggests that the particle displacement is electrophoretic force dominated.

4.3.6 Ruling out the effect of electro-osmotic flow

The counterions that screen a charge surface cause the EO flow under external electric field, even if the neutral PEG coating covalently bound to the silica surface could shield this effect and hence reduce the EO force. It is hard to quantitatively model it due to possible local surface nonuniformity. To rule out this effect, I predicted the direction of EO flow from known polarity of

applied potential and confirmed that by observing the direction of motion of freely diffusive particles or dirt in buffer solution (Fig. 4.9c). Since the tethered particles are negatively charged at pH 7.6, in the presence of EF, I found that the direction of the tethered particles motion is in fact opposite to the direction of flow as expected. In addition, I have discussed previously that the relation between the external electric field and the tethered particle displacement (Eq. 4.8) holds when the electro-osmotic (EO) flow is negligible. Observing a large range of displacements between nearby tethered particles (Fig. 4.9d) confirms experimentally that electrophoretic forces are much larger than those caused by the EO flow, which should cause the comparable displacement on adjacent particles.

4.4 Conclusion and outlook

In this chapter, I have demonstrated a tethered particle motion assay with 20 nm diameter reporter beads, maintaining simultaneous nm localisation precision and μs temporal resolution in a wide-field imaging configuration. These experimental capabilities enable the efficient identification of free, single tethers and characterisation of their mechanical properties on a molecule-by-molecule basis. By applying an alternating potential across the sample chamber, I can further characterise the charge properties of the tether, accessing femtonewton scale forces. In addition, by monitoring the position of reporter beads driven by electrophoretic force, I have experimentally demonstrated the dependence of the variations in their surface potential on surrounding pH values as well as on the binding of supercharged biomolecules. The experimental results present a highly efficient, high-throughput approach to monitor the dynamics of biomolecular interactions based on the alteration of their effective charge. I anticipate that this assay will provide alternative routes to study

binding-unbinding dynamics and kinetics of biological molecules at the single particle level. By detecting changes in charge rather than mass, NJ Tao et al. has developed various methods and demonstrated applications in detecting small molecule binding,[232] measuring binding kinetics and affinities of low molecular mass ligands with a nanodisc encapsulated membrane protein[233] and quantifying the size, mobility and charge of single proteins.[234] Specially comparing with the label-free surface plasmon resonance (SPR)[235,236] method where the detection signal scales with the molecule weight, such charge-sensitive technique enables the detection of both high and low mass molecules.

There are many prospects for future work to further apply and develop the method of the tethered particle construction combined with dark-field detection. For instance, double-stranded DNA can be replaced by a single-stranded DNA which is much more flexible and thus offers a lower effective spring constant and therefore possibilities of force measurements on sub-femtonewton scales with higher accuracy. However, the negatively charged characteristics of DNA strands, make it difficult to decouple the molecular contribution on particle displacement. Future experiments will greatly benefit from using neutrally charged polymers, such as PEG,[232] to achieve accurate force measurements. Furthermore, one could turn this assay to a single-molecule manipulation method by applying flow force[237] instead of electrophoretic force created via electrodes.

Chapter 5

Nanoscale imaging of the electric double layer

This chapter has been adapted from the following publication: K. Namink, X. Meng, M. Koper, P. Kukura and S. Faez, Electric-Double-Layer-Modulation Microscopy, *Physical Review Applied*, 2020, **13**, 044065,[238] doi: 10.1103/PhysRevApplied.13.044065. Further permissions related to the material excerpted should be directed to the APS.

Both the experimental work and the data analysis were performed by Kevin Namink, Dr. Sanli Faez, Dr. Marc Koper and myself. Specifically, the dark-field imaging and measurements of the potentiodynamic optical contrast (PDOC) on the ITO substrates, the PDOC signal analysis were performed by myself. The measurements of PDOC under variable surface potential, electric current and in different salt solutions was performed by Kevin Namink. The characterisation of surface electric double layer reconfiguration was performed both by Dr. Sanli Faez and Dr. Marc Koper.

5.1 Introduction

The storage and recovery of energy in batteries, solvation of molecules, filtration by membranes, and many transport processes in liquid environments

are dictated by the interaction of ions with charged surfaces and the formation of the electric double layer (EDL).[239] The EDL formed around charged nanostructures at the liquid-solid interface determines their electrochemical activity and influences their electrical and optical polarisability. The EDL consists of a layer of ions in solution that screens the surface charge at the interface, with a thickness from one to a few tens of nanometres dependent on the ionic strength of the solution. The formation of the EDL involves several time scales,[240] the fastest of which is the molecular diffusion timescale, D/λ_{D}^2, with D the diffusion constant and λ_{D} the Debye length, which is often used as a measure of the EDL thickness. The small volumes and short timescales associated with the formation of the EDL makes direct access to its local dynamics experimentally challenging. Previous experimental observations of the EDL on the nanoscale have been based on amperometric measurements with scanning probe methods,[241,242] nanopores,[243,244] or ultramicroelectrodes,[245,246] which require a current signal above the background thermal current fluctuations. Visualising the contrast of the EDL optically, on the other hand, probes the accumulated charge and provides direct access to spatial information of the ionic current. Optically studying the spatial ion accumulation and transport is an enabling approach, built on a distinct working principle, which combines the power of optical microscopy with electrochemical amperometric analysis.

Changes to the optical reflectivity from a homogeneous flat electrode in contact with an electrolyte as a function of its electric potential, referred to as electroreflectance, has been observed previously, and attributed to modulations of the optical properties of both the metal and electrolyte sides of the interface.[247,248] The connection between electroreflectance and the restructuring of the EDL has been postulated and tested for large flat surfaces using ellipsometry[249] but separating the changes caused by conduction electrodes in the

metallic layer to electromodulation from the contribution of electrolyte EDL has been challenging.[250,251] More recently, the influence of electrode potential on elastic light scattering (ELS) from plasmonic nanoparticles that exhibit a localised plasmon resonance[252–254] and for two-dimensional materials[255] has been detected. In those experiments, however, the signal from the EDL is often dwarfed by plasmonic and electronic effects caused by variation of the charge density inside the nano-object.

Here, we experimentally demonstrate that the change in the EDL composition can be directly visualised by measuring the ELS from any type of nanoparticle and even surface roughness on top of a capacitively charged surface. We refer to this intensity change in the ELS as the potentiodynamic optical contrast (PDOC). The temporal response of the PDOC is influenced mostly by the physical adsorption of counter-ions with different optical polarisability (related to bulk refractive index) compared to the solvent. We demonstrate this effect by quantifying the temporal relaxation of the PDOC, which is directly related to the charging time of the EDL. We also show that the magnitude of PDOC scales with optical polarisability. We observe that deposited nanoparticles from other materials, e.g., chromium, exhibit a different pattern than the underlying ITO substrate due to different electrochemical properties. This difference enables visualisation of small nanoparticles that otherwise cannot be differentiated from back- ground scattering. By accurately measuring the PDOC as a function of applied potential, we can perform the optical equivalent of cyclic voltametry, at attoampere current level, on a single nanoparticle.

5.2 Experimental methods

5.2.1 Dark-field scattering microscopy

To image such small changes in polarisability due to the reconfiguration of the EDL, we use a customized total internal reflection optical microscope. Similar to other interferometric-enhanced imaging techniques,[256,257] the static scattering from the nanoparticle acts as a reference for the homodyne detection of changes in the polarisability of the (sub-wavelength) particle surrounding. This signal is used here to visualise the EDL reconfiguration. It is essential that the reference intensity is kept stable with fluctuations smaller than the scattering contribution from the EDL. For our measurements the signal to reference ratio is on the order of 10^{-3} to 10^{-2}.

5.2.2 ITO substrate preparation

We perform PDOC measurements on nanoparticles or grown nanostructures on top of ITO-coated glass cover-slips (Diamond Coatings, 70 - 100 Ohms/Sq). As the counter-electrode we use a second ITO-coated acrylic sheet separated from the substrate using double-sided adhesive tape, forming a 100 μm thickness flow cell. This configuration enables liquid exchange inside the flow cell while investigating the same field of view of the substrate with different electrolyte solutions. Unless specified otherwise, the applied potentials have balanced triangle-shape waveforms and the scattering images are recorded at 200 frames per second.

5.2.3 Potentiodynamic optical contrast of the EDL

We first estimate the expected PDOC caused by the change in the ion concentrations inside the EDL as a function of the surface potential. We use a nanosphere with a uniformly charged surface as a model system. Because we

are mainly interested in the ELS from the EDL, we only consider changes due to the reconfiguration of ions outside the particle. The optical contrast of the EDL can be used to study dielectric particles, semiconductor nanocrystals, and metallic scatterers with plasmon resonance frequencies far from the visible range.

Because the EDL is much thinner than the wavelength of the incident light, the details of the charge distribution inside the EDL has a negligible influence on the ELS intensity. Therefore we consider the screening ions to be uniformly distributed in a layer of thickness $\lambda_{\mathrm{S}} \ll a$, with a a the nanosphere radius. This model matches the physical conditions for surface potentials much larger than the characteristic potential $k_{\mathrm{B}}T/e \approx 25$ mV, in which charge screening is mostly due to the Stern layer. The total number of excess counter-ions, N, necessary for screening the nanosphere at potential V is given by $(\frac{Ve}{k_{\mathrm{B}}T})(\frac{a}{\lambda_{\mathrm{B}}})$, with λ_{B} the Bjerrum length. In the Rayleigh scattering regime, the polarisability of the combined system of the nanosphere and the EDL is a volumetric sum of its constituents. Using the Rayleigh polarisability and the phenomenological relation between refractive index and salt concentration $n_{\mathrm{mix}} = n_{\mathrm{solvent}} + Kx_s$, with x_s the ratio between number density of salt ions and solvent molecules,[258] we arrive at the scaling result,

$$\frac{\alpha_{\mathrm{EDL}}}{\alpha_p} \simeq \frac{2K(m^2+2)}{n_w(m^2-1)} . \frac{\frac{Ve}{k_{\mathrm{B}}T}}{4\pi a^2 \lambda_{\mathrm{B}} \rho_w}, \tag{5.1}$$

with ρ_w the number density of water molecules (considering an aqueous solution) and m the ratio between refractive index of the particle and water. For a typical dielectric material ($m = 1.3$) and alkali-halide salts,[258] the prefactor is roughly 3. Using $\rho_w = 33\,\mathrm{nm}^{-3}$ and $\lambda_{\mathrm{B}} = 0.7$ nm for water, we arrive at $\alpha_{\mathrm{EDL}}/\alpha_{\mathrm{p}} \approx 0.015$ for a 10 nm (diameter) nanoparticle in a NaCl solution at a surface potential of $V = 1$ Volt.

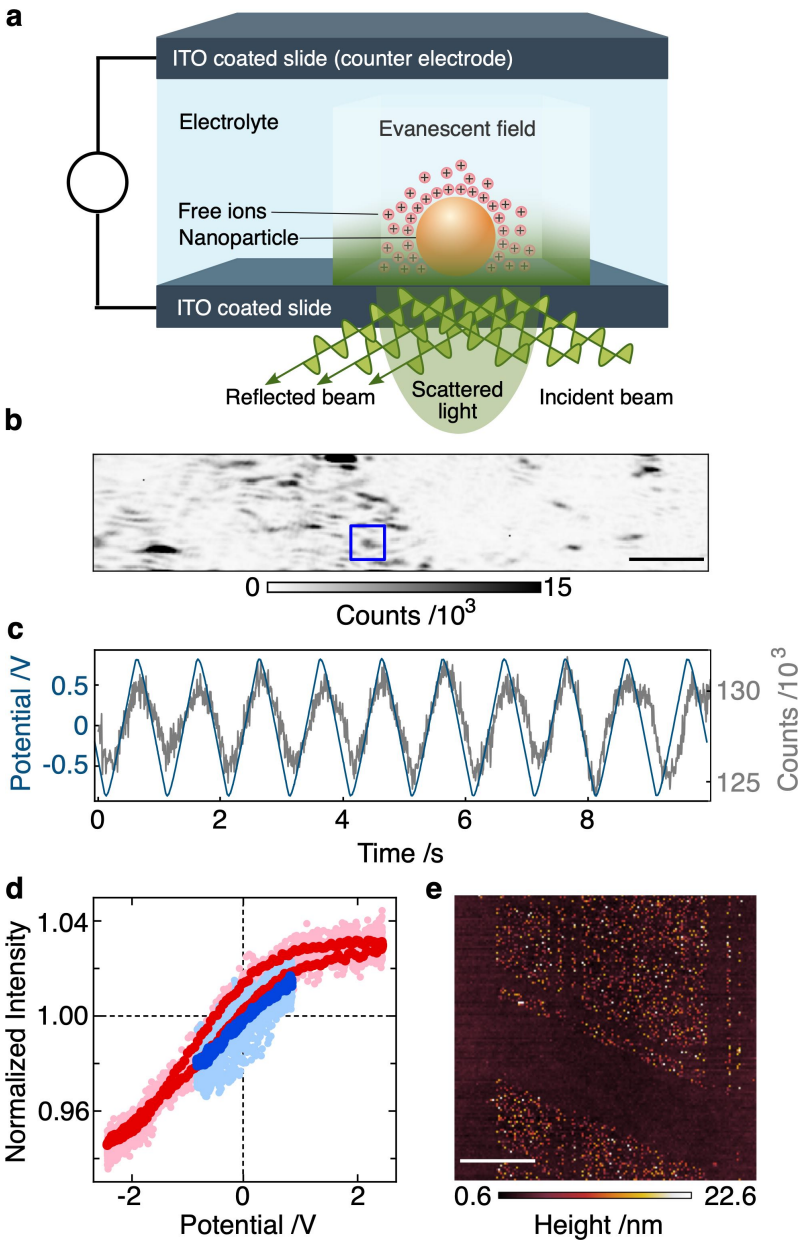


Figure 5.1: Measuring the potentiodynamic contrast of the EDL on a rough surface. (a) Setup for measuring the PDOC and the electrochemical cell configuration, (b) Typical scattering image from the ITO surface. Scale bar: 2 μm. (c) Scattering intensity from the grain annotated by an square in (b) plotted while changing the surface potential in a triangle waveform. (d) The normalized intensity change plotted as a function of the cell potential for 100 cycles (light symbols) and the average of all cycles after correction for drift (bold symbols) for two different sweeping amplitudes. (e) Atomic force microscope scan of the ITO surface. Scale bar: 4 μm.

5.3 Results and discussion

5.3.1 Surface topographic variations

In Figure 5.1, we present a typical scattering image of the surface of the ITO substrate. The ITO surface contains regions of high scattering intensity in the shape of parallelograms (see Figure 5.1b), with sharp edges and corners, in the middle of comparatively smoother regions of 10 to 100 times lower scattering signal. Using an atomic force microscope, we could detect the presence of sparse grains of roughly 20 nm height in geometrically recognisable areas (Figure 5.1e). The sharp boundaries confining these grains are indicative of the crystallographic origin for their formation, attributed to the stress release in the deposited layer during the annealing of ITO.[259,260] We can use the fairly homogeneous size distribution of these grains on the ITO rough regions, and straight boundaries of these regions to distinguish between ITO grains and other particles or contamination that resides on the surface. For the cell potentials and electrolyte solutions used here, the ITO surface has proven to be very stable and has shown no irreversible change for phosphate buffer at pH 7, when the cell potential is kept within ± 1.5 V.

5.3.2 Potentiodynamic optical contrast response to applied cell potential

Due to their electrochemicial stability, we can use the ITO nanograins as reference scatterers for measuring the EDL signal. We record the ELS while alternating the potential of the ITO substrate relative to the counter electrode. By subtracting the average scattering signal over an entire cycle from each frame we obtain the PDOC and simultaneously correct for any drift in background intensity. For some of the spots, these intensity oscillations are visible above the measurement noise, even for a single cycle, after correcting for the drift.

Figure 5.1b depicts the average dark-field scattering image of the ITO surface. The ELS intensity from a single speckle spot is plotted in Figure 5.1c as a function of the applied potential for ten cycles. For low cell potentials, the relation between contrast and substrate potential is close to linear at any instant, in agreement with the prediction for EDL restructuring. At higher potentials, however, we observe a nonlinear dependence and a phase lag between the PDOC and the applied potential (Figure 5.1d).

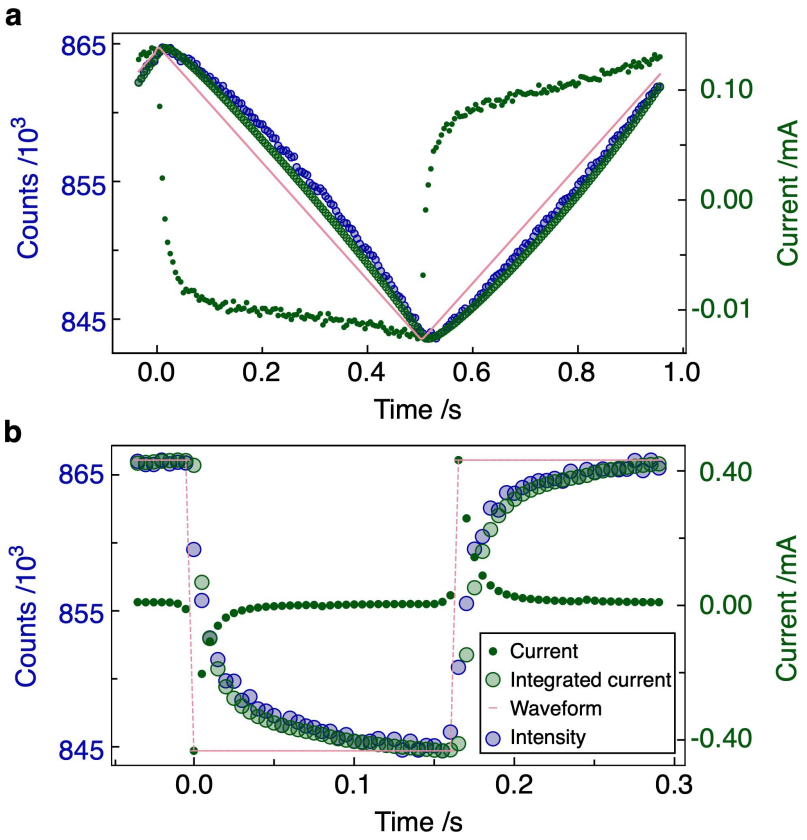


Figure 5.2: The optical signal from the electric double layer under variable surface potential. The measured electric current through the cell for an alternating voltage of (a) triangle and (b) square waveform between +1 and -1 V. In both (a) and (b) in green dots the measured current and in pink dots the applied potential. The integrated current (green circles), corresponding to the accumulate charge at the interface shows the same temporal behaviour as measured scattering intensity (blue circles, averaged value over several cycles). The exponential change of the current towards equilibrium corresponds to the charging time of the electrochemical cell.

5.3.3 Accumulated charge at the substrate

Next, we investigate the time dependence of the PDOC for a linear sweep and for a step reversal of the substrate potential, while simultaneously measuring the current passing through the cell. For a linear sweep, the electric current reaches a constant value after a certain relaxation time. The PDOC follows the potential with a lag that is comparable to that relaxation time and matches the charging time τ_c of the flow cell. This relaxation behaviour is more evident when applying a square potential, in which the current stops after τ_c, due to screening and the PDOC saturates. The saturation of the current for a linear potential sweep and relaxation to null for a step change in the potential both point towards the absence of Faradaic currents at the electrodes. To make a direct comparison, we plot the integrated electric current during the cycle, i.e., the accumulated charge, on top of the PDOC signal (Figure 5.2). We observe an almost perfect overlap that the PDOC is proportional to the accumulated charge at the substrate.

5.3.4 Ruling out the quasi-capacitance charging effect

While the above observations demonstrate the surface charging origin of the PDOC, they are insufficient to distinguish between reconfiguration of the EDL and the redox reactions at the surface of the ITO, also known as quasi-capacitance charging.[261] To differentiate between these two effects, we investigate the PDOC response on the same ITO grain for three different anions in the electrolyte solution. Typical responses are shown in Figure 5.3a, next to the simultaneously measured electric current passing through the cell. While the electric current is the same for the three ions, the PDOC in presence of NaI is almost twice that of NaCl and NaBr for the same cell potential. This observation can be explained by the optical polarisability of the iodide ions

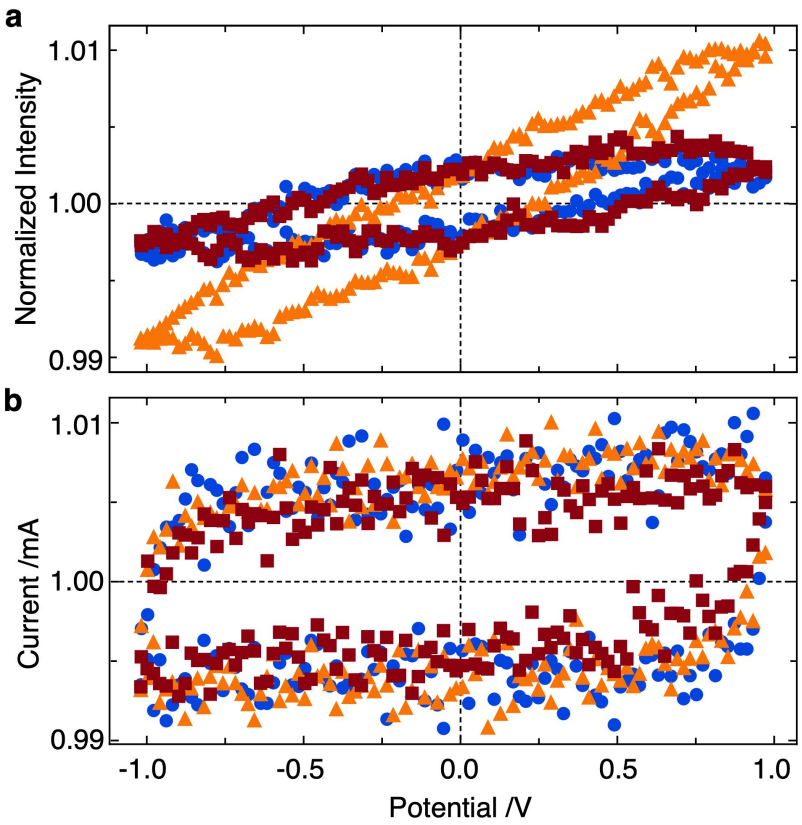


Figure 5.3: PDOC response on the ITO grain for three different anions in the electrolyte solution. (a) The average PDOC contrast for the same ITO grain for three different salts and (b) the electric cyclic voltagram of the ITO substrate of the same measurements as (a). The measured salts are NaCl (blue circles), NaBr (red squares), NaI (orange triangles).

relative to chloride and bromide. While the exact calculation of the change in the refractive index of the EDL would require an accurate consideration of ion hydration and is beyond the scope of this article, it has been shown empirically that the change in the refractive index is almost proportional to the atomic polarisability.[258] NaCl (α_{Cl} = 14.6, RI = 1.54), NaBr (α_{Br} = 21, , RI = 1.64), NaI (α_I = 32, , RI = 1.78).[261]

We also observe a difference in the temporal phase lag between in the PDOC response and the cell potential for the three electrolytes. This difference is also observed in the electrical measurements and can be attributed to the difference in surface absorption dynamics for the three ions. The I-V curves measured

simultaneously also exhibit this difference.

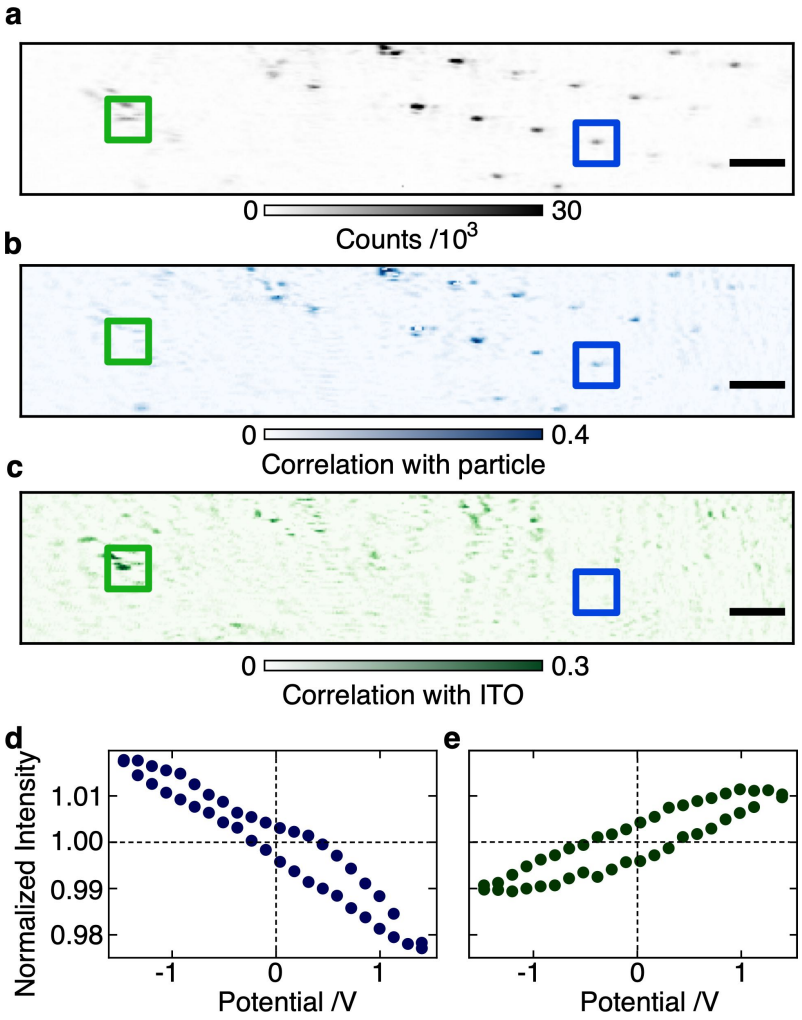


Figure 5.4: The elastic light scattering signal from chromium deposited on the ITO-coated slides through a SiN membrane (a) Dark-field scattering image of the ITO substrate after deposition of Chromium through a SiN stencil. Scale bar: 4 μm. The deposition locations are on a triangular lattice. Average covariance of each pixel intensity with the PDOC curve of (b) chromium and (c) ITO grain. The corresponding reference PDOC curves are depicted in (d) and (e).

5.3.5 Material-specificity of the EDL

We have shown, hitherto, that the PDOC obtained by dark-field ELS microscopy is an optical indicator of the optical polarisability of accumulated ions (charges) around ridges or grains on a flat substrate. Furthermore, we observe that both the temporal hysteresis behavior of the cyclic optical contrast depends

on the type of salt and the sweeping rate of the cell potential. As such, the PDOC of each grain can be viewed as a local nano-electroscope placed directly on the surface that can be used for studying the heterogeneity of surface interactions with the electrolyte, akin to conventional cyclic voltametry. While for electrochemically inert ITO, the EDL reconfiguration is the main source for changes to the scattering intensity, other material-specific surface reactions can influence the dynamics. As such, the PDOC can be seen as a novel, material specific contrast mechanism. To showcase this specificity, we deposit a few nanometres of chromium on the ITO-coated slides through a SiN membrane containing an array of micrometer-size holes, used as stencil. In Figure 5.4a we depict the raw scattering image. The ELS from chromium deposits is comparable in magnitude to the ITO grains in the rough regions. The chromium deposits can be identified from their geometrical arrangement on a triangular lattice, dictated by the stencil. The average PDOC over several cycles for one of chromium particles and one ITO grain are depicted in Figure 5.4d,e. This difference can be attributed to electro-oxidation of chromium atoms. We can identify all other positions on the surface that exhibit the same PDOC response by correlating each pixel in- tensity over time with the obtained reference. In Figure 5.4b,c. We depict the covariance of each pixel with the reference for all points that correlate positively with Cr and ITO references, correspondingly.

5.4 Conclusion and outlook

To conclude, we have spatially resolved the reconfiguration of EDL directly from changes to the optical contrast. At low potentials compared to the electrochemical reaction potential, using fully polarisable electrodes, the potentiodynamic scattering contrast is mostly due to the reconfiguration of the EDL. For higher

potentials, physisoprtion or Faradaic reactions start to dominate changes in the optical contrast of the surface surrounding. PDOC imaging can thus be used to measure the deposition or formation of products on the surface. In this range, the shape and magnitude of the response depend on the sweeping rate. Given that particles as small as 10 nm have been detected, the local current passing through this area for the slowest scan rates in our measurements is at the level of 10^{-18} A. By further studying the correspondence between different sweeping modes, PDOC imaging can build upon the vast knowledge obtained from electrochemical studies. This imaging technique provides important additional information such as spatial resolution, sensitivity to surface heterogeneity, local ions accumulation, and possibility of studying deposits, possibly down to single biomolecules. Another operation mode compatible with PDOC microscopy involves a substrate covered with a thin insulating layer. In this mode, the ion configuration at the EDL can be altered by capacitive coupling, and the Faradaic reaction will be completely excluded. This possibility will extend applications to a range of electrolytes that are chemically corrosive for ITO.

While we have chosen dark-field imaging for this work, the PDOC microscopy is fully compatible with interferometric scattering microscopy (iSCAT).[256,262] This method has already proven to be sufficiently sensitive for detecting and characterizing single proteins based on their polarisability.[263] The combination of this remarkable sensitivity with potentiodynamic control creates a previously untapped contrast mechanism for chemical specific optical microscopy of single nanoparticles and single macromolecules. This possibility paves the way to measuring chemical reactions such as oxidation and reduction processes on a single protein, or their reaction with antibodies, for an extended period of time.

Finally, the label-free imaging capabilities for detecting biological molecules

of TIRSM were not fully exploited given lack of a direct measurement with charged proteins such as DNA, bovine serum albumin (BSA) and actin filaments, and thus the limited control and knowledge over the phase lag of the PDOC that is dependent on charge characteristics of proteins. Future development of TIRSM in the field of label-free imaging will greatly benefit from a comprehensive experiment and characterisation of a variety of proteins with different charge characteristics and molecular weights. The applications are numerous from single molecule imaging to the quantification of equilibrium dynamics of protein complex as previously accomplished for mass photometry measurements.[263]

Chapter 6

Conclusion and outlook

6.1 Conclusion

The objective of this work was to improve the background suppression and signal to noise ratio of darkfield microscopes to enable high speed tracking of nanoparticles and to investigate the flexibility of double-stranded DNA at short length scales, below 150 base pairs, which is essential for understanding DNA-protein interactions. The study has further developed dsDNA tether construction as a molecular sensor to measure the electrophoretic force exerted on DNA tethers and detect changes in charge upon ligand bindings. Compared to alternative approaches, this has high throughput because TIRSM enables simultaneous readout of multiple sensors. Finally, based on our total internal reflection scattering darkfield microscope setup, we have demonstrated a new approach using the material-specificity of the electric double layer as a label-free contrast mechanism to visualise nanostructures with light scattering.

Summarised in chapter 2, the primary achievement of my work is the development of TIRSM capable of distinguishing small features from other background signatures in pursuit of significantly enhanced sensitivity. Taking advantage of the outstandingly high signal to noise ratio and unprecedented background suppression of total internal reflection illumination with the more universal scattering-based contrast mechanism, I have shown the potential of

TIRSM as a powerful tool for high speed single particle tracking with microsecond temporal resolution and nanometre localisation precision. Using pure scattering detection eliminates intrinsic photophysical limitations of fluorescent labels and pushes the boundary of temporal resolution down to 6 μs, which could in principle be further improved by using a faster detector.

Besides the instrumentation, in chapter 3, a straightforward surface passivation and single molecule tethering assay was developed to ensure that individual double-stranded DNA molecules are tethered to the glass surface specifically at one end (5') while the other end is bound to a single reporter bead, making it possible to address the question of DNA flexibility below commonly accepted persistence length scales ($\sim$150 bp), which previously had been an experimental challenge with the TPM method. I used 20 nm diameter gold nanoparticles as small reporter beads to study dynamics in regimes where the bead motion was dominated by diffusion of short DNA with negligible perturbations from volume exclusion effects. Finally, information about the mechanical properties of dsDNA molecules ranging from 60 to 160 base pairs was extracted from radial distribution functions of tethered particles. The results suggest that short lengths of dsDNA are more flexible than predicted by the WLC model, and the flexibility of dsDNA on short length scales is dependent on its contour length and the salt concentration in the buffer.

In addition to studying DNA flexibility, I further developed and utilised the dsDNA tether as a molecular force and charge sensor capable of detecting sub-piconewton change in force and addition/loss of a few hundred elementary charges with single-molecule statistics. By applying an alternating external electric field, stretched dsDNA functionalised with charged nanoparticles acts as a nanospring under forces on sub-piconewton scales. The deformation of DNA tethers was monitored by tracking tethered nanoparticles with simultaneous

nanometre spatial precision and microsecond temporal resolution. I calibrated the effective spring constant of each tether individually from the motion of the tethered bead, and characterised each force sensor by studying its response to the magnitude of the applied field and after binding of supercharged biomolecules to the nanoparticle surface. This technique can be applied to studying force and charge related dynamics and interactions of biological macromolecules.

Finally, we used ITO coated coverslips and noticed intensity fluctuations of the static surface background matching the frequency of the alternating voltage. Further investigations of the phenomenon revealed that the contrast change is caused by the restructuring of the electric double layer around the surface nanostructure. These results demonstrate the potential of TIRSM for label-free imaging. By measuring the temporally and spatially resolved scattering intensity with high sensitivity, we showed that the potentiodynamic optical contrast changes proportionally to the accumulated charge of polarisable ions at the interface and its time derivative represents a nanoscale ionic current. Finally, we used the material-specificity of the EDL as a label-free contrast mechanism to visualise surface nanostructures with light scattering and performed spatially-resolved optical cyclic voltammetry on deposited chromium nanoparticles at an ion current density of a few attoamperes, corresponding to the exchange of only a few hundred ions. The potentiodynamic contrast mechanism, together with the remarkable sensitivity of TIRSM, opens up the possibility of optical studies of chemical kinetics and heterogeneities in redox potentials of single nanoparticles.

6.2 Outlook

While I have presented a TPM experiment using 20 nm diameter gold nanoparticles as reporter beads to study the flexibility of short DNA ($\leq$ 160 bp) in a regime where volume exclusion is not at play. Using even smaller reporter beads remains, however, the ultimate goal, since the influence of the label on the molecular properties being measured remains unclear. For TIRSM, the boundaries for imaging and tracking small particles are the detection sensitivity and the ability to distinguish objects from the background. According to the theory of detection based on pure scattering as has been discussed in chapter 2, the sensitivity is limited by the number of detected photons from weak scatters, and thereby pushing the boundaries for this is probably more feasible by removing background signatures. When visualising a small nanoparticle on a microscope coverslip, static background arises from the surface nanostructure which becomes increasingly visible when detecting the weakest scatters. In principle, specifically for gold nanoparticles, a 10 nm and maybe even smaller ($<$ 5 nm) single particle can be distinguished from the background[264] by taking advantage of plasmon resonance enhanced scattering at $\sim$520 nm illumination wavelength. To achieve this, illuminating with alternating pulses of 520 nm light (on resonance) and an off-resonance wavelength would result in signal fluctuations from the gold nanoparticle while a relatively constant background from the scattering of glass roughness. Subtracting the non-resonant scattering in this way would provide higher specificity for gold nanoparticles, enabling the determination of the centre of mass of smaller such nanoparticles than have been used here. In addition to this, future experiments would benefit from three-dimensional imaging to enhance the axial resolution after calibration.[265] For example in TPM experiments, because of the exponentially decayed evanescent field, correlations between the scattering amplitude and particle

displacements in z could be employed to validate properly formed DNA tethers from their malformed counterparts.

TIRSM is possibly one of the most powerful tool for single particle tracking applications which require both high temporal resolution and spatial precision, while it also has potential for label-free imaging as shown in chapter 5. In combination with PDOC, dark-field microscopy is given a second life with many potential applications in analytical science and surface detection. These may include measuring the formation of products on a surface, deposition of biomolecules, characterisation of surface topography and impurities in the 2D materials.[255] All in all, given the impressive spatiotemporal precision, together with the simplicity of the set-up, TIRSM is an exciting development that will surely find a welcome home in many labs, inspiring many interesting new applications.

References

[1] B. Alberts, A. Johnson, J. Lewis, D. Morgan, M. Raff, K. Roberts and P. Walter, in *Molecular Biology of the Cell*, ed. J. Wilson and T. Hunt, Garland Science, 6th edn., 2017, ch. 4.

[2] K. E. Van Holde, in *Chromatin*, ed. K. E. Van Holde, Springer New York, New York, NY, 1989, pp. 1–15.

[3] M. Thanbichler, S. C. Wang and L. Shapiro, The Bacterial Nucleoid: A Highly Organized and Dynamic Structure, *Journal of Cellular Biochemistry*, 2005, **96**, 506–521.

[4] J. E. Darnell, H. Lodish, A. Berk, L. Zipursky, P. Matsudaira and D. Baltimore, in *Molecular Cell Biology*, W.H.Freeman & Co Ltd, 4th edn., 2000, ch. 6.

[5] K. E. Van Holde, in *Chromatin*, ed. K. E. Van Holde, Springer New York, New York, NY, 1989, pp. 355–408.

[6] R. D. Kornberg and Y. Lorch, Twenty-five Years of the Nucleosome, Fundamental Particle of the Eukaryote Chromosome, *Cell*, 1999, **98**, 285–294.

[7] W. Saenger, in *Principles of Nucleic Acid Structure*, Springer, New York, NY, New York, 1984, ch. 5, pp. 105–115.

[8] J. D. Watson and F. H. C. Crick, Molecular Structure of Nucleic Acids: A Structure for Deoxyribose Nucleic Acid, *Nature*, 1953, **171**, 737–738.

[9] R. Dahm, Discovering DNA: Friedrich Miescher and the early years of nucleic acid research, *Human Genetics*, 2008, **122**, 565–581.

[10] M. E. Jones, Albrecht Kossel, a Biographical Sketch, *The Yale journal of biology and medicine*, 1953, **26**, 80–97.

[11] P. A. Levene and W. A. Jacobs, Über Inosinsäure, *Berichte der deutschen chemischen Gesellschaft*, 1909, **42**, 1198–1203.

[12] P. A. Levene and W. A. Jacobs, Über die Pentose in den Nucleinsäuren, *Berichte der deutschen chemischen Gesellschaft*, 1909, **42**, 3247–3251.

[13] P. A. Levene, The Structure of Yeast Nucleic Acid, *Journal of Biological Chemistry*, 1919, **40**, 415–424.

[14] E. Chargaff, S. Zamenhof and C. Green, Human Desoxypentose Nucleic Acid: Composition of Human Desoxypentose Nucleic Acid, *Nature*, 1950, **165**, 756–757.

[15] E. Vischer and E. Chargaff, The Composition of the Pentose Nucleic Acids of Yeast and Pancreas, *Journal of Biological Chemistry*, 1948, **176**, 715–734.

[16] E. Chargaff and E. Vischer, The Composition of the Desoxypentose Nucleic Acids of Thymus and Spleen., *The Journal of biological chemistry*, 1949, **177**, 405–416.

[17] E. Vischer, S. Zamenhof and E. Chargaff, Microbial Nucleic Acids; the Desoxypentose Nucleic Acids of Avian Tubercle Bacilli and Yeast., *The Journal of biological chemistry*, 1949, **177**, 429–38.

[18] E. Chargaff, Chemical Specificity of Nucleic Acids and Mechanism of their Enzymatic Degradation, *Experientia*, 1950, **6**, 201–209.

[19] O. T. Avery, C. M. MacLeod and M. McCarty, Studies on the Chemical Nature of the Substance Inducing Transformation of Pneumococcal Types: Induction of Transformation by a Desoxyribonucleic Acid Fraction Isolated from Pneumococcus Type III, *Journal of Experimental Medicine*, 1944, **79**, 137–158.

[20] R. E. Franklin and R. G. Gosling, The Structure of Sodium Thymonucleate Fibres. I. The Influence of Water Content, *Acta Crystallographica*, 1953, **6**, 673–677.

[21] P. Yakovchuk, E. Protozanova and M. D. Frank-Kamenetskii, Base-stacking and Base-pairing Contributions into Thermal Stability of the DNA Double Helix, *Nucleic Acids Research*, 2006, **34**, 564–574.

[22] S. J. Benkovic, A. M. Valentine and F. Salinas, Replisome-Mediated DNA Replication, *Annual Review of Biochemistry*, 2001, **70**, 181–208.

[23] H. Yin, M. D. Wang, K. Svoboda, R. Landick, S. M. Block and J. Gelles, Transcription against an Applied Force, *Science*, 1995, **270**, 1653–1657.

[24] M. R. Bernfield and M. W. Nirenberg, RNA Codewords and Protein Synthesis, *Science*, 1965, **147**, 479–484.

[25] O. W. Jones and M. W. Nirenberg, Degeneracy in the Amino Acid Code, *Biochimica et Biophysica Acta - Nucleic Acids and Protein Synthesis*, 1966, **119**, 400–406.

[26] D. A. Kellogg, B. P. Doctor, J. E. Loebel and M. W. Nirenberg, RNA Codons and Protein Synthesis. IX. Synonym Codon Recognition by Multiple Species of Valine-, Alanine-, and Methionine-sRNA, *Proceedings of the National Academy of Sciences*, 1966, **55**, 912–919.

[27] F. Sanger, S. Nicklen and A. R. Coulson, DNA Sequencing with Chain-terminating Inhibitors, *Proceedings of the National Academy of Sciences*, 1977, **74**, 5463–5467.

[28] S. Anderson *et al.*, Sequence and Organization of the Human Mitochondrial Genome, *Nature*, 1981, **290**, 457–465.

[29] N. C. Seeman, Nucleic Acid Junctions and Lattices, *Journal of Theoretical Biology*, 1982, **99**, 237–247.

[30] P. W. K. Rothemund, Folding DNA to Create Nanoscale Shapes and Patterns, *Nature*, 2006, **440**, 297–302.

[31] P. C. Nickels, B. Wünsch, P. Holzmeister, W. Bae, L. M. Kneer, D. Grohmann, P. Tinnefeld and T. Liedl, Molecular Force Spectroscopy with a DNA Origami-based Nanoscopic Force Clamp, *Science*, 2016, **354**, 305–307.

[32] M. Gellert, DNA Topoisomerases, *Annual Review of Biochemistry*, 1981, **50**, 879–910.

[33] E. C. C. Lin, A. S. Lynch, J. C. Wang and A. S. Lynch, in *Regulation of Gene Expression in Escherichia coli*, Springer US, Boston, MA, 1996, pp. 127–147.

[34] J. Ma and M. D. Wang, DNA Supercoiling during Transcription, *Biophysical Reviews*, 2016, **8**, 75–87.

[35] S. Adhya, Multipartite Genetic Control Elements: Communication by DNA Loop, *Annual Review of Genetics*, 1989, **23**, 227–250.

[36] C. Moskaluk and D. Bastia, DNA Bending is Induced in an Enhancer by the DNA-binding Domain of the Bovine Papillomavirus E2 Protein, *Proceedings of the National Academy of Sciences*, 1988, **85**, 1826–1830.

[37] M. Horikoshi, C. Bertuccioli, R. Takada, J. Wang, T. Yamamoto and R. G. Roeder, Transcription Factor TFIID Induces DNA Bending upon Binding to the TATA Element, *Proceedings of the National Academy of Sciences*, 1992, **89**, 1060–1064.

[38] W. A. Rees, R. W. Keller, J. P. Vesenka, G. Yang and C. Bustamante, Evidence of DNA Bending in Transcription Complexes Imaged by Scanning Force Microscopy, *Science*, 1993, **260**, 1646–1649.

[39] P. Meysman, K. Marchal and K. Engelen, DNA Structural Properties in the Classification of Genomic Transcription Regulation Elements, *Bioinformatics and biology insights*, 2012, **6**, 155–168.

[40] H. S. Basu, B. G. Feuerstein, D. A. Zarling, R. H. Shaffer and L. J. Marton, Recognition of Z-RNA and Z-DNA Determinants by Polyamines in Solution: Experimental and Theoretical Studies, *Journal of Biomolecular Structure and Dynamics*, 1988, **6**, 299–309.

[41] R. E. Franklin and R. G. Gosling, Molecular Configuration in Sodium Thymonucleate, *Nature*, 1953, **171**, 740–741.

[42] A. H. J. Wang, G. J. Quigley, F. J. Kolpak, J. L. Crawford, J. H. van Boom, G. van der Marel and A. Rich, Molecular Structure of a Left-handed Double Helical DNA Fragment at Atomic Resolution, *Nature*, 1979, **282**, 680–686.

[43] R. E. Dickerson, in *DNA Structures Part A: Synthesis and Physical Analysis of DNA*, Academic Press, 1992, vol. 211, pp. 67–111.

[44] A. Ghosh and M. Bansal, A Glossary of DNA Structures from A to Z, *Acta Crystallographica Section D*, 2003, **59**, 620–626.

[45] A. G. W. Leslie, S. Arnott, R. Chandrasekaran and R. L. Ratliff, Polymorphism of DNA Double Helices, *Journal of Molecular Biology*, 1980, **143**, 49–72.

[46] Y. G. Kim, M. Muralinath, T. Brandt, M. Pearcy, K. Hauns, K. Lowenhaupt, B. L. Jacobs and A. Rich, A Role for Z-DNA Binding in Vaccinia Virus Pathogenesis, *Proceedings of the National Academy of Sciences*, 2003, **100**, 6974–6979.

[47] A. Rich and S. Zhang, Z-DNA: the Long Road to Biological Function, *Nature Reviews Genetics*, 2003, **4**, 566–572.

[48] Y. G. Kim, K. Lowenhaupt, D.-B. Oh, K. K. Kim and A. Rich, Evidence that Vaccinia Virulence Factor E3L Binds to Z-DNA in vivo: Implications for Development of a Therapy for Poxvirus Infection, *Proceedings of the National Academy of Sciences*, 2004, **101**, 1514–1518.

[49] M. L. Sipski and T. E. Wagner, Probing DNA Quaternary Ordering with Circular Dichroism Spectroscopy: Studies of Equine Sperm Chromosomal Fibers, *Biopolymers*, 1977, **16**, 573–582.

[50] S. G. Gregory *et al.*, The DNA Sequence and Biological Annotation of Human Chromosome 1, *Nature*, 2006, **441**, 315–321.

[51] R. D. Kornberg, Chromatin Structure: A Repeating Unit of Histones and DNA, *Science*, 1974, **184**, 868–871.

[52] K. E. Van Holde, in *Chromatin*, ed. K. E. Van Holde, Springer New York, New York, NY, 1989, pp. 69–180.

[53] K. Luger, A. W. Mäder, R. K. Richmond, D. F. Sargent and T. J. Richmond, Crystal Structure of the Nucleosome Core Particle at 2.8 Å Resolution, *Nature*, 1997, **389**, 251–260.

[54] Y. Lorch, J. W. LaPointe and R. D. Kornberg, Nucleosomes Inhibit the Initiation of Transcription but Allow Chain Elongation with the Displacement of Histones, *Cell*, 1987, **49**, 203–210.

[55] M. Han and M. Grunstein, Nucleosome Loss Activates Yeast Downstream Promoters in vivo, *Cell*, 1988, **55**, 1137–1145.

[56] A. L. Olins and D. E. Olins, Spheroid Chromatin Units (ν Bodies), *Science*, 1974, **183**, 330–332.

[57] D. S. Latchman, Transcription Factors: An Overview, *The International Journal of Biochemistry & Cell Biology*, 1997, **29**, 1305–1312.

[58] J. Widom, Role of DNA Sequence in Nucleosome Stability and Dynamics, *Quarterly Reviews of Biophysics*, 2001, **34**, 269–324.

[59] K. Rippe, P. H. von Hippel and J. Langowski, Action at a Distance: DNA-looping and Initiation of Transcription, *Trends in Biochemical Sciences*, 1995, **20**, 500–506.

[60] D. Shore, J. Langowski and R. L. Baldwin, DNA Flexibility Studied by Covalent Closure of Short Fragments into Circles, *Proceedings of the National Academy of Sciences*, 1981, **78**, 4833–4837.

[61] O. Kratky and G. Porod, Röntgenuntersuchung gelöster Fadenmoleküle, *Recueil des Travaux Chimiques des Pays-Bas*, 1949, **68**, 1106–1122.

[62] M. Rubinstein and R. H. Colby, in *Polymer Physics*, Oxford University Press, 2003, ch. 2, pp. 49–96.

[63] J. L. Barrat and J. F. Joanny, Persistence Length of Polyelectrolyte Chains, *Europhysics Letters*, 1993, **24**, 333–338.

[64] B. Y. Ha and D. Thirumalai, Electrostatic Persistence Length of a Polyelectrolyte Chain, *Macromolecules*, 1995, **28**, 577–581.

[65] M. Le Bret, Electrostatic Contribution to the Persistence Length of a Polyelectrolyte, *The Journal of Chemical Physics*, 1982, **76**, 6243–6255.

[66] J. R. Wenner, M. C. Williams, I. Rouzina and V. A. Bloomfield, Salt Dependence of the Elasticity and Overstretching Transition of Single DNA Molecules, *Biophysical Journal*, 2002, **82**, 3160–3169.

[67] C. G. Baumann, S. B. Smith, V. A. Bloomfield and C. Bustamante, Ionic effects on the elasticity of single DNA molecules, *Proceedings of the National Academy of Sciences*, 1997, **94**, 6185–6190.

[68] C. Bustamante, S. B. Smith, J. Liphardt and D. Smith, Single-molecule Studies of DNA Mechanics, *Current Opinion in Structural Biology*, 2000, **10**, 279–285.

[69] C. Bustamante, Z. Bryant and S. B. Smith, Ten Years of Tension: Single-molecule DNA Mechanics, *Nature*, 2003, **421**, 423–427.

[70] P. J. Hagerman, Flexibility of DNA, *Annual Review of Biophysics and Biophysical Chemistry*, 1988, **17**, 265–286.

[71] T. E. Cloutier and J. Widom, Spontaneous Sharp Bending of Double-stranded DNA, *Molecular Cell*, 2004, **14**, 355–362.

[72] R. Vafabakhsh and T. Ha, Extreme Bendability of DNA Less than 100 Base Pairs Long Revealed by Single-Molecule Cyclization, *Science*, 2012, **337**, 1097–1101.

[73] S. B. Smith, L. Finzi and C. Bustamante, Direct Mechanical Measurements of the Elasticity of Single DNA Molecules by using Magnetic Beads, *Science*, 1992, **258**, 1122–1126.

[74] T. Perkins, D. Smith and S. Chu, Direct Observation of Tube-like Motion of a Single Polymer Chain, *Science*, 1994, **264**, 819–822.

[75] T. Perkins, D. Smith, R. Larson and S. Chu, Stretching of a Single Tethered Polymer in a Uniform Flow, *Science*, 1995, **268**, 83–87.

[76] S. B. Smith, Y. Cui and C. Bustamante, Overstretching B-DNA: The Elastic Response of Individual Double-stranded and Single-stranded DNA Molecules, *Science*, 1996, **271**, 795–799.

[77] P. Cluzel, A. Lebrun, C. Heller, R. Lavery, J. L. Viovy, D. Chatenay and F. O. Caron, DNA: An Extensible Molecule, *Science*, 1996, **271**, 792–794.

[78] M. D. Wang, H. Yin, R. Landick, J. Gelles and S. M. Block, Stretching DNA with Optical Tweezers, *Biophysical Journal*, 1997, **72**, 1335–1346.

[79] G. Binnig, C. F. Quate and C. Gerber, Atomic Force Microscope, *Physical Review Letters*, 1986, **56**, 930–933.

[80] P. Wiggins, T. V. Der Heijden, F. Moreno-Herrero, A. Spakowitz, R. Phillips, J. Widom, C. Dekker and P. C. Nelson, High Flexibility of DNA on short Length Scales Probed by Atomic Force Microscopy, *Nature Nanotechnology*, 2006, **1**, 137–141.

[81] C. Gosse and V. Croquette, Magnetic Tweezers: Micromanipulation and Force Measurement at the Molecular Level, *Biophysical Journal*, 2002, **82**, 3314–3329.

[82] T. Ha, T. Enderle, D. F. Ogletree, D. S. Chemla, P. R. Selvin and S. Weiss, Probing the Interaction between Two Single Molecules: Fluorescence Resonance Energy Transfer between a Single Donor and a Single Acceptor., *Proceedings of the National Academy of Sciences*, 1996, **93**, 6264–6268.

[83] D. A. Schafer, J. Gelles, M. P. Sheetz and R. Landick, Transcription by Single Molecules of RNA Polymerase Observed by Light Microscopy, *Nature*, 1991, **352**, 444–448.

[84] B. Cappella and G. Dietler, Force-distance Curves by Atomic Force Microscopy, *Surface Science Reports*, 1999, **34**, 1–104.

[85] A. J. Katan, R. Vlijm, A. Lusser and C. Dekker, Dynamics of Nucleosomal Structures Measured by High-speed Atomic Force Microscopy, *Small*, 2015, **11**, 976–984.

[86] T. R. Strick, J. F. Allemand, D. Bensimon, A. Bensimon and V. Croquette, The Elasticity of a Single Supercoiled DNA Molecule, *Science*, 1996, **271**, 1835–1837.

[87] M. T. J. van Loenhout, M. V. de Grunt and C. Dekker, Dynamics of DNA Supercoils, *Science*, 2012, **338**, 94–97.

[88] A. Ashkin, Acceleration and Trapping of Particles by Radiation Pressure, *Physical Review Letters*, 1970, **24**, 156–159.

[89] A. Ashkin, J. M. Dziedzic, J. E. Bjorkholm and S. Chu, Observation of a Single-beam Gradient Force Optical Trap for Dielectric Particles, *Optics Letters*, 1986, **11**, 288–290.

[90] K. C. Neuman and A. Nagy, Single-molecule Force Spectroscopy: Optical Tweezers, Magnetic Tweezers and Atomic Force Microscopy, *Nature Methods*, 2008, **5**, 491–505.

[91] K. Halvorsen and W. P. Wong, Massively Parallel Single-Molecule Manipulation Using Centrifugal Force, *Biophysical Journal*, 2010, **98**, 53–55.

[92] I. De Vlaminck *et al.*, Highly Parallel Magnetic Tweezers by Targeted DNA Tethering, *Nano Letters*, 2011, **11**, 5489–5493.

[93] N. Ribeck and O. A. Saleh, Multiplexed Single-molecule Measurements with Magnetic Tweezers, *Review of Scientific Instruments*, 2008, **79**, 094301.

[94] R. Roy, S. Hohng and T. Ha, A Practical Guide to Single-molecule FRET, *Nature Methods*, 2008, **5**, 507–516.

[95] A. A. Deniz, M. Dahan, J. R. Grunwell, T. Ha, A. E. Faulhaber, D. S. Chemla, S. Weiss and P. G. Schultz, Single-pair Fluorescence Resonance Energy Transfer on Freely Diffusing Molecules: Observation of Forster Distance Dependence and Subpopulations, *Proceedings of the National Academy of Sciences*, 1999, **96**, 3670–3675.

[96] X. Zhuang, L. E. Bartley, H. P. Babcock, R. Russell, T. Ha, D. Herschlag and S. Chu, A Single-molecule Study of RNA Catalysis and Folding, *Science*, 2000, **288**, 2048–2051.

[97] S. A. McKinney, A. C. Déclais, D. M. Lilley and T. Ha, Structural Dynamics of Individual Holliday Junctions, *Nature Structural Biology*, 2003, **10**, 93–97.

[98] M. C. Murphy, I. Rasnik, W. Cheng, T. M. Lohman and T. Ha, Probing Single-stranded DNA Conformational Flexibility using Fluorescence Spectroscopy, *Biophysical journal*, 2004, **86**, 2530–2537.

[99] M. Manghi, C. Tardin, J. Baglio, P. Rousseau, L. Salomé and N. Destainville, Probing DNA Conformational Changes with High Temporal Resolution by Tethered Particle Motion, *Physical Biology*, 2010, **7**, 046003.

[100] S. Brinkers, H. R. Dietrich, F. H. De Groote, I. T. Young and B. Rieger, The Persistence Length of Double Stranded DNA Determined using Dark Field Tethered Particle Motion, *Journal of Chemical Physics*, 2009, **130**, 215105.

[101] S. Dixit, M. Singh Zocchi, J. Hanne and G. Zocchi, Mechanics of Binding of a Single Integration-host-factor Protein to DNA, *Physical Review Letters*, 2005, **94**, 118101.

[102] P. C. Nelson, C. Zurla, D. Brogioli, J. F. Beausang, L. Finzi and D. Dunlap, Tethered Particle Motion as a Diagnostic of DNA Tether Length, *Journal of Physical Chemistry B*, 2006, **110**, 17260–17267.

[103] D. T. Kovari, Y. Yan, L. Finzi and D. Dunlap, in *Methods in Molecular Biology*, NIH Public Access, 2018, vol. 1665, ch. 17, pp. 317–340.

[104] D. E. Segall, P. C. Nelson and R. Phillips, Volume-exclusion Effects in Tethered-particle Experiments: Bead Size Matters, *Physical Review Letters*, 2006, **96**, 088306.

[105] M. Lindner, G. Nir, S. Medalion, H. R. C. Dietrich, Y. Rabin and Y. Garini, Force-free Measurements of the Conformations of DNA Molecules Tethered to a Wall, *Physical Review E*, 2011, **83**, 011916.

[106] E. F. Casassa, Modern Theory of Polymer Solutions, *Journal of Polymer Science Part B: Polymer Letters*, 1972, **10**, 69–73.

[107] H. Ueno, S. Nishikawa, R. Iino, K. V. Tabata, S. Sakakihara, T. Yanagida and H. Noji, Simple Dark-field Microscopy with Nanometer Spatial Precision and Microsecond Temporal Resolution, *Biophysical Journal*, 2010, **98**, 2014–2023.

[108] C. Joo, H. Balci, Y. Ishitsuka, C. Buranachai and T. Ha, Advances in Single-Molecule Fluorescence Methods for Molecular Biology, *Annual Review of Biochemistry*, 2008, **77**, 51–76.

[109] M. J. Saxton and K. Jacobson, Single-particle Tracking: Applications to Membrane Dynamics., *Annual review of biophysics and biomolecular structure*, 1997, **26**, 373–399.

[110] D. Axelrod, T. P. Burghardt and N. L. Thompson, Total Internal Reflection Fluorescence, *Annual review of biophysics and bioengineering*, 1984, **13**, 247–268.

[111] E. Betzig, J. K. Trautman, T. D. Harris, J. S. Weiner and R. L. Kostelak, Breaking the Diffraction Barrier: Optical Microscopy on a Nanometric Scale, *Science*, 1991, **251**, 1468–1470.

[112] S. W. Hell and J. Wichmann, Breaking the Diffraction Resolution Limit by Stimulated Emission: Stimulated-Emission-depletion Fluorescence Microscopy, *Optics Letters*, 1994, **19**, 780–782.

[113] E. Betzig *et al.*, Imaging Intracellular Fluorescent Proteins at Nanometer Resolution, *Science*, 2006, **313**, 1642–1645.

[114] S. W. Hell, Far-Field Optical Nanoscopy, *Science*, 2007, **316**, 1153–1158.

[115] M. Minsky, *US Patent# 3013467*, 1957.

[116] T. Wilson and C. Sheppard, in *Theory and Practice of Scanning Optical Microscopy*, Academic Press London, 1984, vol. 180, ch. 3, pp. 37–78.

[117] J. W. Lichtman, W. J. Sunderland and R. S. Wilkinson, High-resolution Imaging of Synaptic Structure with a Simple Confocal Microscope, *The New biologist*, 1989, **1**, 75–82.

[118] E. J. Ambrose, A Surface Contact Microscope for the study of Cell Movements, *Nature*, 1956, **178**, 1194.

[119] D. Axelrod, Cell-substrate Contacts Illuminated by Total Internal Reflection Fluorescence., *Journal of Cell Biology*, 1981, **89**, 141–145.

[120] D. Axelrod, in *Fluorescence Microscopy of Living Cells in Culture Part B. Quantitative Fluorescence Microscopy-Imaging and Spectroscopy*, ed. D. L. Taylor and Y. L. Wang, Academic Press, 1989, vol. 30, pp. 245–270.

[121] D. B. T. Axelrod, in *Biophotonics, Part B*, Academic Press, 2003, vol. 361, pp. 1–33.

[122] D. B. T. Axelrod, in *Biophysical Tools for Biologists, Volume Two: In Vivo Techniques*, Academic Press, 2008, vol. 89, pp. 169–221.

[123] A. L. Mattheyses, S. M. Simon and J. Z. Rappoport, Imaging with Total Internal Reflection Fluorescence Microscopy for the Cell Biologist, *Journal of Cell Science*, 2010, **123**, 3621–3628.

[124] J. Z. Rappoport and S. M. Simon, Real-time Analysis of Clathrin-mediated Endocytosis during Cell Migration, *Journal of Cell Science*, 2003, **116**, 847–855.

[125] J. Z. Rappoport, A. Benmerah and S. M. Simon, Analysis of the AP-2 Adaptor Complex and Cargo During Clathrin-Mediated Endocytosis, *Traffic*, 2005, **6**, 539–547.

[126] C. J. Merrifield, M. E. Feldman, L. Wan and W. Almers, Imaging Actin and Dynamin Recruitment during Invagination of Single Clathrin-coated Pits, *Nature Cell Biology*, 2002, **4**, 691–698.

[127] C. J. Merrifield, D. Perrais and D. Zenisek, Coupling between Clathrin-Coated-Pit Invagination, Cortactin Recruitment, and Membrane Scission Observed in Live Cells, *Cell*, 2005, **121**, 593–606.

[128] M. Fix, T. J. Melia, J. K. Jaiswal, J. Z. Rappoport, D. You, T. H. Söllner, J. E. Rothman and S. M. Simon, Imaging Single Membrane Fusion Events Mediated by SNARE Proteins, *Proceedings of the National Academy of Sciences*, 2004, **101**, 7311–7316.

[129] I. Akopova, S. Tatur, M. Grygorczyk, R. Luchowski, I. Gryczynski, Z. Gryczynski, J. Borejdo and R. Grygorczyk, Imaging Exocytosis of ATP-containing Vesicles with TIRF Microscopy in Lung Epithelial A549 Cells, *Purinergic Signalling*, 2012, **8**, 59–70.

[130] I. Grigoriev *et al.*, Rab6 Regulates Transport and Targeting of Exocytotic Carriers, *Developmental Cell*, 2007, **13**, 305–314.

[131] M. E. Berginski, E. A. Vitriol, K. M. Hahn and S. M. Gomez, High-Resolution Quantification of Focal Adhesion Spatiotemporal Dynamics in Living Cells, *PLOS ONE*, 2011, **6**, e22025.

[132] M. A. Partridge and E. E. Marcantonio, Initiation of Attachment and Generation of Mature Focal Adhesions by Integrin-containing Filopodia in Cell Spreading, *Molecular Biology of the Cell*, 2006, **17**, 4237–4248.

[133] S. J. Fletcher, N. S. Poulter, E. J. Haining and J. Z. Rappoport, Clathrin-mediated Endocytosis Regulates Occludin, and not Focal Adhesion, Distribution during Epithelial Wound Healing, *Biology of the Cell*, 2012, **104**, 238–256.

[134] F. E. Lock, K. R. Ryan, N. S. Poulter, M. Parsons and N. A. Hotchin, Differential Regulation of Adhesion Complex Turnover by ROCK1 and ROCK2, *PLOS ONE*, 2012, **7**, e31423.

[135] J. B. Manneville, Use of TIRF Microscopy to Visualize Actin and Microtubules in Migrating Cells, *Methods in enzymology*, 2006, **406**, 520–532.

[136] R. L. Webb, O. Rozov, S. C. Watkins and B. M. McCartney, Using Total Internal Reflection Fluorescence (TIRF) Microscopy to Visualize Cortical Actin and Microtubules in the Drosophila Syncytial Embryo, *Developmental Dynamics*, 2009, **238**, 2622–2632.

[137] R. Dixit and J. L. Ross, in *Microtubules, in vitro*, ed. L. Wilson and J. J. B. T. Correia, Academic Press, 2010, vol. 95, pp. 543–554.

[138] M. Gardner, B. Charlebois, I. Jánosi, J. Howard, A. Hunt and D. Odde, Rapid Microtubule Self-Assembly Kinetics, *Cell*, 2011, **146**, 582–592.

[139] M. Born and E. Wolf, in *Principles of Optics: Electromagnetic Theory of Propagation, Interference and Diffraction of Light*, Elsevier, 6th edn., 2013, ch. 11, pp. 556–591.

[140] T. Schmidt, G. J. Schuetz, W. Baumgartner, H. J. Gruber and H. Schindler, Characterization of Photophysics and Mobility of Single Molecules in a Fluid Lipid Membrane, *The Journal of Physical Chemistry*, 1995, **99**, 17662–17668.

[141] N. L. Thompson and J. K. Pero, in *Fluorescence Spectroscopy in Biology*, Springer-Verlag, Berlin/Heidelberg, 2005, pp. 79–103.

[142] W. E. Moerner and D. P. Fromm, Methods of Single-molecule Fluorescence Spectroscopy and Microscopy, *Review of Scientific Instruments*, 2003, **74**, 3597–3619.

[143] J. Ortega Arroyo, J. Andrecka, K. M. Spillane, N. Billington, Y. Takagi, J. R. Sellers and P. Kukura, Label-Free, All-Optical Detection, Imaging, and Tracking of a Single Protein, *Nano Letters*, 2014, **14**, 2065–2070.

[144] J. Ortega-Arroyo and P. Kukura, Interferometric Scattering Microscopy (iSCAT): New Frontiers in Ultrafast and Ultrasensitive Optical Microscopy, *Physical Chemistry Chemical Physics*, 2012, **14**, 15625–15636.

[145] J. Ortega Arroyo, D. Cole and P. Kukura, Interferometric Scattering Microscopy and its Combination with Single-molecule Fluorescence Imaging, *Nature Protocols*, 2016, **11**, 617–633.

[146] J. Andrecka, J. Ortega Arroyo, K. Lewis, R. Cross and P. Kukura, Label-free Imaging of Microtubules with Sub-nm Precision Using Interferometric Scattering Microscopy, *Biophysical Journal*, 2016, **110**, 214–217.

[147] G. de Wit, J. S. H. Danial, P. Kukura and M. I. Wallace, Dynamic Label-free Imaging of Lipid Nanodomains, *Proceedings of the National Academy of Sciences*, 2015, **112**, 12299–12303.

[148] A. Wax and K. Sokolov, Molecular Imaging and Darkfield Microspectroscopy of Live Cells using Gold Plasmonic nNanoparticles, *Laser & Photonics Review*, 2009, **3**, 146–158.

[149] E. Ringe, B. Sharma, A. I. Henry, L. D. Marks and R. P. Van Duyne, Single Nanoparticle Plasmonics, *Physical Chemistry Chemical Physics*, 2013, **15**, 4110–4129.

[150] J. D. Jackson, in *Classical Electrodynamics*, John Wiley & Sons, 2nd edn., 1975, ch. 6, pp. 209–261.

[151] M. Milosevic, in *Internal reflection and ATR spectroscopy*, John Wiley & Sons, 2012, vol. 176, ch. 5, pp. 55–60.

[152] M. Born *et al.*, in *Principles of Optics*, Cambridge University Press, Cambridge, 7th edn., 1999, ch. 1, pp. 1–70.

[153] M. Milosevic, On the Nature of the Evanescent Wave, *Applied Spectroscopy*, 2013, **67**, 126–131.

[154] H. He and J. Ren, A Novel Evanescent Wave Scattering Imaging Method for Single Gold Particle Tracking in Solution and on Cell Membrane, *Talanta*, 2008, **77**, 166–171.

[155] S. Enoki *et al.*, Label-Free Single-Particle Imaging of the Influenza Virus by Objective-Type Total Internal Reflection Dark-Field Microscopy, *PLoS ONE*, 2012, **7**, e49208.

[156] J. Andrecka *et al.*, Structural Dynamics of Myosin 5 during Processive Motion Revealed by Interferometric Scattering Microscopy, *eLife*, 2015, **2015**, e05413.

[157] D. S. Martin, M. B. Forstner and J. A. Käs, Apparent Subdiffusion Inherent to Single Particle Tracking, *Biophysical Journal*, 2002, **83**, 2109–2117.

[158] W. P. Wong and K. Halvorsen, The Effect of Integration Time on Fluctuation Measurements: Calibrating an Optical Trap in the Presence of Motion Blur, *Optics Express*, 2006, **14**, 12517–12531.

[159] T. Savin and P. S. Doyle, Static and Dynamic Errors in Particle Tracking Microrheology, *Biophysical Journal*, 2005, **88**, 623–638.

[160] T. Savin, P. T. Spicer and P. S. Doyle, A Rational Approach to Noise Discrimination in Video Microscopy Particle Tracking, *Applied Physics Letters*, 2008, **93**, 024102.

[161] A. S. Hansen, M. Woringer, J. B. Grimm, L. D. Lavis, R. Tjian and X. Darzacq, Robust Model-based Analysis of Single-particle Tracking Experiments with Spot-on, *eLife*, 2018, **7**, e33125.

[162] M. J. Bogdan and T. Savin, Errors in Energy Landscapes Measured with Particle Tracking, *Biophysical Journal*, 2018, **115**, 139–149.

[163] N. Mojarad and M. Krishnan, Measuring the Size and Charge of Single Nanoscale Objects in Solution using an Electrostatic Fluidic Trap, *Nature Nanotechnology*, 2012, **7**, 448–452.

[164] J. Howard, in *Mechanics of Motor Proteins and the Cytoskeleton*, Sinauer associates Sunderland, MA, 2001, ch. 6, pp. 99–118.

[165] W. Lukosz and R. E. Kunz, Light Emission by Magnetic and Electric Dipoles close to a Plane Dielectric Interface. II. Radiation Patterns of Perpendicular Oriented Dipoles, *Journal of the Optical Society of America*, 1977, **67**, 1615–1619.

[166] K. G. Lee, X. W. Chen, H. Eghlidi, P. Kukura, R. Lettow, A. Renn, V. Sandoghdar and S. Götzinger, A Planar Dielectric Antenna for Directional Single-photon Emission and Near-unity Collection Efficiency, *Nature Photonics*, 2011, **5**, 166–169.

[167] R. E. Thompson, D. R. Larson and W. W. Webb, Precise Nanometer Localization Analysis for Individual Fluorescent Probes., *Biophysical journal*, 2002, **82**, 2775–2783.

[168] J. F. Beausang, C. Zurla, L. Finzi, L. Sullivan and P. C. Nelson, Elementary Simulation of Tethered Brownian Motion, *American Journal of Physics*, 2007, **75**, 520–523.

[169] S. Blumberg, A. Gajraj, M. W. Pennington and J. C. Meiners, Three-dimensional Characterization of Tethered Microspheres by Total Internal Reflection Fluorescence Microscopy, *Biophysical Journal*, 2005, **89**, 1272–1281.

[170] A. W. C. Lau, A. Prasad and Z. Dogic, Condensation of Isolated Semi-flexible Filaments Driven by Depletion Interactions, *EPL (Europhysics Letters)*, 2009, **87**, 48006.

[171] S. Geggier and A. Vologodskii, Sequence Dependence of DNA Bending Rigidity, *Proceedings of the National Academy of Sciences*, 2010, **107**, 15421–15426.

[172] J. S. Mitchell, J. Glowacki, A. E. Grandchamp, R. S. Manning and J. H. Maddocks, Sequence-Dependent Persistence Lengths of DNA, *Journal of Chemical Theory and Computation*, 2017, **13**, 1539–1555.

[173] H. Shen, L. J. Tauzin, R. Baiyasi, W. Wang, N. Moringo, B. Shuang and C. F. Landes, Single Particle Tracking: From Theory to Biophysical Applications, *Chemical Reviews*, 2017, **117**, 7331–7376.

[174] R. Parthasarathy, Rapid, Accurate Particle Tracking by Calculation of Radial Symmetry Centers, *Nature Methods*, 2012, **9**, 724–726.

[175] T. E. Ouldridge, A. A. Louis and J. P. K. Doye, Structural, Mechanical, and Thermodynamic Properties of a Coarse-grained DNA Model, *The Journal of Chemical Physics*, 2011, **134**, 085101.

[176] K. E. Van Holde, *Chromatin*, Springer New York, New York, NY, 1989.

[177] T. Odijk, Polyelectrolytes near the Rod Limit, *Journal of Polymer Science: Polymer Physics Edition*, 1977, **15**, 477–483.

[178] M. Doi, S. F. Edwards and S. F. Edwards, *The theory of polymer dynamics*, Oxford University Press, 1986, vol. 73, p. 317.

[179] P. A. Wiggins, R. Phillips and P. C. Nelson, Exact Theory of Kinkable Elastic Polymers, *Physical Review E*, 2005, **71**, 021909.

[180] Q. Du, C. Smith, N. Shiffeldrim, M. Vologodskaia and A. Vologodskii, Cyclization of Short DNA Fragments and Bending Fluctuations of the Double Helix, *Proceedings of the National Academy of Sciences*, 2005, **102**, 5397–5402.

[181] D. F. R. Muris *et al.*, Cloning of Human and Mouse Genes Homologous to RAD52, a Yeast Gene involved in DNA Repair and Recombination, *Mutation Research/DNA Repair*, 1994, **315**, 295–305.

[182] K. Adzuma, T. Ogawa and H. Ogawa, Primary Structure of the RAD52 Gene in Saccharomyces Cerevisiae., *Molecular and Cellular Biology*, 1984, **4**, 2735–2744.

[183] E. V. Dyck, A. Z. Stasiak, A. Stasiak and S. C. West, Binding of Double-strand Breaks in DNA by Human RAD52 Protein, *Nature*, 1999, **398**, 728–731.

[184] E. Van Dyck, N. M. A. Hajibagheri, A. Stasiak and S. C. West, Visualisation of Human RAD52 Protein and its Complexes with hRAD51 and DNA, *Journal of Molecular Biology*, 1998, **284**, 1027–1038.

[185] A. Shinohara, M. Shinohara, T. Ohta, S. Matsuda and T. Ogawa, Rad52 Forms Ring Structures and Co-operates with RPA in Single-strand DNA Annealing, *Genes to Cells*, 1998, **3**, 145–156.

[186] U. H. Mortensen, C. Bendixen, I. Sunjevaric and R. Rothstein, DNA Strand Annealing is Promoted by the Yeast RAD52 Protein, *Proceedings of the National Academy of Sciences*, 1996, **93**, 10729–10734.

[187] P. Sung, Function of Yeast RAD52 Protein as a Mediator between Replication Protein A and the RAD51 Recombinase, *Journal of Biological Chemistry*, 1997, **272**, 28194–28197.

[188] A. Shinohara and T. Ogawa, Stimulation by RAD52 of Yeast RAD51-mediated Recombination, *Nature*, 1998, **391**, 404–407.

[189] J. H. New, T. Sugiyama, E. Zaitseva and S. C. Kowalczykowski, RAD52 Protein Stimulates DNA Strand Exchange by RAD51 and Replication Protein A, *Nature*, 1998, **391**, 407–410.

[190] F. E. Benson, P. Baumann and S. C. West, Synergistic Actions of RAD51 and RAD52 in Recombination and DNA Repair, *Nature*, 1998, **391**, 401–404.

[191] T. Sugiyama, J. H. New and S. C. Kowalczykowski, DNA Annealing by RAD52 Protein is Stimulated by Specific Interaction with the Complex of Replication Protein A and Single-stranded DNA, *Proceedings of the National Academy of Sciences*, 1998, **95**, 6049–6054.

[192] Z. Feng, S. P. Scott, W. Bussen, G. G. Sharma, G. Guo, T. K. Pandita and S. N. Powell, Rad52 Inactivation is Synthetically Lethal with BRCA2 Deficiency, *Proceedings of the National Academy of Sciences*, 2011, **108**, 686–691.

[193] R. Bhargava, D. O. Onyango and J. M. Stark, Regulation of Single-Strand Annealing and its Role in Genome Maintenance, *Trends in Genetics*, 2016, **32**, 566–575.

[194] J. M. Stark, A. J. Pierce, J. Oh, A. Pastink and M. Jasin, Genetic Steps of Mammalian Homologous Repair with Distinct Mutagenic Consequences, *Molecular and Cellular Biology*, 2004, **24**, 9305–9316.

[195] G. Reddy, E. I. Golub and C. M. Radding, Human RAD52 Protein Promotes Single-strand DNA Annealing followed by Branch Migration, *Mutation Research/Fundamental and Molecular Mechanisms of Mutagenesis*, 1997, **377**, 53–59.

[196] K. Kito, H. Wada, E. T. H. Yeh and T. Kamitani, Identification of Novel Isoforms of Human RAD52, *Biochimica et Biophysica Acta (BBA) - Gene Structure and Expression*, 1999, **1489**, 303–314.

[197] W. Kagawa, H. Kurumizaka, S. Ikawa, S. Yokoyama and T. Shibata, Homologous Pairing Promoted by the Human RAD52 Protein, *Journal of Biological Chemistry*, 2001, **276**, 35201–35208.

[198] W. Kagawa, A. Kagawa, K. Saito, S. Ikawa, T. Shibata, H. Kurumizaka and S. Yokoyama, Identification of a Second DNA Binding Site in the Human RAD52 Protein, *Journal of Biological Chemistry*, 2008, **283**, 24264–24273.

[199] A. Z. Stasiak, E. Larquet, A. Stasiak, S. Müller, A. Engel, E. Van Dyck, S. C. West and E. H. Egelman, The Human RAD52 Protein Exists as a Heptameric Ring, *Current Biology*, 2000, **10**, 337–340.

[200] W. Kagawa, H. Kurumizaka, R. Ishitani, S. Fukai, O. Nureki, T. Shibata and S. Yokoyama, Crystal Structure of the Homologous-Pairing Domain from the Human RAD52 Recombinase in the Undecameric Form, *Molecular Cell*, 2002, **10**, 359–371.

[201] M. R. Singleton, L. M. Wentzell, Y. Liu, S. C. West and D. B. Wigley, Structure of the Single-strand Annealing Domain of Human RAD52 Protein, *Proceedings of the National Academy of Sciences*, 2002, **99**, 13492–13497.

[202] I. Brouwer, H. Zhang, A. Candelli, D. Normanno, E. J. Peterman, G. J. Wuite and M. Modesti, Human RAD52 Captures and Holds DNA Strands, Increases DNA Flexibility, and Prevents Melting of Duplex DNA: Implications for DNA Recombination, *Cell Reports*, 2017, **18**, 2845–2853.

[203] M. de Odrowaz Piramowicz, P. Czuba, M. Targosz, K. Burda and M. Szymoński, Dynamic Force Measurements of Avidin-biotin and Streptavdin-biotin Interactions using AFM, *Acta Biochimica Polonica*, 2006, **53**, 93–100.

[204] T. E. Ouldridge, A. A. Louis and J. P. K. Doye, DNA Nanotweezers Studied with a Coarse-Grained Model of DNA, *Physical Review Letters*, 2010, **104**, 178101.

[205] B. E. K. Snodin *et al.*, Introducing Improved Structural Properties and Salt Dependence into a Coarse-grained Model of DNA, *The Journal of Chemical Physics*, 2015, **142**, 234901.

[206] A. Kuzuya, K. Numajiri, M. Kimura and M. Komiyama, Single-Molecule Accommodation of Streptavidin in Nanometer-Scale Wells Formed in DNA Nanostructures, *Nucleic Acids Symposium Series*, 2008, **52**, 681–682.

[207] N. B. Becker, A. Rosa and R. Everaers, The Radial Distribution Function of Worm-like Chains, *The European Physical Journal E*, 2010, **32**, 53–69.

[208] Cytodiagnostics, *Gold Nanoparticle Properties*, `http://www.cytodiagnostics.com/store/pc/viewcontent.asp?idpage=2`.

[209] A. O. Govorov, W. Zhang, T. Skeini, H. Richardson, J. Lee and N. A. Kotov, Gold Nanoparticle Ensembles as Heaters and Actuators: Melting and Collective Plasmon Resonances, *Nanoscale Research Letters*, 2006, **1**, 84–90.

[210] N. Zeng and A. B. Murphy, Heat Generation by Optically and Thermally Interacting Aggregates of Gold Nanoparticles under Illumination, *Nanotechnology*, 2009, **20**, 375702.

[211] Z. Qin and J. C. Bischof, Thermophysical and Biological Responses of Gold Nanoparticle Laser Heating, *Chemical Society Reviews*, 2012, **41**, 1191–1217.

[212] M. Reismann, J. C. Bretschneider, G. Von Plessen and U. Simon, Reversible Photothermal Melting of DNA in DNA-gold-nanoparticle Networks, *Small*, 2008, **4**, 607–610.

[213] R. A. Forties, R. Bundschuh and M. G. Poirier, The flexibility of locally melted DNA, *Nucleic Acids Research*, 2009, **37**, 4580–4586.

[214] A. Brunet, C. Tardin, L. Salomé, P. Rousseau, N. Destainville and M. Manghi, Dependence of DNA Persistence Length on Ionic Strength of Solutions with Monovalent and Divalent Salts: A Joint Theory-Experiment Study, *Macromolecules*, 2015, **48**, 3641–3652.

[215] P. A. Wiggins and P. C. Nelson, Generalized Theory of Semiflexible Polymers, *Physical Review E*, 2006, **73**, 031906.

[216] F. Lankaš, R. Lavery and J. H. Maddocks, Kinking Occurs during Molecular Dynamics Simulations of Small DNA Minicircles, *Structure*, 2006, **14**, 1527–1534.

[217] J. Curuksu, M. Zacharias, R. Lavery and K. Zakrzewska, Local and Global Effects of Strong DNA Bending Induced during Molecular Dynamics Simulations, *Nucleic Acids Research*, 2009, **37**, 3766–3773.

[218] M. S. Kellermayer, S. B. Smith, H. L. Granzier and C. Bustamante, Folding-unfolding Transitions in Single Titin Molecules Characterized with Laser Tweezers, *Science*, 1997, **276**, 1112–1116.

[219] M. D. Wang, M. J. Schnitzer, H. Yin, R. Landick, J. Gelles and S. M. Block, Force and Velocity Measured for Single Molecules of RNA Polymerase, *Science*, 1998, **282**, 902–907.

[220] M. Rief, M. Gautel, F. Oesterhelt, J. M. Fernandez and H. E. Gaub, Reversible unfolding of individual titin immunoglobulin domains by AFM, *Science*, 1997, **276**, 1109–1112.

[221] T. Ando, N. Kodera, E. Takai, D. Maruyama, K. Saito and A. Toda, A High-speed Atomic Force Microscope for Studying Biological Macromolecules, *Proceedings of the National Academy of Sciences*, 2001, **98**, 12468–12472.

[222] K. Haase and A. E. Pelling, Investigating Cell Mechanics with Atomic Force Microscopy, *Journal of The Royal Society Interface*, 2015, **12**, 20140970.

[223] L. Finzi and J. Gelles, Measurement of Lactose Repressor-mediated Loop Formation and Breakdown in Single DNA Molecules, *Science*, 1995, **267**, 378–380.

[224] F. Vanzi, Lac repressor hinge flexibility and DNA looping: single molecule kinetics by tethered particle motion, *Nucleic Acids Research*, 2006, **34**, 3409–3420.

[225] D. Rutkauskas, H. Zhan, K. S. Matthews, F. S. Pavone and F. Vanzi, Tetramer Opening in LacI-mediated DNA Looping, *Proceedings of the National Academy of Sciences*, 2009, **106**, 16627–16632.

[226] L. Han, H. G. Garcia, S. Blumberg, K. B. Towles, J. F. Beausang, P. C. Nelson and R. Phillips, Concentration and Length Dependence of DNA Looping in Transcriptional Regulation, *PLoS ONE*, 2009, **4**, e5621.

[227] T. Plénat, C. Tardin, P. Rousseau and L. Salomé, High-throughput Single-molecule Analysis of DNA-protein Interactions by Tethered Particle Motion, *Nucleic Acids Research*, 2012, **40**, e89–e89.

[228] S. Ucuncuoglu, D. A. Schneider, E. R. Weeks, D. Dunlap and L. Finzi, in *Single-Molecule Enzymology: Nanomechanical Manipulation and Hybrid Methods*, ed. M. Spies and Y. Chemla, Academic Press, 2017, vol. 582, pp. 415–435.

[229] T. Odijk, Stiff Chains and Filaments under Tension, *Macromolecules*, 1995, **28**, 7016–7018.

[230] V. Kahl, A. Gansen, R. Galneder and J. O. Rädler, Microelectrophoresis in a Laser Trap: A Platform for Measuring Electrokinetic Interactions and Flow Properties within Microstructures, *Review of Scientific Instruments*, 2009, **80**, 073704.

[231] E. P. Diamandis and T. K. Christopoulos, The biotin-(strept)avidin system: Principles and applications in biotechnology, *Clinical Chemistry*, 1991, **37**, 625–636.

[232] X. Shan, Y. Fang, S. Wang, Y. Guan, H. Y. Chen and N. Tao, Detection of Charges and Molecules with Self-assembled Nano-oscillators, *Nano Letters*, 2014, **14**, 4151–4157.

[233] G. Ma, Y. Guan, S. Wang, H. Xu and N. Tao, Study of Small-Molecule–Membrane Protein Binding Kinetics with Nanodisc and Charge-Sensitive Optical Detection, *Analytical Chemistry*, 2016, **88**, 2375–2379.

[234] G. Ma, H. Zhu, Z. Wan, Y. Yang, S. Wang and N. Tao, Optical Imaging of Single Protein Size, Charge, Mobility, Binding and Conformational Change, *bioRxiv*, 2019, 505404.

[235] R. Karlsson and A. Fält, Experimental Design for Kinetic Analysis of Protein-protein Interactions with Surface Plasmon Resonance Biosensors, *Journal of Immunological Methods*, 1997, **200**, 121–133.

[236] M. Beseničar, P. Maček, J. H. Lakey and G. Anderluh, Surface Plasmon Resonance in Protein–membrane Interactions, *Chemistry and Physics of Lipids*, 2006, **141**, 169–178.

[237] J. F. Marko and E. D. Siggia, Stretching DNA, *Macromolecules*, 1995, **28**, 8759–8770.

[238] K. Namink, X. Meng, M. Koper, P. Kukura and S. Faez, Electric-Double-Layer-Modulation Microscopy, *Physical Review Applied*, 2020, **13**, 044065.

[239] J. Lyklema, in *Fundamentals of Interface and Colloid Science*, Academic Press, 1995, vol. 2, ch. 3, pp. 1–3.

[240] M. Z. Bazant, K. Thornton and A. Ajdari, Diffuse-charge Dynamics in Electrochemical Systems, *Physical Review E*, 2004, **70**, 021506.

[241] L. Collins *et al.*, Probing Charge Screening Dynamics and Electrochemical Processes at the Solid-liquid Interface with Electrochemical Force Microscopy, *Nature Communications*, 2014, **5**, 3871.

[242] C. L. Bentley, J. Edmondson, G. N. Meloni, D. Perry, V. Shkirskiy and P. R. Unwin, Nanoscale Electrochemical Mapping, *Analytical Chemistry*, 2019, **91**, 84–108.

[243] R. Smeets, U. F. Keyser, D. Krapf, M. Y. Wu, N. H. Dekker and C. Dekker, Salt Dependence of Ion Transport and DMA Translocation through Solid-state Nanopores, *Nano Letters*, 2006, **6**, 89–95.

[244] D. G. Haywood, A. Saha-Shah, L. A. Baker and S. C. Jacobson, Fundamental Studies of Nanofluidics: Nanopores, Nanochannels, and Nanopipets, *Analytical Chemistry*, 2015, **87**, 172–187.

[245] X. Xiao and A. J. Bard, Observing Single Nanoparticle Collisions at an Ultramicroelectrode by Electrocatalytic Amplification, *Journal of the American Chemical Society*, 2007, **129**, 9610–9612.

[246] T. Albrecht, S. Horswell, L. K. Allerston, N. V. Rees and P. Rodriguez, Electrochemical Processes at the Nanoscale, *Current Opinion in Electrochemistry*, 2018, **7**, 138–145.

[247] W. N. Hansen and A. Prostak, Electromodulation of the Optical Properties of Gold, *Physical Review*, 1968, **174**, 500–503.

[248] A. Bewick, F. A. Hawkins and A. M. Tuxford, Studies of the Electrical Double Layer and of Adsorbed Species on Electrodes using Modulated Specular Reflectance Spectroscopy, *Surface Science*, 1973, **37**, 82–89.

[249] M. Stedman, Effect of the Electrical Double Layer on the Reflectance and Ellipsometry of Electrolyte-conductor Interfaces, *Chemical Physics Letters*, 1968, **2**, 457–460.

[250] J. D. McIntyre, Electrochemical Modulation Spectroscopy, *Surface Science*, 1973, **37**, 658–682.

[251] D. M. Kolb, W. Boeck, K. M. Ho and S. H. Liu, Observation of Surface States on Ag(100) by Infrared and Visible Electroreflectance Spectroscopy, *Physical Review Letters*, 1981, **47**, 1921–1924.

[252] A. M. Brown, M. T. Sheldon and H. A. Atwater, Electrochemical Tuning of the Dielectric Function of Au Nanoparticles, *ACS Photonics*, 2015, **2**, 459–464.

[253] C. M. Hill, R. Bennett, C. Zhou, S. Street, J. Zheng and S. Pan, Single Ag Nanoparticle Spectroelectrochemistry via Dark-field Scattering and Fluorescence Microscopies, *Journal of Physical Chemistry C*, 2015, **119**, 6760–6768.

[254] C. P. Byers, B. S. Hoener, W.-S. Chang, S. Link and C. F. Landes, Single-Particle Plasmon Voltammetry (spPV) for Detecting Anion Adsorption, *Nano Letters*, 2016, **16**, 2314–2321.

[255] H. Zhu, F. Zhang, H. Wang, Z. Lu, H. Y. Chen, J. Li and N. Tao, Optical Imaging of Charges with Atomically Thin Molybdenum Disulfide, *ACS Nano*, 2019, **13**, 2298–2306.

[256] P. Kukura, H. Ewers, C. Müller, A. Renn, A. Helenius and V. Sandoghdar, High-speed Nanoscopic Tracking of the Position and Orientation of a Single Virus, *Nature Methods*, 2009, **6**, 923–927.

[257] J. O. Arroyo and P. Kukura, Non-fluorescent Schemes for Single-molecule Detection, Imaging and Spectroscopy, *Nature Photonics*, 2016, **10**, 11–17.

[258] N. An, B. Zhuang, M. Li, Y. Lu and Z. G. Wang, Combined Theoretical and Experimental Study of Refractive Indices of Water-Acetonitrile-Salt Systems, *Journal of Physical Chemistry B*, 2015, **119**, 10701–10709.

[259] G. Kavei, Y. Zare and A. Mohammadi Gheidari, Evaluation of Surface Roughness and Nanostructure of Indium Tin Oxide (ITO) Films by Atomic Force Microscopy, *Scanning*, 2008, **30**, 232–239.

[260] S. Gardonio *et al.*, Characterization of Indium Tin Oxide Surfaces after KOH and HCl Treatments, *Organic Electronics: physics, materials, applications*, 2008, **9**, 253–261.

[261] A. J. Bard, G. Inzelt and F. Scholz, *Electrochemical Dictionary*, Springer Science & Business Media, 2008.

[262] G. Young and P. Kukura, Interferometric Scattering Microscopy, *Annual Review of Physical Chemistry*, 2019, **70**, 301–322.

[263] G. Young *et al.*, Quantitative Mass Imaging of Single Biological Macromolecules, *Science*, 2018, **360**, 423–427.

[264] A. Weigel, A. Sebesta and P. Kukura, Dark Field Microspectroscopy with Single Molecule Fluorescence Sensitivity, *ACS Photonics*, 2014, **1**, 848–856.

[265] B. Huang, W. Wang, M. Bates and X. Zhuang, Three-Dimensional Super-Resolution Imaging by Stochastic Optical Reconstruction Microscopy, *Science*, 2008, **319**, 810–813.